A Thesis Submitted for the Degree of PhD at the University of Warwick

Permanent WRAP URL:

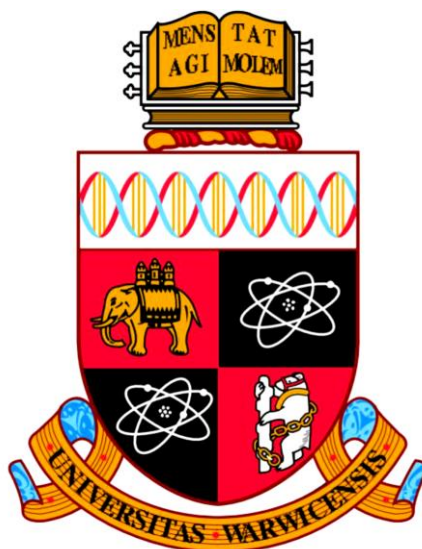http://wrap.warwick.ac.uk/183170

warwick.ac.uk/lib-publications

BIOANALYTICAL APPLICATIONS OF BORON DOPED DIAMOND ELECTRODES

BY

TEENA SUSAN RAJAN

A Thesis Submitted to the University of Warwick for the
Degree of Doctor of Philosophy in Chemistry

Department of Chemistry

December 2022

TABLE OF CONTENTS

ACKNOWLEDGMENTS

Firstly, I would like to express my deepest appreciation to my supervisor Professor Julie V. Macpherson. Thank you for all your patience, support, and guidance throughout my PhD. Thank you to Professors Bhavik Anil Patel, and Martyn Boutelle for sharing their extensive knowledge and experience, and the interesting discussions this sparked! I would also like to acknowledge EPSRC, Diamond Science and Technology Centre for Doctoral Training, and the Department of Chemistry at Warwick for providing the funding and facilities to be able to complete this PhD.

I owe a special thanks to the many fellow CDT students and members of the Electrochemistry and Interfaces Group, past and present, who have provided a supportive and enjoyable environment.

Finally, to all my family and friends, thank you for all your love, patience, and support (and asking why I still haven't submitted yet!).

DECLARATIONS

I declare that all the work presented in this thesis is entirely original and my own work, except when carried out in collaboration, as outlined below. I also confirm that this thesis has not been submitted for a degree at another university.

Work from Chapter 3 is published as:

T. S. Rajan, T. L. Read, A. Abdalla, B. A. Patel, and J. V. Macpherson, *Ex vivo* electrochemical pH mapping of the gastrointestinal tract in the absence and presence of pharmacological agents, *ACS Sensors*, 2020, 5(9), 2858-2865.
DOI: 10.1021/acssensors.0c01020

The work presented in Chapter 4 is in preparation for publication. Nafiz Biswas collected the viscosity measurements reported. Invaluable discussions were conducted with Katherine Levey and Irina Terrero Rodríguez. Dr. Georgia F. Wood, Daniel Houghton, and Anjali John assisted with FE-SEM imaging.

The work presented in Chapter 5 was undertaken in collaboration with Dr. Tania L. Read, and a MSc student, Harry Tomkins. Some of the data is published in his Masters report. A publication of this work is in preparation.

LIST OF FIGURES

LIST OF TABLES

ABBREVIATIONS

3D	Three-dimensional
A	Electrode area
AA	Amino acid
a_{RHS}, a_{LHS}	Activity of the reactants and products
AC	Alternating current
AN	Acupuncture
ANOVA	Analysis of variance
BDD	Boron doped diamond
BDD-IrOx	Iridium oxide electrodeposited on BDD
BDD-Q	BDD with incorporated quinone groups
BSA	Bovine serum albumin
c	Concentration
C_{dl}	Double layer capacitance
C_g	Capacitance of the diffuse Gouy layer
C_s	Capacitance of the compact Stern layer
CA	Chronoamperometry
CAD	Computer-aided design
CB	Conduction band
CE	Counter electrode
CFME	Carbon fibre microelectrode
CNT	Carbon nanotubes
CPE	Constant Phase Element
CSF	Cerebrospinal fluid
CV	Cyclic Voltammetry
CVD	Chemical Vapour Deposition
D	Diffusion coefficient
D_h	Hydraulic Diameter
DA	Dopamine
DOS	Density of electronic states
E	Electrode potential
E^o	Standard electrode potential

$E^{o\prime}$	Formal electrode potential
E_f	Fermi Level
E_{pzc}	Potential of zero charge
E_{step}	Potential step
EDL	Electrical double layer
EEC	Equivalent electrical circuit
EIS	Electrochemical Impedance Spectroscopy
ET	Electron Transfer
F	Faraday's constant
FBS	Fetal bovine serum
FE-SEM	Field-emission scanning electron microscopy
FSCV	Fast scan cyclic voltammetry
GC	Glassy carbon
GERD	Gastroesophageal reflux disease
GI	Gastrointestinal tract
HPHT	High Pressure High Temperature
HSA	Human serum albumin
i	Current
i_{lim}	Limiting current
i_p	Peak current
i_{pa} and i_{pc}	Anodic and cathodic peak
IPA	Isopropyl alcohol
IPE	Ideal Polarisable Electrode
IHP	Inner Helmholtz Plane
IrOx	Iridium oxide
ISF	Interstitial fluid
ISFET	Ion selective field effect transistors
j	Imaginary number
J	Flux
JW	Jackson waveform
n	Number of electrons
NP	Nanoparticle
NPG	Nanoporous gold electrode

OCP	Open circuit potential
OHP	Outer Helmholtz Plane
Ox	Oxidised species
pI	Isoelectric point
PAN	Polyaniline
PBS	Phosphate buffered saline
PCET	Proton coupled electron transfer
PDMS	Polydimethylsiloxane
pI	Isoelectric point
PPI	Proton pump inhibitor
PyC	Pyrolytic carbon
PZC	Point of zero charge
Q	Quinone
r	Electrode radius
R	Universal gas constant
R_{ct}	Charge transfer resistance
R_s	Solution resistance
R_u	Uncompensated resistance
Re	Reynolds number
RE	Reference Electrode
Red	Reduced species
SCE	Saturated Calomel electrode
SLA	Stereolithography
SW	Solvent window
SWV	Square Wave Voltammetry
t	Time
T	Temperature
ta-C	Tetrahedral amorphous carbon
$\bar{U}$	Mean fluid velocity
ν	Scan rate
V	Voltage
V_f	Volume flow rate
VB	Valence band

ω	Angular frequency
W	Warburg impedance element
WE	Working Electrode
WLH	White light interferometry
x	Distance
Z_{int}	Interfacial impedance

ABSTRACT

Maintaining pH homeostasis is one of the most important biological processes, and variations in tissue or fluid pH can often be related to diseases. Hence, detecting pH changes accurately could be crucial for early diagnosis. This thesis investigates electrochemical methods for accurate biological pH measurements. Of importance is characterising protein fouling on the electrode surfaces and the implications for accurate pH evaluation.

Chapter 3 investigates the *ex vivo* pH profiling of the gastrointestinal (GI) tract using an electrochemical pH sensor. Also, the variation caused by omeprazole and melatonin, known to alter the pH in upper GI tract. Three pH electrodes, glass electrode, iridium oxide electrodeposited on boron doped diamond (BDD-IrOx), and quinone surface integrated BDD (BDD-Q), were assessed in a GI-tract mimic solution to determine suitability before *ex vivo* application. When assessing the electrodes in terms of response time, robustness and minimal electrode fouling, the BDD-Q was determined to be the most suitable sensor.

Chapter 4 explores the effect of protein adsorption on: BDD, a BDD that has the whole surface laser ablated to sp^2 carbon (sp^2-BDD), and a glassy carbon. The performance of these electrodes was assessed in 0.5% mucin (GI-tract mimic), and 5% bovine serum albumin (most abundant protein in blood). Fouling was studied using three different methods: (i) Time-dependent change in cyclic voltammograms of metal redox couples ($Ru(NH_3)_6^{3+}$, $IrCl_6^{2-}$); (ii) Changes in double layer capacitance in response to protein solutions; and (iii) the effect of applied electrode potential on protein adsorption and the subsequent silver electrodeposition.

Chapter 5 describes the development of a 3D-printed flow cell capable of housing a BDD-Q pH electrode to conduct pH measurements under controlled flow. We hypothesise that flow can be used to reduce fouling from mucin and albumin. The BDD-Q sensor was flow-independent in the range from 0.1 to 100 mL/min. The pH of solutions containing proteins were measured under stationary and flow (100 mL/min) conditions, while alternating with buffer solution. Conducting pH measurements under flow improved the accuracy of the measurement. A similar experiment was conducted in blood, a more complex media with multiple proteins. Measurements conducted at 100 mL/min showed low variation in pH using the BDD-Q.

Chapter 1.   INTRODUCTION

1.1. ELECTROCHEMISTRY

Electrochemistry is a powerful technique for understanding physical and chemical processes at an interface which undergoes charge transfer.[1] Most measurements are made at solid-liquid interfaces where the solid constitutes the electrode and the liquid the electrolyte. Electrochemical measurements are typically either potentiometric (where a voltage between two interfaces is measured), or voltammetric (where a potential is applied to an electrode with respect to a reference electrode to drive an electron transfer reaction, and a current is measured).[2] The reactions occurring at an electrode interface can be divided into two categories: non-Faradaic, where no charge transfer takes place at the interface, but external currents may flow to compensate for changes at the interface; and Faradaic, involving the transfer of electrons across the electrode interface, as a result of the reduction and/or oxidation of redox-active analytes in solution.[1–3]

1.1.1. Non-Faradaic Processes

An ideal polarised electrode (IPE) is defined as an electrode at which no charge transfer can occur across the electrode-solution interface, regardless of applied potential.[2] The range over which an electrode behaves as an IPE in electrolyte solution is often referred to as its solvent window (SW). The electrode-solution interface can be considered analogous to a parallel-plate capacitor.[4] The electrode surface is one plate of the capacitor, and the solution is the other, when a change in potential is applied to the electrode surface, ions in solution rearrange to balance the change in electron density at the electrode surface, which results in a change to the structure of the electrochemical double layer (EDL). Figure 1.1 shows the Gouy-Chapman-Stern-Graham model for EDL.
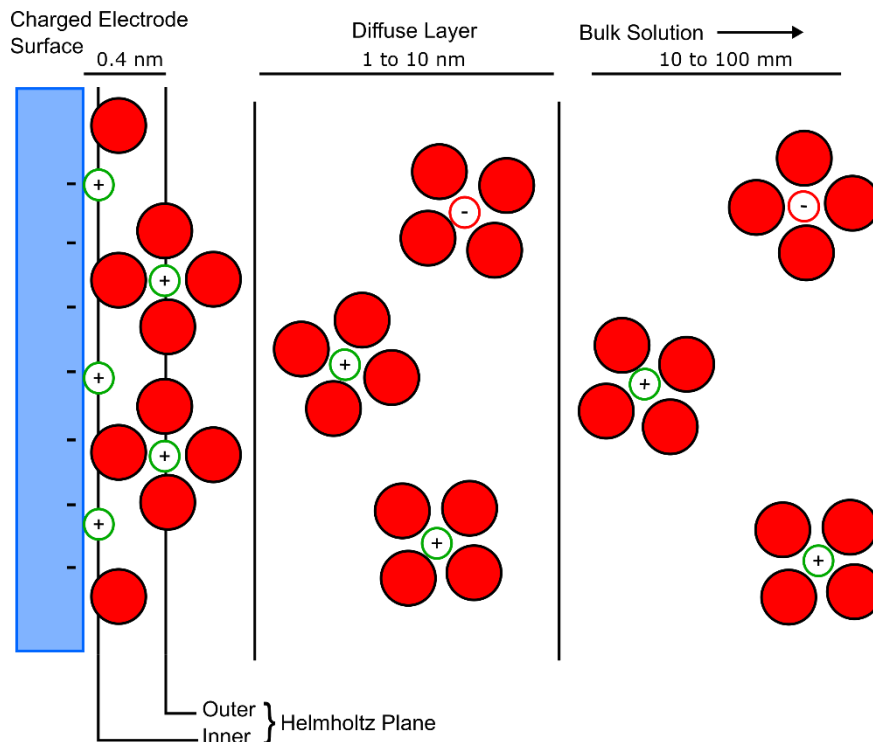
Figure 1.1. Schematic for the Gouy-Chapman-Stern-Graham model of the electrochemical double layer at an electrode surface assuming a negatively charged electrode. The compact double layer consisting of densely arranged ions which maintain charge neutrality. In the inner Helmholtz plan are specifically adsorbed dehydrated species, the outer Helmholtz plane consists of hydrated counterions and the diffuse layer of ions which extends into the bulk solution.[5]

The region nearest to the electrode/electrolyte interface is known as the inner Helmholtz plane (IHP), where species without their hydration shell, and solvent molecules are specifically adsorbed. Next to it is the outer Helmholtz plane (OHP), which consists of a layer of hydrated ions that have very strong long-range coulombic interactions with the charged electrode.[6,7] The diffuse layer (or Gouy layer) develops outside the OHP, and the concentration of cations in the diffuse layer decreases exponentially with distance from the electrode surface.[8]

The thickness of the EDL depends on the ionic strength of the solution, with a smaller double layer thickness in higher ionic strength solutions.[4] The higher the ionic strength the more ions exist in solution, so excess charge (relative to the point of zero charge, PZC) on the surface can be compensated over

a shorter distance. The capacitance of the EDL characterises its ability to store charge in response to a change in potential and consists of a combination of the capacitance of the compact (Stern) layer and the diffuse layer (Gouy layer),[6,9] Equation 1.1.

$$1/C = 1/C_S + 1/C_G \qquad\qquad \text{Equation 1.1}$$

where C is the double layer capacitance, C_S and C_G represent the capacitances of the compact and diffuse layers, respectively. The potential at which the electrode contains zero charge density is known as the potential of zero charge (E_{pzc}).[2,6] At potentials more positive than E_{pzc}, the electrode surface carries a positive charge, and at potentials more negative, the surface carries a negative charge.

The electrochemical cell for an IPE can be represented by an equivalent electrical circuit (EEC), consisting of a capacitor, that represents the EDL capacitance C_{dl}, and a resistor, to represent the system resistance (Figure 1.2). The system resistance is a combination of several resistances in series, such as, the solution resistance (controlled by solution conductivity), resistances not associated with electron/ion transfer i.e., poor electrode conductivity, high electrode contact resistance, blocked reference electrode frit.[10] These resistances are collectively described as the uncompensated resistance, R_u.[10]
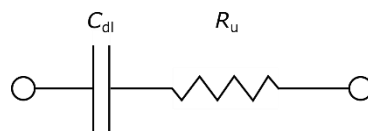
Figure 1.2. Equivalent electrical circuit for an ideal polarised electrode.

R_u and C_{dl} contributes to the non-Faradaic current (often called charging or capacitive current) observed during a chronoamperometry (CA) or cyclic voltammetry (CV) experiment. The current-time response observed is described by Equation 1.2,

$$i = \frac{\Delta E_{step}}{R_u} \exp\left(-\frac{t}{R_u C_{dl}}\right) \qquad\qquad \text{Equation 1.2}$$

Thus, the current decreases exponentially with time. Here, i is the current, ΔE_{step} is the potential step, and t is time. Equation 1.3 can be used to calculate C_{dl} of solid electrodes in contact with electrolyte. This is measured experimentally by recording CVs at different scan rates in a supporting electrolyte solution and plotting the charging current at a given potential versus the scan rate.[11] The gradient of the straight line obtained corresponds to $C_{dl}A$.

$$C_{dl} = \frac{i_{av}}{A\,\upsilon} \qquad \text{Equation 1.3}$$

Where, C_{dl} is the specific double layer capacitance (i.e., per unit area), i_{av} is the average current magnitude at a given potential (A), υ is the scan rate (V/s) and A is the electrode area (cm^2).

One of the oldest electroanalytical techniques used to characterise C_{dl}, of the electrode/electrolyte interface is electrochemical impedance spectroscopy.[12] Equation 1.4 can be used to approximate C_{dl},

$$Z_{int} = \frac{1}{j\omega C_{dl}} \qquad \text{Equation 1.4}$$

where, Z_{int} is the interfacial impedance, j is the imaginary number ($\sqrt{-1}$) and ω is the angular frequency of the oscillating sine wave. When a circuit contains only a capacitor, the real impedance is zero, while the imaginary part is inversely proportional to the capacitance and frequency. Measurement of C_{dl} can provide valuable insights into adsorption and desorption processes,[13,14] as well as the structure of film-modified electrodes.[15,16]

1.1.2. Faradaic Processes

A simple faradaic reaction can be represented by Equation 1.5,

$$O + ne^- \rightleftharpoons R \qquad \text{Equation 1.5}$$

where, O and R represent the oxidised and reduced soluble forms respectively, of an electroactive species. The position of equilibrium depends on the standard electrode potential (E^0), under standard conditions (298 K, unit activity). When the electrochemical system deviates from standard conditions, the Nernst equation (Equation 1.6) is used to determine the electrode potential,

$$E = E^0 - \frac{RT}{nF} \ln\left(\frac{a_{RHS}}{a_{LHS}}\right)$$

<div align="right">Equation 1.6</div>

where, E is the electrode potential, n is the number of electrons transferred, F is the Faraday's constant (96485 C/mol), R is the universal gas constant (8.314 J/mol K), T is the absolute temperature (K), a_{RHS} and a_{LHS} are the activity of the redox species. Note when activity is replaced by concentration, E^0 is replaced by the formal electrode potential, $E^{0\prime}$.[2]

Under dynamic conditions where a current flows due to oxidation or reduction of species R/O respectively, depletion of redox species at the electrode-solution interface occurs and a resulting diffusion layer is always established. The thickness of this diffusion layer increases with time for a planar electrode (1D diffusion). The size of the diffusion layer can be controlled by the potential scan rate; at slower scan rates the diffusion layer becomes larger (slow mass transport), by increasing the scan rate the diffusion length is kept small (higher diffusive mass transport) and the peak current increases.

The rate of the electrode reaction is determined by the flux (J) of species to the electrode surface and is affected by a combination of several factors (Figure 1.3): (1) mass transfer rate of O from bulk solution to the electrode surface, (2) electron transfer (ET) rate at electrode surface, (3) chemical reaction before/after ET, and (4) surface reactions such as adsorption and desorption.[2]
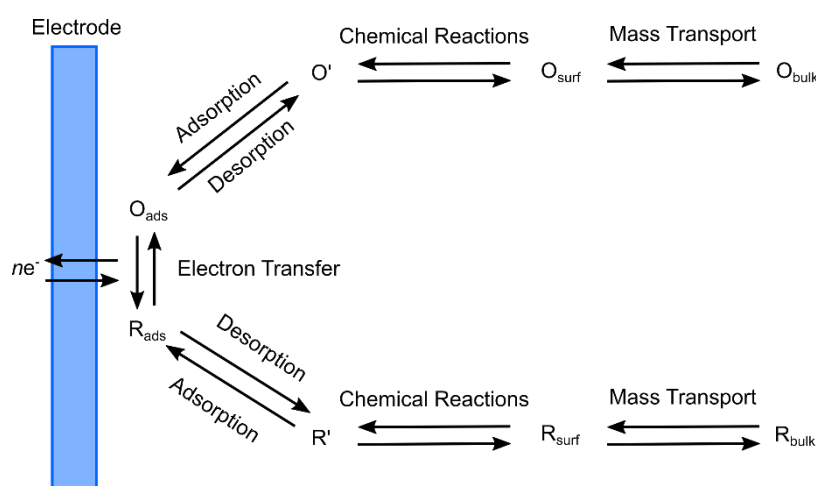
Figure 1.3. Schematic of a basic electrochemical reaction, showing the mass transport and kinetic electron transfer steps in the reduction of species O to R at the electrode surface.

Mass transport of electroactive species from the bulk to the electrode surface is an important factor that affects electrochemical reaction rates and currents. There are three forms of mass transport, and a combination of these contribute to the response observed in an electrochemical measurement. (1) Diffusion, discussed above, is the movement of species from a region of high concentration to a region of low concentration (i.e., concentration gradient). This is always present in a dynamic electrochemical system. (2) Migration is the movement of charged species in response to an electric field formed when a potential difference is applied between two electrodes. This can be the electric field generated at the electrode surface and/or that felt in solution due to the presence of a sizeable R_u. The latter results in Ohmic drop. The addition of a high concentration of non-electroactive supporting electrolyte minimises R_u, helps to compensate Ohmic drop, and reduces the thickness of the double layer.[2] (3) Convection, this is the movement of species in solution due to external forces such as stirring or hydrodynamic transport. To overcome these effects and simplify interpretation, electrochemical measurements are usually done in stationary solutions with the addition of excess supporting electrolyte.

Therefore, under conditions where electron transfer ten times faster than mass transport, and transport is by diffusion only, the currents are controlled by diffusion of species to the electrode surface, and is related to J through Equation 1.7 at a planar stationary electrode with area, A,

$$i = nAFJ$$ Equation 1.7

Diffusional flux can be related to the mass transport (diffusion) rate constant (k_t) and concentration of electroactive species (C) by Equation 1.8,

$$J = k_t C$$ Equation 1.8

Under diffusion only conditions, the reactions occurring at the electrode surface generates a concentration gradient, between the electrode surface and

6

the bulk solution, this in turn gives rise to a diffusional flux.[6] Therefore, Fick's first law can be applied under steady state diffusion, and the rate of diffusion is directly proportional to the diffusion coefficient (D cm^2/s) and the slope of the concentration gradient:

$$J = -D\frac{\delta c}{\delta x}$$

<div align="right">Equation 1.9</div>

To probe electron transfer (ET) kinetics, the diffusional flux must be suitably increased so that ET kinetics become rate limiting. This can be achieved by e.g. (i) scanning faster in a CV; (ii) moving to micro and nano electrodes, which due to the presence of significant radial diffusion in addition to linear diffusion have an increased diffusional flux,[17,18] or by introducing a convective contribution.[2,6]

1.1.3. Hydrodynamic methods

There are different methods for generating and controlling convection to the electrode surface. Typically, these involve the movement of either the electrode with respect to the solution (i.e., a rotating disk electrode)[2] or by inducing motion in the solution (i.e., in a flow cell).[19] In the tube or channel, two characteristic flow regimes are observed as depicted in Figure 1.4,
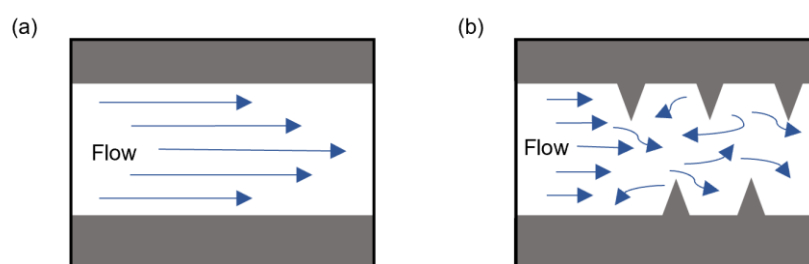
Figure 1.4.   Velocity profiles for (a) laminar and (b) turbulent flow

Laminar flow in a channel, also known as Poiseuille flow,[1] is characterised by an ordered velocity profile where the velocity is at the greatest along the centre of the channel and decays to zero at the walls (Figure 1.4a). Conversely turbulent flow is chaotic and poorly defined such that the velocity at a particular point is not predictable, as shown schematically in Figure 1.4b. Whether a solution is laminar or turbulent depends upon the velocity of the

solution, the geometry of the hydrodynamic system and the viscosity of the solution and is described by the Reynolds number (Re) of the system.[2] Laminar flow is observed for a channel system with a Re < 2000.[20,21] Re for a channel flow system, describing the ratio of convective to viscous forces, is given by Equation 1.10,

$$\mathrm{Re} = \frac{\bar{U}D_{\mathrm{h}}}{\nu} \qquad \text{Equation 1.10}$$

$\bar{U}$ is the mean fluid velocity (cm/s), ν is the kinematic viscosity (0.01 cm^2/s for water at 25°C),[19] and D_{h} is the hydraulic diameter, dependent on the channel dimensions. The values for $\bar{U}$ and D_{h} can be calculated from Equation 1.11 and Equation 1.12 for rectangular or square channel,

$$\bar{U} = \frac{V_{\mathrm{f}}}{2hw} \qquad \text{Equation 1.11}$$

$$D_{\mathrm{h}} = \frac{8hw}{2h + w} \qquad \text{Equation 1.12}$$

where, V_{f} is the volume flow rate (cm^3/s), h and w are the height and width of the channel, respectively. Under laminar flow the steady state limiting current (i_{lim}) response for a rectangular channel electrode system can be predicted by Levich equation, Equation 1.13,[22,23]

$$i_{\mathrm{lim}} = 1.165 \, nFCD^{\frac{2}{3}}\bar{U}^{-\frac{1}{3}}h^{-\frac{1}{3}}wx_e^{\frac{2}{3}} \qquad \text{Equation 1.13}$$

where, x_{e} is the length of the band electrode.

1.1.4. Electrochemical Techniques

Voltammetry is commonly used for electroanalysis, where a potential waveform is applied digitally and the current in the electrochemical cell is recorded using a potentiostat. This current represents several processes, both Faradaic and non-Faradaic depending on the experimental conditions.

CV is the most commonly used electrochemical technique. In CV, the potential is scanned in one direction at a defined scan rate, and then reversed to complete the cycle, Figure 1.5a. The resulting current *vs.* potential response can

inform on the electrode characteristics and response to an electroactive species. Exemplar CVs for a macroelectrode, Figure 1.5b, and microelectrode or electrode under forced convection reactions, Figure 1.5c, are presented.
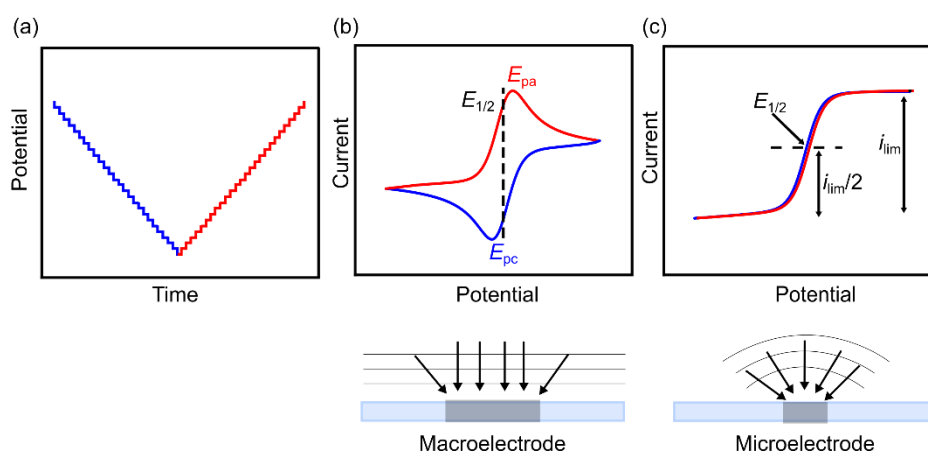
Figure 1.5. (a) A staircase cyclic voltammogram waveform and resulting exemplar current response for a reversible reaction on a (b) macroelectrode and (c) microelectrode including the respective diffusional profiles.

Digital potentiostats cannot apply an analog 'true linear' waveform, instead the potential sweep consists of a series of discrete potential steps, resolution of which depends on the bit size of the digital to analogue converter (DAC) e.g., 16 bit DAC has a resolution of 0.305 mV, resulting in a staircase scan (Figure 1.5a).[24] For each potential step an *i-t* curve is obtained, the potentiostat analyses the current over a region of this curve. The analysis method varies between potentiostats, current sampling could be the end of the step, or the average current over a certain percentage of the step, however, some potentiostats also allow the option to choose how much of the current is sampled.[10] To avoid this, on some potentiostats, a true analog generator can be added. The approximation of staircase CV to linear sweep CV is only valid under certain conditions,[25] and may not be appropriate for more complex time dependent processes (such as, adsorption).[26]

For a species in solution, in the oxidised form, the scan starts at a potential well positive of E^0, and one where no current is flowing (the open circuit potential, OCP) and is then scanned in a negative direction. As the potential approaches E^0, the reduction of the species begins and a faradaic current starts

to flow, depleting O species at the surface, and causing an increase in flux and current. Increasing E results in an increase in the current up to a potential where a maximum peak current results (i_p: i_{pa} and i_{pc} for the anodic and cathodic peak respectively). For fast electron transfer at some point past the peak current, the concentration profile at the electrode surface is such that the concentration of O at the electrode surface is zero.[27] Under fast electron transfer, diffusion-controlled conditions, the theoretical peak-to-peak potential separation ΔE_p is 57 mV (at T = 298 K) for a one ET reaction.[28]

In the case of a planar macroelectrode, with a linear diffusional profile, after reaching i_p, a subsequent drop in current is observed, as the rate of mass transfer of the redox species to the electrode surface is not sufficiently fast to replace that being consumed at the electrode surface. For reversible reactions, under diffusion-controlled conditions, i_p can be described using the Randles-Sevcik equation, Equation 1.14,[2] assuming T = 298 K.

$$i_p = 0.4463 \left(\frac{F^3}{RT}\right)^{\frac{1}{2}} n^{\frac{3}{2}} A D^{\frac{1}{2}} C v^{\frac{1}{2}}$$

Equation 1.14

where, v is the scan rate (V/s). By substituting i_p for i in Equation 1.7 and using Equation 1.8, then k_t can be determined using Equation 1.15.

$$k_t = 2.69 \times 10^5 n^{\frac{1}{2}} D^{\frac{1}{2}} v^{\frac{1}{2}} F^{-1}$$

Equation 1.15

For a 1 mm diameter planar disc electrode, assuming $n = 1$, $D = 1 \times 10^{-5}$ cm^2/s, and v = 100 mV/s, k_t is calculated as 0.0028 cm/s.

At the surface of a planar microelectrode, the diffusional flux profile changes from planar to hemispherical (Figure 1.5c), thereby increasing the flux of electroactive species to the microelectrode surface compared to that at a macroelectrode. As the potential is scanned out in the negative direction, the current increases and reaches a steady state limiting current, i_{lim}, due to the high diffusional flux. On scanning back, the product of the ET reaction diffuses away from the electrode sufficiently fast, so that there is no product to detect in the reverse reaction. For a disk microelectrode, i_{lim} is predicted using Equation 1.16,[6]

$$i_{lim} = 4nrFDC$$

Equation 1.16

where, r is the electrode radius (cm). Under this condition, for a disk microelectrode, $k_t = 4D/\pi r$,[2] therefore, for a disk of diameter 1 μm, $k_t = 0.25$ cm/s, nearly two orders of magnitude greater than a 1 mm macroelectrode. Under diffusion limited conditions for a fast electron transfer reversibly system, the $\Delta E_{\frac{3}{4}-\frac{1}{4}}$, known as the Tomes potential, corresponds to the potential difference between three-quarter wave and one-quarter wave of the limiting current response is 56.4 mV/n (Figure 1.5c).[29]

CV can be used to determine the ET kinetics of a redox active species. When ET at the electrode surface is slow compared to mass transport, i.e., the process is now kinetically limited, for a reductive process this means a more negative potential needs to be applied for an appreciable current to flow. This results in a distortion of the CV for both macro and micro electrodes, with a shift in $E^{0'}$ and a concomitant increase in ΔE_p (for planar macro electrodes) and $\Delta E_{\frac{3}{4}-\frac{1}{4}}$ (for microelectrode).

A further commonly used electroanalytic technique is square wave voltammetry (SWV). SWV is a type of pulse voltammetry technique, in which the waveform consists of a series of symmetric square wave pulses, superimposed on a base staircase potential[30] (Figure 1.6). The variables that can be changed include, the frequency and amplitude of pulses, and increment for each potential step.
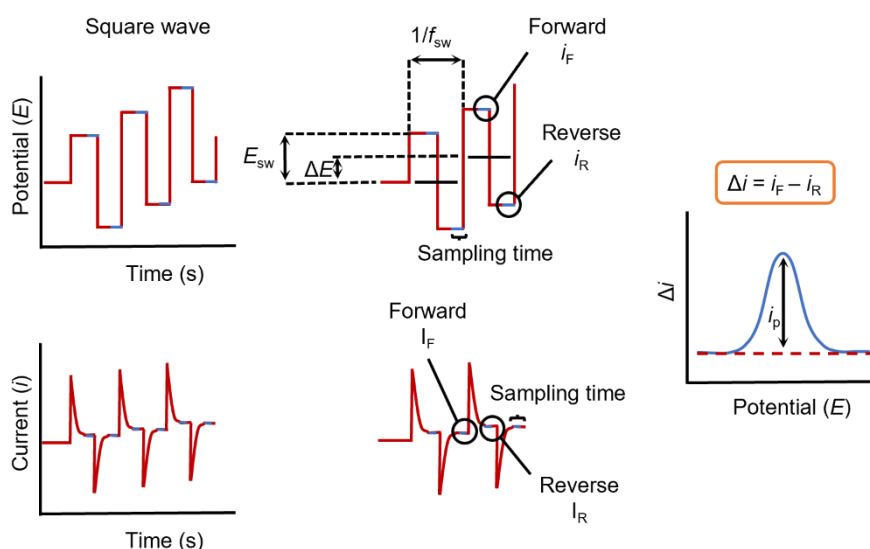
Figure 1.6. Square wave voltammogram waveform and current decays. Current sampling points have been indicated and the resulting *i-V* curve.

The current is sampled twice during each square-wave cycle, once at the forward pulse, and once at the reverse pulse. Current commercial potentiostats sample over a proportion of the pulse (often the last 40%, although this varies between manufacturers). The difference between the two measurements is plotted versus the base staircase potential (Figure 1.6). The raw data extracted from SWV is a series of current-time (*i-t*) decays in the forward and reverse directions with the length of decay determined by the frequency of pulse applied. The *i-t* decays are a combination of non-faradaic ($e^{\frac{-t}{R_u C_{dl}}}$) and faradaic ($t^{-1/2}$) components. If the solution is sufficiently conductive, the non-faradaic component will decay well before the faradaic current signal, resulting in negligible contributions from charging current in the final voltammogram.[31] Therefore, much lower detection limits are achievable using SWV (concentrations of ~nM) compared to CV (~µM).[31,32] Other pulsed techniques include normal pulse voltammetry and differential pulse voltammetry.[33] The choice of the type of voltammetric technique to use often depends on the application. For all techniques, a range of parameters should be tested to ensure the best detection limits are achieved.

1.1.5. Electrochemical cell

The electrochemical cell varies depending on the size of the working electrode (WE) used. For a microelectrode, where small (<10 nA) currents are observed, a two-electrode set up is typically used, consisting of a WE, where the reaction of interest occurs, and a reference electrode (RE) that provides a stable and fixed reference potential against which the potential measured at the WE are compared. For micro and smaller electrodes, even though current flows through RE in a two-electrode set-up it is not enough to perturb the RE potential.[10] A RE holds a constant and known potential by virtue of being encased with a constant composition of potential determining ions. Typical RE's include $Hg/Hg_2Cl_2/Cl^-$ or

Ag/AgCl/Cl⁻, commonly referred to as saturated calomel electrode (SCE), and silver-silver chloride respectively. For the former the concentration of chloride is saturated, whilst for the latter different known concentrations of Cl^- can be used.[34]

As the electrode diameter increases to the macro scale (mm size), the currents measured also increase, and passing currents through the RE will result in RE polarisation and drift (drift of few mVs is common). Therefore, to prevent current flow through the RE, a counter electrode (CE) is introduced, typically coil or mesh of platinum or other inert metal, and the potential of CE shifts to allow currents of equal and opposite magnitude of that observed at the WE to pass through the CE. Since most of the time CE is platinum, water oxidation or reduction could occur. It is important that the CE has a surface area significantly larger than the WE, to avoid any limitation on the reactions occurring at the surface of the WE. The three-electrode cell set up is depicted in Figure 1.7.
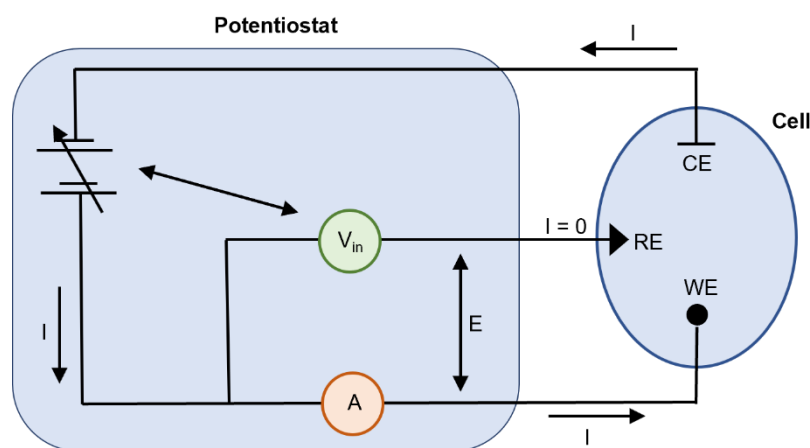
Figure 1.7. Schematic of a typical three-electrode electrochemical set up. Current flows between the counter (CE) and working (WE) electrodes, whilst potential is controlled between the WE and reference (RE) electrodes.[10]

All three electrodes are connected to a potentiostat, which controls the potential between the WE and RE, and records the resultant current between the WE and CE.

1.1.6. Electrode materials

A WE can be fabricated from any conductive material, provided it does not react with the reactant or product of interest for analysis. The ideal material for electroanalysis would have low background currents, low ohmic resistance, a large potential window of analysis, low toxicity, inexpensive, reproducible, and stable. Mercury electrodes (drop and film) used to be the most commonly used WE, due to favourable properties such as, minimal non-faradaic contribution, a wide cathodic window (up to -2.5 V), easily renewable and highly reproducible surface.[35] However, due to the limited anodic potential range,[6] extreme toxicity of mercury,[36,37] and mechanical instability (i.e., the mercury drops are easily displaced),[38] it is no longer practically applicable as an electrode material, particularly for biological sensing or for flow applications.

Platinum, gold, and carbon-based electrode materials have been used as alternative WEs to mercury electrodes. Metal electrodes offer favourable electron transfer kinetics and a large anodic potential range. However, the electrodes are limited in the cathodic window (to -0.2 to -0.5 V region, depending on pH)[6] and have high background currents associated with surface oxide or adsorbed hydrogen layer formation.[39,40] The presence of these films can alter the electrode reaction kinetics, and lead to irreplicable results.

Carbon based electrodes are in widespread use for electroanalysis. Primarily due to the broad SW, low cost, biocompatibility, and electrocatalytic activity for various redox reactions.[41–44] The allotropes of carbon include graphite, diamond, and carbon fibres.[44] The hybridisation in carbon materials vary, with carbon atoms in graphite all being sp^2 hybridised. Diamond is entirely sp^3 hybridised and requires dopants for electrical conductivity for electrochemistry. Carbon nanotubes (CNT) are the most commonly used fullerene-based electrochemical material, which can be single or multiple layers of graphite sheets rolled up to form a tube structure. For an electrode material the density of electronic states (DOS), determined by the microstructure and surface states, controls the ET kinetics of the material. A low DOS can reduce the ET rate, which is the case for boron doped diamond, or highly oriented pyrolytic graphite, compared to metal electrodes.[44–46]

Basal plane carbon surfaces are robust, and relatively inert, although, the material is still susceptible to surface contaminations (e.g., adsorbed hydrocarbons) which can significantly affect ET processes.[47–49] Pristine carbon surfaces are difficult to achieve in a real-world setting, as the surface becomes contaminated upon exposure to air.[47,50] Although, methods have been explored in polishing[51] or modifying[52,53] the surface to ensure a reproducible electrode surface with improved sensitivity and selectivity.

1.2. BORON DOPED DIAMOND AS AN ELECTRODE MATERIAL

Diamond is a remarkable material containing $\sim 2 \times 10^{23}$ carbon atoms per cm³, exhibits very high thermal conductivity (24-25 $Wcm^{-1}K^{-1}$ at 300 K, compared to 1.5 for Si, and 4 for Cu),[54] incredibly hard and mechanically stable making it resistant to wear and chemical attack.[55] However, due to the wide band gap of 5.47 eV (at 300 K),[54] it is an electrical insulator (Figure 1.8a). In order to produce the electrical conductivity necessary for an electrode material, diamond can be doped with either boron (*p*-type dopant), or nitrogen (*n*-type dopant). Boron effectively takes up the same position as a carbon atom, with a relatively small activation energy (0.37 eV), and unlike nitrogen (1.7 eV), high doping levels are possible.[56] Therefore, boron is the preferred dopant for electrochemical studies.
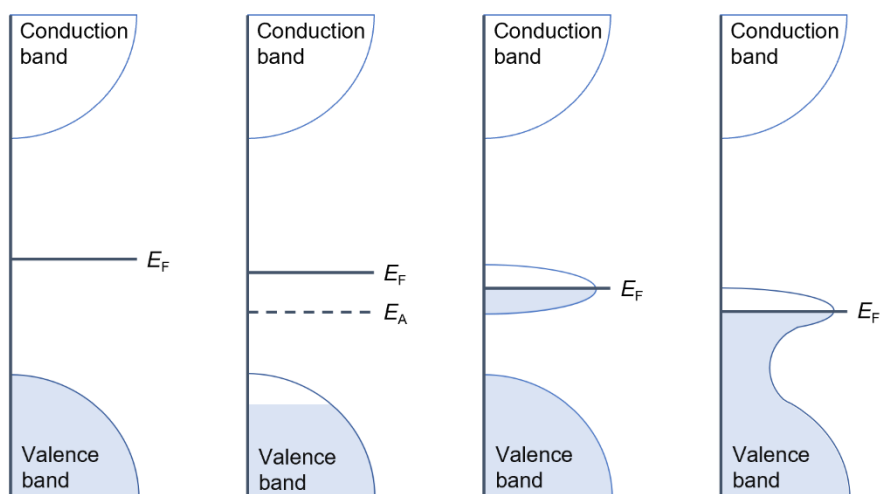
Figure 1.8. Electronic band structure (a) intrinsic diamond, a wide band gap insulator with the Fermi level (E_f) in between the valence (VB) and conduction band (CB); (b) lightly boron doped diamond the

carrier concentration depends on the ionisation energy of boron and the temperature; (c) heavily doped diamond ($\sim 10^{20}$ atoms per cm^3), where the dopant wavefunctions overlap, resulting in delocalisation and metallic behaviour with E_f inside the dopant state.[57]

At moderate doping levels ($\sim 10^{18}$ boron atoms per cm^3) BDD is a *p*-type semiconductor with an acceptor level (E_A) in the diamond bandgap (Figure 1.8b), boron atoms accept electrons from the valence band (VB), leading to holes in the VB. With dopant densities above $\sim 10^{20}$ atoms per cm^3, BDD can have a metallic conduction behaviour, as the dopants are close enough together for their wavefunctions to overlap (Figure 1.8c). This leads to hopping conduction and pinning the Fermi level (E_f) in the dopant states. Boron doping is accompanied by a colour change from colour-less (intrinsic) through blue (semiconducting doping levels) to black (metallic doping levels).

BDD exhibits many advantageous properties over other common electrode materials, such as Au, Pt, and glassy carbon (GC) including:[56,58,59] wide SW, low background currents, corrosion resistance at high temperatures, pressures and in challenging environments, and reduced fouling due to its inert, low roughness and hydrophilic (*O*-terminated) surface. Figure 1.9a shows the comparison of a typical BDD SW with other common electrode materials.
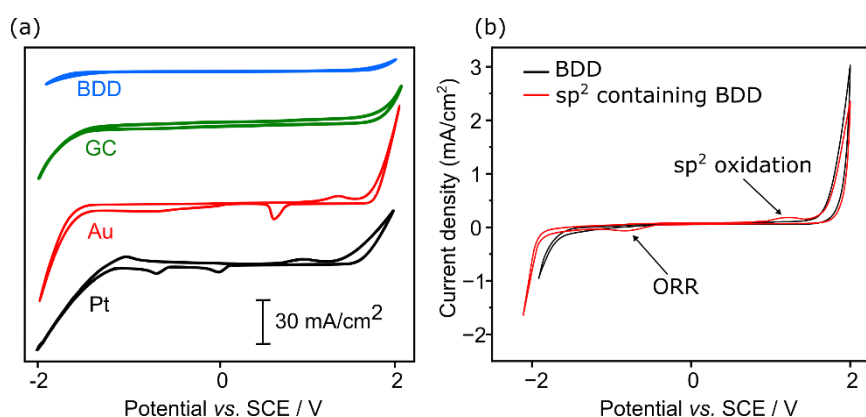
Figure 1.9. (a) Comparison of SWs for BDD, GC, Au, and Pt, in 0.1 M KNO$_3$ at 0.1 V/s,[60] (b) SWs in 0.1 M KNO$_3$ for BDD and sp^2 containing BDD ($\sim$pH 5-7).

To understand why BDD exhibits such a large SW (>3 V in 0.1 M KNO$_3$, within a ± 0.4 mA/cm^2 threshold),[61] it is important to note that the sp^3 structure

results in the BDD surface showing very low electrocatalytic activity towards water splitting. As water electrolysis is an inner-sphere redox, the water molecules must adsorb favourably to the electrode surface in order for an ET event to occur. BDD surfaces are known to be weakly adsorbing.[62,63] This differentiates from outer-sphere redox reactions that only require proximity to the electrode surface for ET, therefore are not sensitive to surface chemistry or functionality.[2]

Ideally, there would not be any sp² carbon present in a BDD electrode. However, it is extremely challenging to exclude all sp² carbon during the diamond growth or processing stages.[56,61] Although, it is noted that growth conditions do exist for BDD growth with minimal sp² carbon as used herein.[61] If present, sp² carbon is most commonly found at grain boundaries. The presence of sp² carbon also increases the electrocatalytic activity of BDD,[64] reflected in Figure 1.9b. The SW is reduced as water electrolysis is facilitated by the increase in electrocatalytic sp² carbon sites.[65] On sp² carbon containing BDD, the reductive window also shows a current-voltage signal for the reduction of oxygen and a further current response due to oxidation of sp² carbon in the oxidative window, limiting the SW of the electrode.[56] For certain applications, such as e.g., low concentration sensing (where low background currents are required) or the generation of hydroxyl radials responsible for electrochemical combustion (requires a low adsorbing surface), the presence of sp²-carbon on BDD can be considered detrimental.[66,67] However, there are also instances where increasing the electroactivity of BDD is useful.[68,69] For example, for hydrogen peroxide generation *via* oxygen reduction reaction in acid solutions,[70] or the detection of hypochlorite in unbuffered solutions,[71] and determination of free chlorine concentration for disinfecting drinking water.[72]

1.3. pH SENSING

The pH scale was first introduced by the Danish Chemist Søren Peder Lauritz Sørensen, who defined pH as the negative logarithm of proton activity (*aH*⁺, Equation 1.17)[73]

$$pH = -\log(aH^+)$$
<div align="right">Equation 1.17</div>

pH is used to characterise the degree of acidity of an aqueous solution at a given temperature. pH measurement techniques have been widely used in food production,[74] environmental monitoring,[75] waste management,[76] and biomedical applications.[77]

1.3.1. Glass pH Electrode

The glass pH electrode response was first observed by Max Cremer in 1906, he noticed that a solid-liquid interface, separated by a thin glass bubble created an electric potential that could be measured. Later, in 1909, Fritz Haber and Zygmunt Klemensiewicz, applied this electric potential to hydrogen ion activity, which is now recognised as the glass electrode (Figure 1.10).[78] The glass pH sensors have a high sensitivity and selective towards protons (H+).[79] They are capable of accurately determining the pH in a wide range from pH 2-12 and their response is reasonably fast (<60 s). Furthermore, the electrodes are cheap and commercially available, and have a long lifetime.
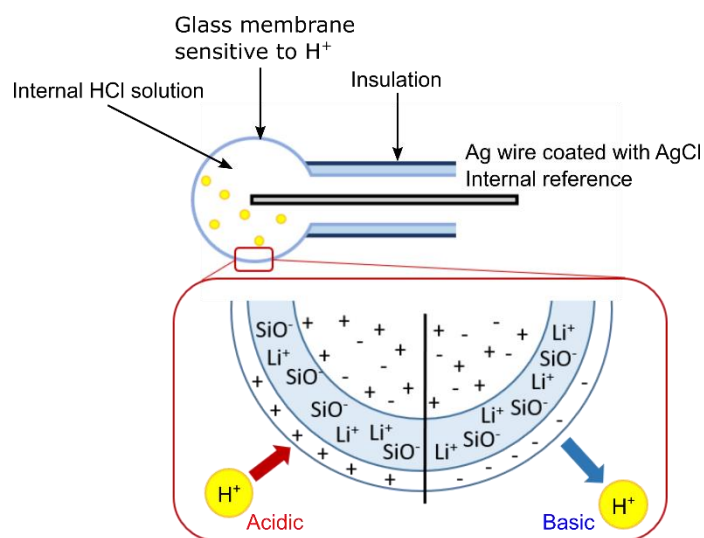
Figure 1.10. Schematic of a glass pH electrode

The sensor is a hydrogen ion selective electrode, comprised of a RE, typically Ag|AgCl/Cl- RE, and a thin glass membrane (ca. 0.1 mm thick) coupled with an external RE, the interface show a constant potential difference. The pH sensing capability arises from ion exchange that occurs at the surface of the glass membrane, which consists mainly of amorphous silicon dioxide, and becomes

protonated when exposed to solution. Furthermore, the sensor includes a combined thermocouple to measure and compensate for temperature changes. The degree of protonation establishes a potential difference at the glass membrane, which can be related to the solution pH via the Nernst equation, Equation 1.18.[6,78]

$$E = K - \frac{2.303\,RT}{nF} pH \hspace{3cm} \text{Equation 1.18}$$

where, K is a constant that includes all sample-independent potential contributions.[6] The electrode potential is measured with respect to an external RE. Therefore, the cell potential (at 298 K) is,

$$E_{cell} = K' + 0.059\,pH \hspace{3cm} \text{Equation 1.19}$$

The glass pH electrode, however, has several issues, the glass is inherently fragile, and must be kept hydrated to maintain performance. Additionally, at high pH, alkali cations of similar charge and size to protons, such as Li+, Na+, and K+ can bind to the glass membrane resulting in inaccurate pH measurements.[80] Previously, the electrodes have been applied for biological pH measurements,[78] however, due to the fragility of the glass, *in vivo* measurements are difficult.

1.3.2. Metal Oxides

A wide variety of metal oxide materials have been developed for electrochemical pH sensing, as they offer the potential for integration on wearable and flexible substrate, low cost of fabrication, and biocompatibility.[81] pH sensors have been constructed from the materials of Ir/IrO_2, Pt/PtO_2, Ru/RuO_2, Pb/PbO_2, Sb/Sb_2O_3, and W/W_2O_3.[82–86] In particular, iridium oxide (IrOx) sensors have exhibited excellent stability over a wide pH range at high temperatures (up to 250°C).[81,87,88] These electrodes are formed from a thick IrOx layer deposited via thermal decomposition of iridium[(III)], sputtering,[88] or electrochemical deposition.[89] The potentiometric response of IrOx to pH is a function of the transition of Ir between two oxidation states, Ir[(IV)] oxide and Ir[(III)] oxide, as shown in Equation 1.20.[90]

$$\text{Ir}^{(IV)}\text{oxide} + q\text{H}^+ + ne\text{-} \leftrightarrow \text{Ir}^{(III)}\text{oxide} + r\text{H}_2\text{O} \qquad \text{Equation 1.20}$$
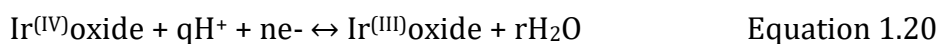
Iridium oxide electrodes follow the Nernst equation for pH response, and the slopes of the electrodes vary between 59 and 90 mV/pH, depending on the preparation method. Anhydrous iridium oxides prepared by thermal oxidation or sputtering showed pH response of 59 mV/pH, in comparison to the super-Nernstian response (90 mV/pH) observed on electrochemically deposited (hydrated) iridium oxides.[85]

Similar to the glass pH electrode, the IrOx electrodes can be stored in a solution that is most similar to the solution of interest, to ensure the film stabilises after deposition. Additionally, variation in the composition and hydration of IrOx films can have significant effects on the pH response, and cause delamination of the film. IrOx film is unstable to anions,[91] which can be a challenging for physiological application due to the high concentrations of chloride present.

1.3.3. Ion Selective Field Effect Transistors

Ion Selective Field Effect Transistors (ISFET) devices have gained interest as an alternative to glass electrodes, due to the fact the sensors can be stored dry, robust, and easily miniaturised.[92–95] The pH measurements work by controlling the current between two semiconductor electrodes separated by a third electrode (the gate) that is in direct contact with the solution of interest, integrated into a silicon chip. The gate is a proton sensitive chemical layer such as silicon oxide, silicon nitride, aluminium oxide or tantalum pentoxide which becomes hydrated by electrolyte solution. This layer then acts as a surface charge transfer layer, allowing current to flow from one of the electrodes to the other. The degree of protonation of the gate (thus the solution pH) dictates the potential observed, which exhibits a Nernstian dependence. ISFET devices often have drift issues, and experience blockages in real-world samples.[96]

1.3.4. Quinone-based pH Sensors

Voltammetric pH sensing using carbon electrodes has been attractive due to their intrinsic biocompatible, robust nature, and low cost.[97,98] A review by

Kahlert[99] summaries the numerous methods which have been used to functionalise carbon surfaces with quinones for pH sensing applications. These include physical adsorption of organic molecules (e.g., quinhydrone),[100,101] chemical oxidation of the surface,[102] and electrochemically assisted covalent bonding *via* reduction of aryl diazonium salts,[103] or oxidation of amines.[104]

Quinones (Q) are a category of organic compounds that undergo proton coupled electron transfer reactions (PCET). The different possible PCET pathways for Q have been summarised using a scheme of squares, as depicted in Figure 1.11.[105,106]
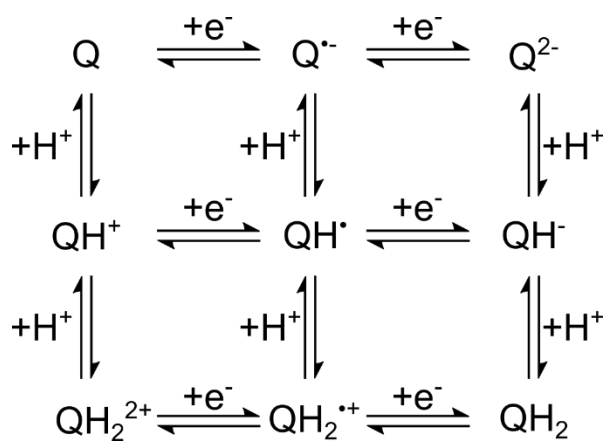
Figure 1.11. Quinone scheme of squares demonstrating the possible electron and proton transfer reactions pathways.

In aprotic solvents, only electron transfer is possible ($Q + 2e^- \rightleftharpoons Q^{2-}$), with the voltammetric response typically two well defined redox peaks, that are pH independent.[107] In aqueous buffered media, Q undergoes PCET of $2e^-$ and $2H^+$ ($Q + 2H^+ + 2e^- \rightleftharpoons QH_2$), this response is pH dependent, and the peak potential shifts towards negative potentials as pH increases. PCET can occur in one concerted step, or in a stepwise manner with the ET or proton transfer taking place first.[108] The situation where the second ET is thermodynamically easier than the first, is known as potential inversion,[109] results in a single redox peak corresponding to $Q \rightleftharpoons QH_2$ in aqueous media. The reduction potential shows a good linear dependence on pH, with a slope of -59 mV/pH, in agreement with the Nernst equation, Equation 1.21.[109]

$$E = E^0 + \frac{0.0592}{2} \log \frac{[Q]}{[QH_2]} - 0.0592 \text{ pH}$$
<div align="right">Equation 1.21</div>

As the pH of the solution increases, and pK$_{a1}$ of Q is reached (Figure 1.12), a 2e$^-$ and H$^+$ reaction occurs, which equals a 30 mV/pH unit change. By increasing the pH further, exceeding pK$_{a2}$, a proton independent ET reaction (2e$^-$) occurs, this is the case in aprotic solvents.[110]
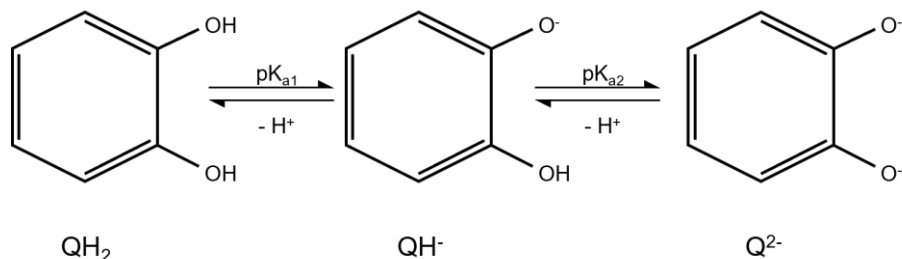
Figure 1.12. Reaction schematic for the deprotonation of quinone showing pK$_{a1}$ and pK$_{a2}$

Recent work pioneered by Ayres *et al*[111] involves the controlled introduction of sp^2-carbon regions on BDD using laser micromachining, to create BDD pH sensitive (BDD-Q) sensors, where the sp^2 bonded carbon has been integrated into the surface with quinone terminations resulting from a chemical oxidation.[111–114] The BDD-Q sensors follow a Nernstian pH response, with -59 mV/pH across the buffered and unbuffered pH range 2-12.[111,112]

1.4. ELECTROCHEMICAL SENSORS

Electrochemical sensors have the reputation of being small, cheap, and easy to use for analytical applications.[112] The rapid response time (typical CV takes ~16 s per cycle or SWV takes ~6 s per scan) of electrochemistry makes it appealing for use in medical applications where quick analyses are necessary for medical diagnostics, to ensure treatment effectiveness, and to understand dynamic changes during diseases. One of the biggest problems for an electrochemical sensor being used in a biomedical application is biofouling.[113–115]

1.4.1. Biological Fouling

Electrode fouling is a term used to describe the passivation of an electrode surface by a substance, that forms impermeable or permeable layers

on the surface, modifying charge and electron transfer kinetics at the electrode/electrolyte interface.[116] Electrode fouling negatively affects the sensitivity, detection limit, reproducibility, and reliability of the electrochemical sensor. The term biofouling is often used to describe fouling due to (1) the undesired growth of bacterial biofilms (e.g., *Pseudomonas aeruginosa*) on sensors,[119,120] (2) the adsorption of biological matrix molecules (such as proteins),[121-123] or (3) formation of by-products of signalling molecules (e.g., polymerisation of oxidised catecholamines) on the electrode surface.[124,125] This absorption on the electrode surface can hinder electrode reactions for accurate determination of analytes of interest.

For biomedical applications, electrode stability over time is vital. One major challenge is that in the complex biological fluids (such as urine, saliva, etc.) or the *in vivo* environment, the concentration of biological analytes of interest is often very low compared to the large concentration of coexisting background species (e.g., cells, proteins) that can adsorb onto the electrode surface. Therefore, can lead to reduced accuracy and precision of the measurement.[116,117,126] Furthermore, on biomedical implants, that are in direct contact with blood, protein adsorption can lead to thrombosis.[127] Moreover, protein adsorption can trigger adhesion of bacteria, particles, or cells and can promote inflammation and fouling processes.[128-131]

The type of fouling on the electrode surface can vary. Figure 1.13 illustrates examples of different types of film formation on an electrode surface due to a (bio)fouling process.[125,132] The film formed on the electrode surface can be thought of as an insulating and partially blocking film that allows ET at uncovered regions on the surface. This film formation results in a significant reduction in the current response, and slower ET kinetics over time, where (if given enough time) the electrode will eventually be completely blocked and unable to detect any current response. Protein adsorption is an example of partially blocking layer that does not allow any charge passing through the blocked region,[133] this is explored further in Chapter 4.
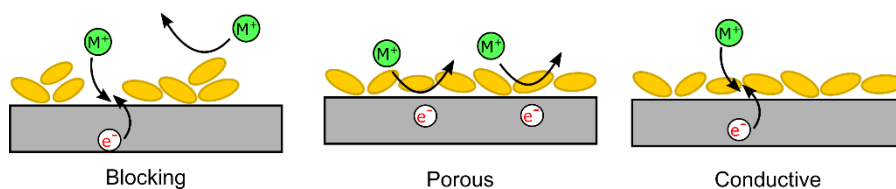
Figure 1.13. Schematic to demonstrate different processes for electrode fouling. Adapted from Patel *et al*,[125] and Patel.[132]

Fouling could also result in the formation of a porous permeable film, where the fouling film will alter the mass transfer of the analyte to the surface, reducing the current response, but it will not result in a complete loss of response. Hence, the response is altered, but the electrode is still functional in a fouled state. Finally, the film formed on the surface can be conductive (or partially), allowing ET at a reduced rate. This type of film formation can be identified by the presence of additional redox features in the resulting voltammogram, that can interfere with the analysis of the signal of interest.

The fouling molecule typically adsorbs onto the electrode surface due to favourable interactions, such as hydrophilicity/hydrophobicity, and electrostatics, which depend on the physico-chemical properties of the fouling agent and electrode material.[134–136] This section aims to give an overview of some of the electrochemical methods used for characterising biological fouling due to the biological environment (specifically protein adsorption) or from by-products of electrochemical reactions (e.g., dopamine polymerisation).

1.4.2. Factors affecting protein adsorption on electrode surfaces

There are several factors that influence protein adsorption on an electrode surface, (i) solution conditions, (ii) protein properties (conformation, charge distribution and strength of intramolecular bonds) and (iii) electrode surface properties (chemistry, charge, roughness, and surface energy). The conditions used to study protein adsorption can have a considerable influence on the adsorption behaviour. External parameters include pH, temperature, and ionic strength.[131]

The pH of the solution is known to determines the electrostatic state of the protein molecules. When the pH equals the isoelectric point (pI) of the protein, it is considered that the amount of negative and positive charges on the protein are balanced, resulting in a net neutral molecule.[137,138] Therefore, at low pH conditions (pH < pI), proteins are thought to be net positively charged, and at high pH (pH > pI), proteins are net negatively charged. Electrostatic protein-protein repulsions are minimised at pI, this allows for higher packing densities on the electrode surface. Adsorption rates are increased when protein and substrate have opposite charges, due to electrostatic attraction.[139,140] Interestingly, bovine serum albumin (BSA) adsorption on various surfaces showed that the maximum adsorption was observed near the pI.[141–143]

While strong protein adsorption generally occurs on charged surfaces, there is an interesting exception to this rule. Studies have shown that zwitterionic surfaces can be highly resistant to protein adsorption.[144] Zwitterionic groups are closely spaced positively and negatively charged groups with a net zero charge. These surfaces are generally thought to be able to bind to water molecules and counterions strongly enough to prevent their displacement by proteins, thus providing a means to create electrode surfaces that are highly resistant to protein fouling.[145,146]

The amount of protein adsorbed on the substrate surface is usually higher at high temperatures than that at room temperature.[147] Jackson *et al.* explored the temperature dependence of BSA adsorption between 295 – 343 K,[148] note, BSA has a melting point of 336 K. It was observed that 316 K was a threshold temperature, i.e., below 316 K, the surface concentration of BSA on titanium was 2.52 mg/m^2 and above 316 K the concentration suddenly increased to 6.50 mg/m^2. This increase is related to the partial unfolding (spreading on material surface) of BSA.[148] Furthermore, at temperatures higher than 333 K, thermal denaturing and unfolding of BSA begins causing a sudden increase in concentration to 10.3 mg/m^2. A similar response was observed on Pt[149] and stainless steel.[150]

The concentration of dissolved ions, i.e., the ionic strength of the solution, also affects protein adsorption.[131] Rabe *et al.* compared the adsorption kinetics of BSA at low (5 mM) and high (50 mM) citrate buffer ionic strength on

a hydrophilic glass surface.[151] The reduction of buffer ionic strength was shown to increase the Debye length from 1.4 to 4.3 nm, which means the electrostatic potential of the protein is less efficiently shielded at lower ionic strength.[152,153] Consequently, the electrostatic repulsions between charged molecules are more pronounced at low ionic strength, forcing protein molecules to adsorb far apart from each other. However, at high ionic strength, because there is less repulsion, protein molecules can adsorb more closely, and at higher density.

The most important aspect to consider for long-term applications of electrodes in biological media, is the affinity of a protein for the substrate surface, i.e., how likely it is that the protein will adsorb and how strongly will it adhere. Protein molecules will spontaneously adsorb to a surface if the process results in an overall decrease in the system and its environment's free energy. The change in free energy is denoted by:

$$\Delta G = \Delta H - T\Delta S \qquad\qquad \text{Equation 1.22}$$

where ΔG is the change in free energy of the process under constant temperature and pressure, ΔH is the change in enthalpy, ΔS is the change in entropy. The change in enthalpy is composed of two separate terms:

$$\Delta H = \Delta E + p\Delta V \qquad\qquad \text{Equation 1.23}$$

where ΔE is the change in bond energy, p is the absolute pressure, and ΔV is the change in volume. Since the change in volume for protein adsorption is typically negligible in aqueous solution conditions, ΔH mainly represents the change in overall bond energy that occurs during protein adsorption, which is an exothermic reaction. Note, G, H, and S are state functions i.e., they only depend on the difference between the start and end states of the defined system and surrounding system, and therefore are not influenced by the path that a given process takes. These thermodynamics processes include the interaction between the protein and electrode surface, but also with the surrounding aqueous media. Under physiological conditions, the surrounding media consists of water molecules with charged cations and anions from dissociated salts, and other biomolecules.

The protein-electrode interaction can vary immensely depending on the protein and electrode surface properties. At nonpolar surfaces, protein adsorption is mediated by hydrophobic interactions, because nonpolar surfaces do not have functional groups that can form hydrogen bonds. Proteins, have a mixture of hydrophobic and hydrophilic regions, and can reorganise to interact with a nonpolar (hydrophobic) surface. However, water molecules only weakly interact with a nonpolar surface and are at a higher free energy state, therefore, the displacement of the surface water molecules by proteins is energetically favourable hence result in a reduction of the free energy of the system. Equally, the displacement of water molecules around the nonpolar groups on the protein surface can also contributes to lowering the free energy of the system. These combined effects provide a strong thermodynamic driving force for the adsorption of protein to a nonpolar surface.[131,134] The thermodynamic driving force will also guide the orientation of the protein molecules on the nonpolar surface, as shown in Figure 1.14. Indicating that the favourable nonpolar (protein)-nonpolar (electrode surface) interactions result the protein molecule unfolding and occupying a large area of the electrode surface.[116]
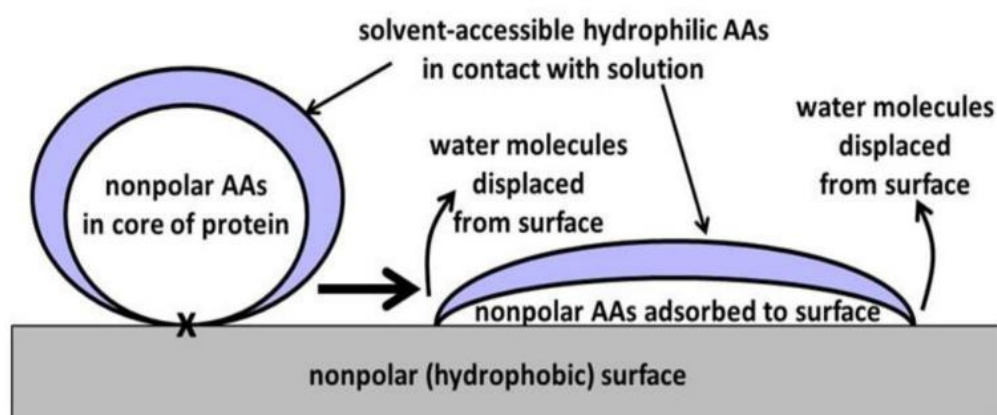
Figure 1.14. Illustration of protein adsorption on a nonpolar (hydrophobic) surface. Amino acid (AA) residues. Figure from Latour.[134]

Downard and Roddick, investigated the response for the oxidation of ferrocenemethanol in the absence and presence of BSA, at modified glassy carbon (GC) electrodes.[154] The surface of the GC electrode was modified using a

diazonium salt to covalently bind various *p*-substituted phenyl groups. This study found, increasing the carboxylate groups close to the surface did not reduce protein adsorption. However, hydrophobic groups close to the surface (e.g., methoxy) block access of the analyte and render the surface more prone to BSA adsorption. Furthermore, hydrophilic groups (e.g., carboxylates) attached to the surface via long linkages reduced the amount of protein able to contact the electrode surface for adsorption.

Protein interactions with polar electrode surfaces are mediated by the formation of hydrogen bonds, between the polar amino acid residues on the protein and polar groups on the electrode surface. The functional groups at the electrode surface will form strong hydrogen bonds with water, therefore adsorption of protein to this surface involves the breaking of these hydrogen bonds. Here, the driving force is an entropic effect (Figure 1.15). Proteins are large macromolecules that are covered in many polar functional groups, therefore, the displacement of multiple surface bound water molecules for one protein molecule is entropically favourable and occurs spontaneously.
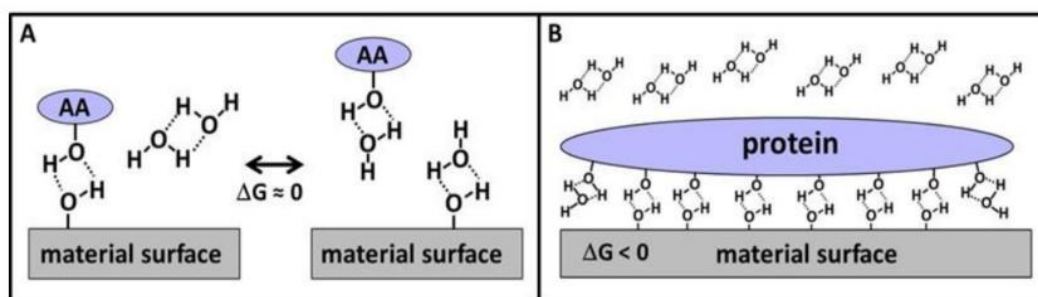
Figure 1.15. Illustration of protein adsorption on a neutral polar (hydrophilic) surface. (A) Single amino acid with a hydroxyl group adsorbing to surface. (B) Protein with multiple hydrogen-bondable groups interacting with the polar surface. Figure from Latour.[134]

Due to the strong hydrophobic interaction in aqueous media, many antifouling strategies involve increasing the hydrophilicity of the electrode surface.[116] For example, the walls of CNTs are generally hydrophobic, with strong aromatic π-π interactions, Thomas *et al*., reported the analysis of tryptophan using an oxidised multiwalled CNT-modified carbon paste electrode, which

showed good reproducibility, stability, and antifouling properties.[155] The oxidation of CNT introduces a large number of oxygen functional groups on the surface, which in turn increases the hydrophilicity of the material.

1.4.3. Electrochemical Characterisation Methods

The accurate characterisation of biological fouling is crucial for the optimisation of medical devices that interact with complex biological environments. Inaccurate or incomplete characterisation may hinder the discovery of promising biomaterials, as initial findings may not translate to *in vivo* assessments. A number of electrochemical techniques, either in isolation or in combination with non-electrochemical techniques have been used to study electrode fouling. Non-electrochemical methods have recently been comprehensively reviewed by Jesmer *et al.* and Wei *et al.*[156,157] A critical comparison of non-electrochemical surface characterisation techniques was also reported recently by Hedayati *et al.*,[158] which concludes that surfaces which are conventionally defined as low- or ultralow protein fouling (e.g., binding <5 ng/cm^2 of protein in a short-term adsorption study) accumulate adsorbed proteins in long-term experiments. Therefore, future studies should include an evaluation of long-term (> 5 mins) protein-surface interactions.

1.4.3.1. Cyclic Voltammetry (CV)

CV is a useful technique that is often the first experiment performed in an electrochemical study of an analyte, a biological material, or an electrode material. Non-faradaic and faradaic processes can be investigated using CV, described in Section 1.1.1 and 1.1.2.[159,160] Changes in ET due to the presence of protein molecules on the electrode surface typically result in a change in the shape of the CV e.g., a change in the magnitude of the peak current or ΔE_p.[6,161]

For example, the CV response for the reduction of potassium ferricyanide at a robust flexible nanoporous gold (NPG) electrode and a planar gold electrode in the absence and presence of fibrinogen showed that fibrinogen barely effected the electrochemical signal on NPG acquired over 60 mins. In contrast the redox peaks disappeared within the first 10 mins on the planar gold electrode.[160] Nanoporous electrodes have demonstrated higher fouling resistance than planar

electrodes, however, the antifouling properties are strongly depend on the size of the pores. This is demonstrated in a study by Patel *et al*, where the electrochemical performance of planar, macroporous (pore size: 1200 nm), hierarchical (pore size: 1200 and 60 nm), and nanoporous (pore size: <50 nm) gold electrodes were investigated in the presence of BSA.[162] The time taken for the peak current for the reduction of ferricyanide to reach half its original value (prior to exposure to BSA) was 3, 12, and 38 min for planar, macroporous, and hierarchical gold electrodes, respectively. Interestingly, the NPG electrode showed an average decrease in the peak current of 12 ± 8% after an hour in the protein containing solution.[162] This antifouling property of NPG appears to be due to the nano porosity and high surface area. Fouling agents can readily adsorb onto the planar gold electrode surface, which is contact with bulk solution, however, fouling of the inner surface of NPG would be slower and more difficult due to restricted mass transport of large species through small pores.[116,162] This indicates that a pore size of <50 nm is required for effective fouling resistance to BSA or similar sized proteins.

The study conducted using fibrinogen as the fouling agent uses a relatively low concentration of fouling agent (1 mg/mL).[160] Fibrinogen typically exists at relatively high concentrations ($\sim$ 3 mg/mL) in blood plasma,[163] hence the concentrations used in this study, may not be representative of a real system.

Carbon-based electrodes are very popular for biological applications due to their biocompatibility and versatility.[164,165] These electrodes typically contain oxygen-based surface functional groups, such as aldehyde, ketones, alcohols, and carboxylic acids, making the surface inherently hydrophilic. Furthermore, the surface functionality can be tuned depending on the carbon material. For example, tetrahedral amorphous carbon (ta-C) was found to have significantly more carbonyl groups than pyrolytic carbon (PyC), which had an equal amount of ketone, hydroxyl and ether/epoxide groups.[166] Both ta-C and PyC electron transfer kinetics (measured via assessment of ΔE_p) for the reduction of $Ru(NH_3)_6^{3+}$ were shown to be unaffected by 2% BSA or undiluted fetal bovine serum (FBS). The electrode was immersed in the protein solutions for 30 mins at 37°C (and rinsed using phosphate buffered saline (PBS)) prior to conducting measurements (at room temperature). This is, however, not a true

representation of electrode fouling, since the measurements are not conducted *in situ*, and the PBS rinse may be removing some of fouling agent from the electrode surface. The ET kinetics of $IrCl_6^{2-}$ were affected by both fouling agents.[166] Both BSA and FBS are present in the overall negative charge state, hence this could be due to the electrostatic repulsion between the redox species and the anionically-charged proteins adsorbed on the electrode, and/or the stronger interaction of the proteins and the positive applied potential at the surface (although, the E_{pzc} of this material is not characterised).

Studying the effects of the most abundant proteins in the body is crucial for the evaluation of sensors for biological applications. However, it also important to consider the effects of multiple protein environments, that closely relates to real-world biological samples. In solutions such as blood serum, urine, sweat, and saliva, there are a range of molecules present in high concentrations and with different molecular weights. The protein in blood plasma can be classed in three board groups: globulins, fibrinogen, and albumins which is the most abundant of the three.[167] Saliva contains high concentrations of mucin, a glycoprotein, which is also secreted in the upper and middle portions of the stomach (along with pepsinogen).[167]

In an effort to improve the antifouling property of carbon electrodes, Siraj *et al.* recently reported a method of hydrogenating carbon electrodes by *n*-butylsilane reduction, that reduces the oxygen surface functional groups on the surface[168] to produce an antifouling hydrophobic electrode surface for dopamine detection.[169,170] The antifouling properties of these electrodes were explored in a synthetic fouling solution containing, 1% (v/v) caproic acid (a lipid), 4% (w/v) BSA and 0.01% (w/v) cytochrome c (both are proteins), and 0.002% (w/v) human fibrinopeptide B (a peptide). The detection of dopamine in this solution, using CV, a ~35 % decrease was observed in the dopamine oxidation peak after incubating the electrodes in the synthetic solution for 30 mins. After further incubation for a week, there was no further change in the dopamine signal. However, the non-hydrogenated carbon electrode completely lost all dopamine detection signal. A major challenge in dopamine detection *in vivo* is electrode fouling from amphiphilic proteins, lipids, and peptides present in the extracellular fluid irreversibly adsorbing on an oxygenated sp^2 carbon surface,

through dipole-dipole or ion dipole interactions, or hydrogen bonding, which will prevent dopamine from reaching the electrode surface for ET.[170] Hydrogenating the carbon surface, produces a sp[3]-enriched carbon surface, with reduced C-O functional groups, and C=O converted to C-H bonds.[169] The H-terminated surface has minimised the adsorption of biomolecules, and the siloxane dendrimers (from *n*-butylsilane reduction) sterically discourages large biomolecules from adsorption to the surface.[168]

1.4.3.2. Fast Scan Cyclic Voltammetry (FSCV)

FSCV is an electrochemical technique used for the detection of neurotransmitters on a sub-second timescale, and often used in combination with carbon-fibre microelectrodes (CFME).[171] The potential is ramped from a holding potential to a switching potential and back, usually at a 400 V s^{-1} scan rate and a frequency of 10 Hz (sub second temporal resolution).[172] Experiments must be performed at a microelectrode, due to the small time constant for fast capacitive charging.[173] Venton and Cao, recently published a critical review on the fundamentals of FSCV, which provides a detailed explanation of the technique FSCV as well as its well-known application for dopamine detection.[172]

There are several waveforms for FSCV, depending on the application.[174–178] Dunham and Venton recently reported a study on reducing electrode fouling and increasing serotonin sensitivity by extending the switching potential.[177] Figure 1.16 summaries the waveforms used in this study. To test electrode fouling, 25 repeated serotonin injections were conducted, for 5 s and every 30 s using flow injection analysis. A decrease in serotonin oxidation current from the current recorded in the first injection is recognised as CFME fouling. The Jackson waveform (Figure 1.16A), scans from 0.2 V, to switching potential 1 V to -0.1 V, then back to the holding potential of 0.2 V at 1000 V/s, was previously developed to reduce serotonin fouling.[179,180] However, this study showed that using this waveform, the electrodes were still fouling with a 39 ± 3% average current decrease. The dopamine waveform (Figure 1.16B) sweeps from -0.4 V to 1.3 V at 400 V/s,[181] showed no electrode fouling with only, 5 ± 2% current decrease compared to first injection, this is thought to be due to the negative holding potential. The antifouling nature of the dopamine waveform is due to the

extended switching potential of 1.3 V, which regenerates the carbon electrode surface, and the negative holding potential which reduces the adsorption of serotonin and its oxidation products. However, a positive holding potential (0.2 V) is necessary to attract serotonin to the surface.
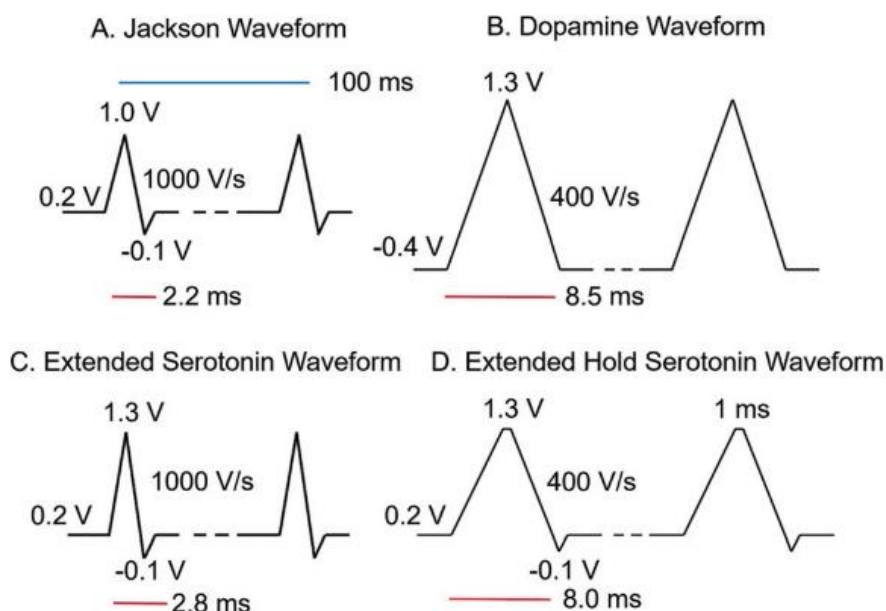
Figure 1.16. FSCV waveform that have been explored for reduced electrode fouling for the detection of serotonin. From Dunham and Venton.[177]

Hence, this study introduced two new waveforms based on a combination of the Jackson and dopamine waveforms, keeping the positive holding potential and the extended switching potential. Figure 1.16C shows the extended waveform (ESW) scans from 0.2 V to 1.3 V, then to -0.1 V and back to 0.2 V at 1000 V/s. Figure 1.16D shows the extended hold serotonin waveform (EHSW), which applies the same potential as extended waveform, but at a slower scan rate of 400 V/s. Both ESW and EHSW exhibited reduced fouling compared to Jackson waveform, with current decrease of 19 ± 2% and 18 ± 4%, respectively, with good sensitivity for serotonin.

In the example below the traditional CFME was compared to pristine CNT and functionalised CNT electrodes.[182] Functionalisation took place using an O_2 plasma, which is known to introduce oxygen functionalised groups (hydroxyl,

carbonyl, carboxyl) on the CNT surface.[183] It was confirmed by Raman, that the CFME and functionalised CNT electrodes have significantly higher sp^3/sp^2 ratios than the pristine CNT electrode. All electrodes were placed in brain tissue for 2 h without any waveform application, and tested using 1 μM dopamine prior to and after tissue exposure.[182] On average a 31 ± 15% reduction in dopamine current was observed for CFME, whereas, a 76 ± 4.6% and 42 ± 7.2% reduction in current was observed for pristine CNT and functionalised CNT, respectively. This study shows that careful consideration of the surface characteristics of the electrode is necessary to optimise electrodes for resistance to fouling.

1.4.3.3. Electrochemical Impedance Spectroscopy (EIS)

EIS is a powerful surface sensitive alternating current (AC) technique, which can inform on both faradaic and non-faradaic electrode processes.[2] EIS is able to distinguish between two or more electrochemical reactions, it can identify diffusion-limited reactions (e.g., diffusion through a passive film), and provide information on the capacitive behaviour of a system.[184–186] Generally, Nyquist plots are fitted to an EEC to extract quantitative information on the electrode/electrolyte interface. To model electrode behaviour when exposed to protein solutions, two types of EECs have commonly been used. Figure 1.17a shows the Randles circuits which has commonly been used to model solutions containing only proteins.[14,133,148,187] Figure 1.17b is the modified Randles circuit, which has been used to model solutions containing proteins and a metal redox couple[13,122,186,188] (e.g., ferri/ferrocyanide). The models contain certain elements including, C_{dl}, solution resistance (R_s), charge transfer resistance (R_{ct}), and a Warburg impedance (W) is introduced to model the diffusion process in the system. The C_{dl} can be replaced by a constant phase element (CPE), which accounts for any surface inhomogeneity between electrode and protein layers.[185,189,190]
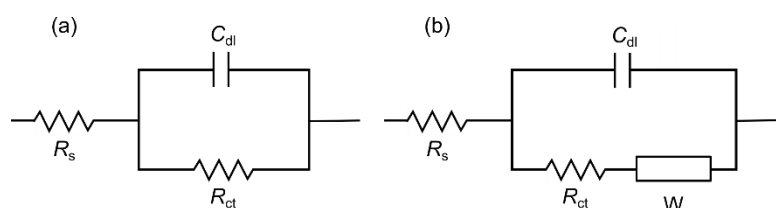
Figure 1.17. EEC models, (a) Randles circuit and (b) modified Randles circuit

Moulton *et al*., investigated the electrochemical behaviour of gold electrode exposed to HSA and immunoglobulin G (Ig.G) using EIS.[14] The PZC of the gold electrode was estimated to be -275 mV. Hence for potentials lower than -275 mV, the surface carries a negative charge, and potentials higher than -275 mV carries a positive charge. EIS measurements were recorded between 50 mHz and 100 kHz with AC amplitude of 10 mV, and the effect of protein interaction on the gold electrode was explored at three potentials, 400 mV, OCP (100 mV), and -400 mV. The resulting EIS spectra were fitted using the EEC shown in Figure 1.17a, with a CPE instead of C_{dl}. The C_{dl} decreased upon exposure to the proteins at all three potentials. The R_{ct} increased after exposure to Ig.G, this considered to be due to the formation of a continuous insulating layer on the gold surface, which is hinders ET of the ferricyanide couple in solution. Interestingly, the greatest C_{dl} decrease observed for both proteins were at or more positive to the electrode OCP, and under the same conditions, Ig.G caused a greater decrease in C_{dl} than HSA.[14] The decrease in capacitance is due to a fouling of the gold electrode surface.

MacDonald and Andreas, reported a method for determining the best EEC model for BSA adsorption on a Pt wire electrode.[13] The step first was to create a library of circuits that may model the physical processes occurring within the system. Then each circuit was fit to experimental data, and the relative residual errors from the circuit parameters relating to the physical parameters with the standard deviation from the repeat measurements were used to determine the best circuit. It was found that the modified Randles circuit (Figure 1.17b) models the experimental data in the absence of BSA (exposed to PBS for 20 h). After the electrode had been incubated in BSA (1 g/L) for 30 mins, then removed and EIS recorded in PBS with ferri/ferrocyanide over a 20 h time period, it was determined that a porous, insulating film of BSA is formed on the Pt electrode surface. To model this accurately an additional time constant (resistor and CPE in parallel) was required. EIS is only reasonable when the fitting parameters used represent the physical system being assessed.

Further to the models shown in Figure 1.17, Cobb and Macpherson used a *RC* circuit to model the time-dependent fouling observed on a BDD electrode in the presence of mucin (0.5 %).[191] The EIS data was compared with the C_{dl} values determined using current-time data from a SWV potential pulse sequence. Both techniques show a small but quantifiable decrease in capacitance, which can be attributed to electrode fouling from mucin adsorption.

1.5. IMPORTANCE OF pH SENSING IN THE BODY

The regulation of pH is critical to maintaining a healthy balance in biological environments. The pH of human organs, which ranges from 1 to 8, is carefully regulated by acid-based homeostasis[192] controlled by a variety of buffering agents.[193] The pH of blood and interstitial fluid (ISF) is normally between 7.35 and 7.45, and an acidosis or alkalosis event can be fatal. Respiratory compensation, which expels CO_2, and renal compensation, which secretes hydrogen ion, bicarbonate, and ammonia, keep blood pH stable.[193] Bicarbonate and ammonia are examples of extracellular buffers, whereas proteins, particularly histidine residues, and phosphate are examples of intracellular buffers.[193]

The healthy lung has a neutral pH, whereas the cystic fibrosis lung has an acidic pH.[194] When the pH of the lung environment is reduced, the activity of certain intracellular antimicrobials is inhibited, resulting in bacterial infection.[195] In the stomach, the proton pump hydrogen potassium ATPase exchanges H^+ for K^+, resulting in a highly acidic pH of 1.5-2.0, when it is empty.[196] This is required for both digestion and bacterial defence. Reduced acidity causes gastrointestinal (GI) infections; however, too much acid can cause stomach ulcers. Proton pump inhibitors (such as omeprazole) effectively raise stomach pH and protect against ulcers.[197]

pH changes in a biological system can be the cause or the result of disease and dysfunction. As a result, detecting this critical parameter is critical in disease detection and prevention. This section discusses advancements in electrochemical pH sensors for in-vivo and ex-vivo measurements of biological fluids. However, because biological pH sensing is a vast field of study, the examples provided below are only a few.

1.5.1. *Ex vivo* and biological fluids

Ex vivo electrochemical measurements are conducted outside the body. A major advantage for studying *ex vivo* tissue is that measurements that would not be easily possible in living organisms, can be explored in a controlled manner. Furthermore, prior to *in vivo* application of any sensor, *ex vivo* analysis can provide valuable information on sensor performance, before placing in patients through unnecessary treatments. Similar to *ex vivo* tissue, analysing bodily fluids can provide important information on diseases/physiology.

Chapter 3 explores the application of BDD-Q pH sensors for the real-time measurement of pH changes in the absence and presence of drugs such as, omeprazole, across an *ex vivo* upper GI tract tissue. Previously, BDD microelectrodes have been used to record the pH in a mouse stomach.[198] The pH sensing method is based on the potential change that is related to proton reduction (hydrogen evolution reaction) following an applied current.[199] However, this method lacked sensitivity, as any redox active species which is present and can be reduced/oxidised at the applied current will also be detected and can interfere with the proton reduction of interest.

Aside from *ex vivo* tissue pH measurements, carbon-based electrodes have also been used for the pH assessment of biological fluids. For example, Chaisiwamongkhol *et al*. investigated the pH in oxygenated saliva using a CFME, where the surface had been chemically oxidised to enrich the surface with pH responsive quinone groups.[200] A Nernstian response (-59 mV/pH) was observed across the pH range 2-8, which is appropriate for many biological fluids. The pH in both synthetic and authentic human saliva was also explored.[200] Performing the measurements at a high scan rate of 4 V/s was shown to remove any interference from the oxygen reduction reaction occurring on the sp^2 carbon surface. Hence, this approach provided a method that was capable of analysing real-world samples without any extra treatments (e.g., degassing).

IrOx pH sensors have been used extensively for physiological applications.[77,201–204] This is due to IrOx electrodes being cost-effective and allow for miniaturisation. Grant *et al*., reported the use of sputter coated IrOx pH sensor, for pH monitoring in human blood.[205] The stability of the IrOx sensor was assessed in PBS prior to placement in blood. Over the measurement time (85

mins), the response time was < 5 s, and showed minimal drift (< 0.4 mV/h). In blood, the pH response was linear in the tested range (6.5 to 8.2) with a sensitivity of -57.8 mV/pH unit. The response time for IrOx was < 5 s, however, the stability of the sensor for the duration of the measurement (3 h) is not shown.

Most IrOx pH sensors are operated under potentiometric mode, however, Chaisiwamongkhol *et al.*, recently reported the use of IrOx electrodeposited on iridium micro-disk electrode in voltammetric mode.[206] The pH response of the electrode in sheep's blood and uncertainty in the measurement was studied using both CV (± 0.07 pH units) and SWV (± 0.03 pH units). The IrOx pH sensor exhibited super-Nernstian response using both techniques. Section 1.1.4, discusses the difference between these two voltammetric techniques, and the ability of SWV to improve signal-to-noise ratio, reduces the uncertainty in the pH measurement, compared to CV.

Urine contains urea, uric acid, creatinine, and protons, which are important biomarkers for the diagnosis of various illnesses such as, kidney disease, electrolyte disorders, and urethritis.[204,207,208] Liu *et al.*, developed a graphite ink based electrochemical sensor capable of detecting multiple analytes: urea using OCP, and uric acid and pH using SWV.[209] The pH detection range was 4.0 to 8.0. In SWV, the oxidation peak current corresponds to the concentration of uric acid, the variation of pH causes a shift in the oxidation peak potential of uric acid, and this extent of shifting is the basis of the pH measurement. The sensitivity of pH detection in urine was 73 mV/pH. This work has produced a device that is portable, cost-effective, and user-friendly.[209]

1.5.2. In vivo

In vivo electrochemical sensors need to be minimally invasive and biocompatible to avoid any physiological immune response and tissue damage during measurement. This is particularly important for long-term measurements that can last for weeks or months. Sensor patches with micro spikes (~ 1 mm) for piercing the skin to the epidermis and gain access to the ISF have been explored as minimally invasive pH sensors for *in vivo* sensing.[210–214] The composition of ISF is claimed to be similar to blood serum, because of the equilibrium maintained between ISF and blood plasma by small molecules. Additionally,

surface fouling is significantly reduced for ISF compared to blood, because there is a lower concentration of proteins and other large molecules in ISF, hence sensors are suitable for long-term measurements.[210] A recent review by García-Guzmán *et al.*, provides a comprehensive summary of progress in microneedle based electrochemical sensors.[210]

Potentiometric pH sensors have been used *in vivo* to monitor the pH in rat brain,[215] bladder and cerebrospinal fluid (CSF).[216] A zinc oxide (ZnO) thin film on a tungsten (W) microneedle was used as the pH-sensitive electrode for *in vivo* pH measurement in the bladder and CSF.[216] The microneedles had a sensitivity of -46.35 mV/pH and was found to stabilise within 20 s in buffer solution. For the *in vivo* study, measurements were limited to 60 s to reduce pain to the animal. The pH measurements recorded using the ZnO pH needle sensor was compared to CSF and bladder urine collected separately and analysed using a commercial pH meter. The pH recorded using the commercial pH meter was higher than that recorded *in vivo*. The ZnO on W pH sensor was also found to have a limited working pH range from pH 2 – 9, and prolonged exposure to higher pH levels caused damage to the microneedle sensors.

For the real-time *in vivo* monitoring of rat brain pH, a gold-covered acupuncture (AN) needle with molybdenum disulfide (MoS_2) nanosheets deposited at the tip, with polyaniline (PAN/MoS_2/AN), was used.[215] The potentiometric PAN/MoS_2/AN microneedle exhibited a close to Nernstian response of -51.2 mV over the pH range of 3-9. The pH sensor was assessed in rat brains, while physically perturbing the pH with the addition of NaH_2PO_4 and Na_2CO_3. The pH sensor was able to successfully detect the changes in pH, however, only in a qualitative manner. Interestingly, the potential responses in phosphate buffer solution before and after implanting the electrode for 2 h, showed little fouling, with the potential stabilising within 100 s.

A non/minimally-invasive and safe approach to reach body fluids is to use ingestible devices.[217] These are mainly used to understand the physiology of the GI.[218,219] The Bravo system employs an antimony pH sensor to measure the pH of the GI tract.[220] The capsule lifetime is generally several days, and the *in vivo* tests have been conducted while the patients maintain their regular diets and daily activities. Recently, pH tests are increasingly being considered as the

benchmark for monitoring of gastric reflux, helping clinicians to diagnose and manage gastroesophageal reflux disorders.[221]

IrOx electrodeposited on screen-printed carbon electrode has been used in a wireless and ingestible capsule to monitor the pH in a dog's GI tract.[222] The pH sensor is flexible and was folded into the capsule (at a reduced volume). For the *in vivo* study, the capsule was in the dog's body for 48 h, there was no obvious damage present in the GI tract from the capsule. The IrOx sensor showed good sensitivity, -74.37 mV/pH, and the sensor was calibrated before and after *in vivo* measurements, showing minimal fouling in the pH response. The fabrication of the IrOx has a significant effect on the sensitivity. A study using an IrOx sensing film formed on a single polyimide substrate by sol-gel, dip coating and thermal oxidation process, showed near-Nernstian sensitivity between -51.1 and 51.7 mV/pH.[202] The system was assessed *in vivo* by implanting the sensor to the oesophageal wall of a live pig, and the IrOx pH sensor response showed good agreement with the commercial Bravo (antimony) system.[202]

Further to measuring pH, the capsule can also provide fundamental information on the physiology of the GI tract, for example, Kuo *et al*. showed that there is correlation (r = 0.73) between food leaving the stomach to the capsule leaving the stomach.[223] Therefore, the pH capsules have also been used to assess the passage time of the GI tract as a whole or individual organs for disorders related to the upper GI tract, constipation, and idiopathic gastroparesis in diabetic patients (delayed gastric emptying). It was also shown that in constipated patients, the transit time in the colon and the gastric emptying time were significantly delayed.[224]

Although ingestible sensors have been extremely valuable in understanding the physiological of the GI tract, and the adsorption of drugs, such as, omeprazole, a proton pump inhibitor,[197] there are still some limitations that need to be addressed. Firstly, determining the location of the sensor in the GI tract is problematic, even though tracking the pH can inform on the emptying of the stomach, it is often uncertain and unreliable.[225] While the stomach is empty, it is possible that bicarbonate from the duodenum can enter the stomach, causing a pH change for at least a short time, that can accidently be interpreted as the capsule entering the duodenum. Furthermore, ingestible sensors are disposable,

making it expensive and not sustainable. Drifting sensor data, inaccurate transmission, or a loss of data transmission due to sensor and recorder being too far apart, can lead to data losses or inaccurate data interpretation.[225]

Quinone-modified carbon paste electrode has been applied *in vivo* for the pH monitoring in a rat hindlimb, to inform on tissue ischaemic injury (reduced blood flow to tissue).[226] The carbon paste electrode was modified by electrodepositing the diazonium salt, 4-Benzoylamino-2, 5-dimethoxybenzenediazonium chloride – hemi zinc chloride. This sensor has shown Nernstian behaviour over the physiological pH range 7.2-7.6. For *in vivo* testing, linear sweep voltammetry was used to cycle the potential range -0.7 to +0.8 V *vs* Ag|AgCl over a 45 min period to establish a baseline. Ischaemia was induced by placing a tourniquet around the rat's limb, and pulling as tightly as possible, this was maintained for 10 mins, after which the tourniquet was removed, and measurements continued for 45 mins. Before and after implantation calibrations showed no significant difference. However, the voltammograms in phosphate buffer for pre and post implantation show a loss in quinone peak resolution (broadening of the peak). Furthermore, scanning electron microscopy images of the surface showed that the smooth carbon paste electrode surface seen prior to implantation had changed to an uneven, concave shape. This is an indication of electrode instability and biofouling occurring at the surface of the electrode.

1.6. AIMS

This thesis aims to assess electrochemical pH sensors for their application in biological systems, with a particular focus on understanding the performance properties of the pH electrode and the impact of biological fouling, specifically protein adsorption on the electrode surface.

The use of electrochemical sensors for *ex vivo* tissue pH measurements can be challenging, as there are stringent requirements for an ideal pH sensor, such as, the temporal and spatial resolution of measurements, robustness of the electrode etc. Chapter 3 aims address these requirements and determine the most suitable electrochemical pH sensor technology that can be used to map the pH profile in the GI tract of a mouse in the absence and presence of omeprazole, a proton pump inhibitor, and melatonin a bicarbonate agonist and acid inhibitor.

Chapter 4 explores the impact of proteins adsorption (0.5% mucin, and 5% BSA) on electrochemical processes on three carbon-based electrodes. In particular, (i) the voltammetry of common redox species ($Ru(NH_3)_6^{3+}$, $IrCl_6^{2-}$) as a function of time, (ii) the use of double layer capacitance measurements to provide information of the state of electrode surface (iii) the impact protein adsorption can have on a surface sensitive process, such as the electrodeposition of silver.

Chapter 5 focuses on the development of a 3D printed flow cell that can incorporate glass sealed BDD electrodes, along with reference and counter electrodes. The flow rate characteristics are explored using a standard redox couple ($Ru(NH_3)_6^{3+}$). Replacing the BDD electrode with both an IrOx and BDD-Q pH electrode allows assessment of the impact of the flow rate on the measured pH values for both IrOx and BDD-Q pH sensors. Finally, flow is explored as a method for eliminating or reducing the biofouling observed on IrOx and BDD-Q electrodes in Chapter 3, in the presence of mucin, and BSA. The findings from the protein investigation are used to conduct pH measurements in the more complex media of blood, under stationary and flow conditions (at three flow rates, 1, 10, and 100 mL/min).

Finally, Chapter 6 summaries the work presented in this thesis and discusses some directions for future work.

1.7. REFERENCES

1   C. M. A. Brett and A. M. O. Brett, Electrochemistry Principles, Methods, and Applications, 1994.

2   A. J. Bard and L. R. Faulkner, Electrochemical Methods Fundamentals and Applications, John Wiley & Sons, 2001.

3   W. J. Albery, Philosophical Transactions of the Royal Society of London. Series A, Mathematical and Physical Sciences, 1981, 302, 221–235.

4   M. Khademi and D. P. J. Barz, Langmuir, 2020, 36, 4250–4260.

5   J. Newman and N. P. Balsara, Electrochemical Systems, John Wiley & Sons, Fourth Edi., 2021.

6   J. Wang, Analytical electrochemistry, 2006.

7   A. M. Bond, R. G. Compton, D. A. Fiedler, G. Inzelt, H. Kahlert, S. Komorsky-Lovric, H. Lohse, M. Lovric, F. Marken, A. Neudeck, U. Retter, F. Scholz and Z. Stojek, Electroanalytical Methods, Guide to Experiments and Applications 2nd, revised and extended edition, 2010.

8   A. M. Bond, R. G. Compton, D. A. Fiedler, G. Inzelt, H. Kahlert, S. Komorsky-Lovric, H. Lohse, M. Lovric, F. Marken, A. Neudeck, U. Retter, F. Scholz and Z. Stojek, Electroanalytical Methods, Guide to Experiments and Applications 2nd, revised and extended edition, 2010.

9   A. Allagui, H. Benaoum and O. Olendski, Physica A: Statistical Mechanics and its Applications, 2021, 582, 126252.

10   A. W. Colburn, K. J. Levey, D. O'Hare and J. V Macpherson, Physical Chemistry Chemical Physics, 2021, 23, 8100–8117.

11   D. M. Morales and M. Risch, JPhys Energy, 2021, 3, 034013.

12   A. S. Bandarenka, Analyst, 2013, 138, 5540–5554.

13   M. A. Macdonald and H. A. Andreas, Electrochim Acta, 2014, 129, 290–299.

14   S. E. Moulton, J. N. Barisci, A. Bath, R. Stella and G. G. Wallace, Electrochim Acta, 2004, 49, 4223–4230.

15   S. Yuan and S. Hu, Electrochim Acta, 2004, 49, 4287–4293.

16   A. Świetlow, M. Skoog and G. Johansson, Electroanalysis, 1992, 4, 921–928.

17   C. Amatore, K. Besenhard, D. Evans, M. Fleischmann, S. Fletcher, J. Heinze, R. Murray, K. Oldham, J. Osteryoung, D. Pletcher, S. Pons, J. Saveant, B. Scharifker, R. M. Wightman and D. Williams, Microelectrodes: Theory and Applications, 1991.

18   S. Pons and M. Fleischmann, Anal Chem, 1987, 59, 1391–1399.

19   R. G. Compton and C. E. Banks, Understanding Voltammetry, 2007.

20   B. Rehm, D. Consultant, A. Haghshenas, A. S. Paknejad and J. Schubert, in Managed Pressure Drilling, Gulf Publishing Company, 2008, pp. 39–80.

21   N. W. Ryan and M. M. Johnson, AIChE Journal, 1959, 5, 433–435.

22   R. G. Compton and P. R. Unwin, J Electroanal Chem Interfacial Electrochem, 1986, 205, 1–20.

23   M. E. Snowden, P. H. King, J. A. Covington, J. V. MacPherson and P. R. Unwin, Anal Chem, 2010, 82, 3124–3131.

24   A. B. V. Metrohm, Autolab Application Note, 2011, 1–2.

25   M. Seralathan, R. A. Ostbryoung and J. G. Ostbryoung, 1987, 222, 69–100.

26   A. Bott, Curr Sep, 1997, 16, 23–26.

27   N. Elgrishi, K. J. Rountree, B. D. McCarthy, E. S. Rountree, T. T. Eisenhart and J. L. Dempsey, J Chem Educ, 2018, 95, 197–206.

28   R. S. Nicholson and I. Shain, Anal Chem, 1964, 36, 1212.

29   O. Fischer and E. Fischerová, in Experimental Techniques in Bioelectrochemistry, eds. V. Brabec, D. Walz and G. Milazzo, Springer Basel AG, 1996, pp. 41–157.

30   V. Mirceski, S. Komorsky-Lovric and M. Lovric, Eds., Square Wave Voltammetry: Theory and Application, Springer, 2007.

31   J. G. Osteryoung and R. A. Osteryoung, Anal Chem, 1985, 57, 101–110.

32   B. Uslu, The Open Chemical and Biomedical Methods Journal, 2011, 3, 56–73.

33   J. Osteryoung, J Chem Educ, 1983, 60, 296–298.

34   C. G. Zoski, Handbook of electrochemistry, 2007.

35   P. T. Kissinger and W. R. Heineman, Eds., Laboratory techniques in electroanalytical chemistry, Marcel Dekker Inc., 1996.

36   Ø. Mikkelsen and K. H. Schrøder, Electroanalysis, 2003, 15, 679–687.

37   A. S. Boyd, D. Seger, S. Vannucci, M. Langley, J. L. Abraham and L. E. King, J Am Acad Dermatol, 2000, 43, 81–90.

38   V. Vyskočil and J. Barek, Crit Rev Anal Chem, 2009, 39, 173–188.

39   H. Angerstein-Kozlowska, B. E. Conway and W. B. A. Sharp, Electroanalytical chemistry and interfacial electrochemistry, 1973, 43, 9–36.

40   A. A. Topalov, S. Cherevko, A. R. Zeradjanin, J. C. Meier, I. Katsounaros and K. J. J. Mayrhofer, Chem Sci, 2014, 5, 631–638.

41   D. Chen, L. Tang and J. Li, Chem Soc Rev, 2010, 39, 3157–3180.

42   A. J. S. Ahammad, T. Islam and M. M. Hasan, Graphene-based electrochemical

sensors for biomedical applications, Elsevier Inc., 2019.

43   W. Zhang, S. Zhu, R. Luque, S. Han, L. Hu and G. Xu, Chem Soc Rev, 2016, 45, 715–752.

44   R. L. McCreery, Chem Rev, 2008, 108, 2646–2687.

45   A. Morteza Najarian, R. Chen, R. J. Balla, S. Amemiya and R. L. McCreery, Anal Chem, 2017, 89, 13532–13540.

46   H. V. Patten, K. E. Meadows, L. A. Hutton, J. G. Iacobini, D. Battistel, K. McKelvey, A. W. Colburn, M. E. Newton, J. V. MacPherson and P. R. Unwin, Angewandte Chemie - International Edition, 2012, 51, 7002–7006.

47   Y. Zou, A. S. Walton, I. A. Kinloch and R. A. W. Dryfe, Langmuir, 2016, 32, 11448–11455.

48   Z. Li, A. Kozbial, N. Nioradze, D. Parobek, G. J. Shenoy, M. Salim, S. Amemiya, L. Li and H. Liu, ACS Nano, 2016, 10, 349–359.

49   N. Nioradze, R. Chen, N. Kurapati, A. Khvataeva-Domanov, S. Mabic and S. Amemiya, Anal Chem, 2015, 87, 4836–4843.

50   M. Hersey, S. N. Berger, J. Holmes, A. West and P. Hashemi, Anal Chem, 2019, 91, 27–43.

51   K. J. Klunder, Z. Nilsson, J. B. Sambur and C. S. Henry, J Am Chem Soc, 2017, 139, 12623–12631.

52   E. M. Akinoglu, E. Kätelhön, J. Pampel, Z. Ban, M. Antonietti, R. G. Compton and M. Giersig, Carbon N Y, 2018, 130, 768–774.

53   G. G. Wildgoose, C. E. Banks, H. C. Leventis and R. G. Compton, Microchimica Acta, 2006, 152, 187–214.

54   J. E. Graebner, in Diamond: Electronic Properties and Applications, 1995, pp. 285–318.

55   R. S. Balmer, J. R. Brandon, S. L. Clewes, H. K. Dhillon, J. M. Dodson, I. Friel, P. N. Inglis, T. D. Madgwick, M. L. Markham, T. P. Mollart, N. Perkins, G. A. Scarsbrook, D. J. Twitchen, A. J. Whitehead, J. J. Wilman and S. M. Woollard, J. Phys.: Condens. Matter, 2009, 21, 364221–364245.

56   J. V. Macpherson, Physical Chemistry Chemical Physics, 2015, 17, 2935–2949.

57   X. Blase, E. Bustarret, C. Chapelier, T. Klein and C. Marcenat, Nat Mater, 2009, 8, 375–382.

58   A. Fujishima, Y. Einaga, T. N. Rao, D. A. Tryk and I. T. Anggraningrum, Diamond Electrochemistry, First Edition, Elsevier, 2005.

59   E. Brillas and C. A. Martinez-Huitle, Eds., Synthetic Diamond Films: Preparation, Electrochemistry, Characterisation, and Applications, John Wiley & Sons, 2011.

60   Z. J. Ayres, PhD Thesis, University of Warwick, 2017.

61   L. A. et al. Hutton, J. G. Iacobini, E. Bitziou, R. B. Channon, M. E. Newton and J. V Macpherson, Anal Chem, 2013, 85, 7230–7240.

62   S. J. Cobb, Z. J. Ayres and J. V Macpherson, Annual Review of Analytical Chemistry, 2018, 11, 463–484.

63   Z. Deng, R. Zhu, L. Ma, K. Zhou, Z. Yu and Q. Wei, Carbon N Y, 2022, 196, 923–939.

64   T. Watanabe, Y. Honda, K. Kanda and Y. Einaga, Physica Status Solidi (A) Applications and Materials Science, 2014, 211, 2709–2717.

65   H. B. Martin, A. Argoitia, U. Landau, A. B. Anderson and J. C. Angus, J. Electrochem. Soc.

66   D. Medeiros De Araújo, P. Cañizares, C. A. Martínez-Huitle and M. A. Rodrigo, Electrochem commun, 2014, 47, 37–40.

67   O. Sarakhman and Ľ. Švorc, Crit Rev Anal Chem, 2022, 52, 791–813.

68   J. P. De Paiva Barreto, K. C. De Freitas Aráujo, D. M. De Aráujo and C. A. Martínez-Huitle, ECS Electrochemistry Letters, 2015, 4, E9–E11.

69   K. Muzyka, J. Sun, T. H. Fereja, Y. Lan, W. Zhang and G. Xu, Analytical Methods, 2019, 11, 397–414.

70   J. J. Tully, Z. Zhang, I. M. Terrero Rodríguez, L. Butcher and J. V Macpherson, Anal Chem, 2022, 94, 9856–9862.

71   A. J. Lucio, R. E. Meyler, M. A. Edwards and J. V Macpherson, 2020, 5, 789–797.

72   A. J. Lucio and J. V Macpherson, Anal Chem, 2020, 92, 16072–16078.

73   I. Feldman, Anal Chem, 1956, 28, 1859–1866.

74   B. D. Meshram, A. K. Agrawal, S. Adil, S. Ranvir and K. K. Sande, Int J Curr Microbiol Appl Sci, 2018, 7, 3305–3324.

75   J. L. Smith and J. W. Doran, in Methods for Assessing Soil Quality, 1996, pp. 169–185.

76   M. H. Banna, H. Najjaran, R. Sadiq, S. A. Imran, M. J. Rodriguez and M. Hoorfar, Sens Actuators B Chem, 2014, 193, 434–441.

77   M. T. Ghoneim, A. Nguyen, N. Dereje, J. Huang, G. C. Moore, P. J. Murzynowski and C. Dagdeviren, Chem Rev, 2019, 119, 5248–5297.

78   D. Daomin Zhou, Microelectrodes for in-vivo determination of pH, Elsevier Inc., 2008.

79   D. J. Graham, B. Jaselskis and C. E. Moore, J Chem Educ, 2013, 90, 345–351.

80   S. Licht, Anal Chem, 1985, 57, 514–519.

81   L. Manjakkal, D. Szwagierczak and R. Dahiya, Prog Mater Sci, 2020, 109.

82   S. Głab, A. Hulanicki, E. Gunnar and F. Ingman, Crit Rev Anal Chem, 1989, 21, 29–47.

83   A. Fog and R. P. Buck, Sensors and Actuators, 1984, 5, 137–146.

84   R. H. G. G. Mingels, S. Kalsi, Y. Cheong and H. Morgan, Sens Actuators B Chem, 2019, 297, 126779.

85   S. Kakooei, C. Ismail and B. Ari-Wahjoedi, International Journal of Material Science Innovations (IJMSI), 2013, 1, 62–72.

86   P. Kurzweil, Sensors, 2009, 9, 4955–4985.

87   K. Kreider, Sens Actuators B Chem, 1991, 5, 165–169.

88   T. Katsube, I. Lauks and J. N. Zemel, Sensors and Actuators, 1982, 2, 399–410.

89   R. D. Meyer, S. F. Cogan, T. H. Nguyen and R. D. Rauh, IEEE Transactions on Neural Systems and Rehabilitation Engineering, 2001, 9, 2–11.

90   Y. J. Kim, Y. C. Lee, B. K. Sohn, J. H. Lee and C. S. Kim, Journal of the Korean Physical Society, 2003, 43, 769–772.

91   D. O'Hare, K. H. Parker and C. P. Winlove, Med Eng Phys, 2006, 28, 982–988.

92   M. Yuqing, G. Jianguo and C. Jianrong, Biotechnol Adv, 2003, 21, 527–534.

93   M. Yuqing, C. Jianrong and F. Keming, J Biochem Biophys Methods, 2005, 63, 1–9.

94   P. Bergveld, Sens Actuators B Chem, 2003, 88, 1–20.

95   R. A. Rani and O. Sidek, IEEE Region 10 Annual International Conference, Proceedings/TENCON, 2004, D, 660–663.

96   V. K. Khanna, Sensor Review, 2007, 27, 233–238.

97   M. Lu and R. G. Compton, Analyst, 2014, 139, 4599–4605.

98   M. Lu and R. G. Compton, Analyst, 2014, 139, 2397–2403.

99   H. Kahlert, Journal of Solid State Electrochemistry, 2008, 12, 1255–1266.

100   H. Gomathi and G. Prabhakara Rao, Journal of Electroanalytical Chemistry, 1985, 190, 85–94.

101   A. P. Brown, C. Koval and F. C. Anson, Journal of Electroanalytical Chemistry, 1976, 72, 379–387.

102   É. Szepesváry and E. Pungor, Anal Chim Acta, 1971, 54, 199–208.

103   P. Allongue, M. Delamar, B. Desbat, O. Fagebaume, R. Hitmi, J. Pinson and J. M. Savéant, J Am Chem Soc, 1997, 119, 201–207.

104   I. Streeter, H. C. Leventis, G. G. Wildgoose, M. Pandurangappa, N. S. Lawrence, L.

Jiang, T. G. J. Jones and R. G. Compton, Journal of Solid State Electrochemistry, 2004, 8, 718–721.

105   J. Jacq, Electrochim Acta, 1967, 12, 1345–1361.

106   E. Laviron, Journal of Electroanalytical Chemistry, 1984, 164, 213–227.

107   P. S. Guin, S. Das and P. C. Mandal, International Journal of Electrochemistry, 2010, 2011, 22.

108   C. Costentin, Chem Rev, 2008, 108, 2145–2179.

109   R. S. Kim and T. D. Chung, Bull Korean Chem Soc, 2014, 35, 3143–3155.

110   M. Quan, D. Sanchez, M. F. Wasylkiw and D. K. Smith, J Am Chem Soc, 2007, 129, 12847–12856.

111   Z. J. Ayres, A. J. Borrill, J. C. Newland, M. E. Newton and J. V Macpherson, Anal. Chem., 2016, 88, 974–980.

112   S. J. Cobb, Z. J. Ayres, M. E. Newton and J. V. Macpherson, J Am Chem Soc, 2019, 141, 1035–1044.

113   T. L. Read, S. J. Cobb and J. V Macpherson, ACS. Sens., 2019, 4, 756–763.

114   T. Rajan, T. Read, A. Abdalla, B. Patel and J. Macpherson, ACS Sens, 2020, 5, 2858–2865.

115   C. E. Banks, T. Killard and B. J. Venton, Analytical Methods, 2019, 10, 2736.

116   B. L. Hanssen, S. Siraj and D. K. Y. Wong, Rev Anal Chem, 2016, 35, 1–28.

117   A. Barfidokht and J. J. Gooding, Electroanalysis, 2014, 26, 1182–1196.

118   J. Y. Lichtenberg, Y. Ling and S. Kim, Sensors, 2019, 19, 2488.

119   A. N. Raditya and D. O'Hare, J Electrochem Soc, 2020, 167, 127503.

120   L. J. Simcox, R. P. A. Pereira, E. M. H. Wellington and J. V. Macpherson, ACS Appl Mater Interfaces, 2019, 11, 25024–25033.

121   C. Dai, L. P. Crawford, P. Song, A. C. Fisher and N. S. Lawrence, RSC Adv, 2015, 5, 104048–104053.

122   R. Trouillon and D. O'Hare, Electrochim Acta, 2010, 55, 6586–6595.

123   A. Fagan-Murphy, F. Watt, K. A. Morgan and B. A. Patel, Journal of Electroanalytical Chemistry, 2012, 684, 1–5.

124   C. D. Allred and R. L. McCreery, Anal Chem, 1992, 64, 444–448.

125   A. N. Patel, P. R. Unwin and J. V. MacPherson, Physical Chemistry Chemical Physics, 2013, 15, 18085–18092.

126   C. Jiang, G. Wang, R. Hein, N. Liu, X. Luo and J. J. Davis, Chem Rev, 2020, 120, 3852–3889.

127   J. L. Harding and M. M. Reynolds, Trends Biotechnol, 2014, 32, 140–146.

128   M. Malmsten, D. Muller and B. Lassen, J Colloid Interface Sci, 1997, 193, 88–95.

129   C. Sperling, M. Fischer, M. F. Maitz and C. Werner, Biomaterials, 2009, 30, 4447–4456.

130   P. Silva-Bermudez and S. E. Rodil, Surf Coat Technol, 2013, 233, 147–158.

131   M. Rabe, D. Verdes and S. Seeger, Adv Colloid Interface Sci, 2011, 162, 87–106.

132   B. A. Patel, Electrochemistry for Bioanalysis, 2021.

133   A. R. Harris, P. Carter, R. Cowan and G. G. Wallace, ChemElectroChem, 2021, 8, 1078–1090.

134   R. A. Latour, Colloids Surf B Biointerfaces, 2020, 191, 110992.

135   A. Quinn, H. Mantz, K. Jacobs, M. Bellion and L. Santen, EPL, 2008, 81, 56003.

136   S. J. Attwood, R. Kershaw, S. Uddin, S. M. Bishop and M. E. Welland, J Mater Chem B, 2019, 7, 2349–2361.

137   B. Jachimska, M. Wasilewska and Z. Adamczyk, Langmuir, 2008, 24, 6867–6872.

138   R. Bansil and B. S. Turner, Curr Opin Colloid Interface Sci, 2006, 11, 164–170.

139   M. G. E. G. Bremer, J. Duval, W. Norde and J. Lyklema, Colloids Surf A Physicochem Eng Asp, 2004, 250, 29–42.

140   T. E. Benavidez and C. D. Garcia, Langmuir, 2013, 29, 14154–14162.

141   S. Demanèche, J. P. Chapel, L. J. Monrozier and H. Quiquampoix, Colloids Surf B Biointerfaces, 2009, 70, 226–231.

142   Z. G. Peng, K. Hidajat and M. S. Uddin, J Colloid Interface Sci, 2004, 271, 277–283.

143   J. Hu, S. Li and B. Liu, Biochem Eng J, 2005, 23, 259–263.

144   J. Wang, D. Wang and N. Hui, Bioelectrochemistry, 2020, 136, 107595.

145   J. Xu and H. Lee, Chemosensors, 2020, 8, 1–29.

146   P. Bevilacqua, S. Nuzzo, E. Torino, G. Condorelli, M. Salvatore and A. M. Grimaldi, Nanomaterials, 2021, 11, 1–19.

147   K. Nakanishi, T. Sakiyama and K. Imamura, J Biosci Bioeng, 2001, 91, 233–244.

148   D. R. Jackson, S. Omanovic and S. G. Roscoe, Langmuir, 2000, 16, 5449–5457.

149   R. Rouhana, S. M. Budge, S. M. MacDonald and S. G. Roscoe, Food Research International, 1997, 30, 13–20.

150   S. Fukuzaki, H. Urano and K. Nagata, J Ferment Bioeng, 1995, 80, 6–11.

151   M. Rabe, D. Verdes, J. Zimmermann and S. Seeger, Journal of Physical Chemistry B, 2008, 112, 13971–13980.

152   F. Fang and I. Szleifer, Journal of Chemical Physics, 2003, 119, 1053–1065.

153   J. N. Israelachvili, Intermolecular and surface forces, Elsevier, Third., 2011.

154   A. J. Downard and A. D. Roddick, Electroanalysis, 1995, 7, 376–378.

155   T. Thomas, R. J. Mascarenhas, O. J. D. Souza, P. Martis, J. Dalhalle and B. E. K. Swamy, J Colloid Interface Sci, 2013, 402, 223–229.

156   A. H. Jesmer and R. G. Wylie, Front Chem, 2020, 8, 604236.

157   Q. Wei, T. Becherer, S. Angioletti-Uberti, J. Dzubiella, C. Wischke, A. T. Neffe, A. Lendlein, M. Ballauff and R. Haag, Angewandte Chemie - International Edition, 2014, 53, 8004–8031.

158   M. Hedayati, D. Krapf and M. J. Kipper, J Colloid Interface Sci, 2021, 589, 356–366.

159   G. F. Wood, C. E. Zvoriste-Walters, M. G. Munday, M. E. Newton, V. Shkirskiy, P. R. Unwin and J. V. Macpherson, Carbon N Y, 2021, 171, 845–856.

160   R. K. Khan, V. K. Yadavalli and M. M. Collinson, ChemElectroChem, 2019, 6, 4660–4665.

161   S. E. Moulton, J. N. Barisci, A. Bath, R. Stella and G. G. Wallace, J Colloid Interface Sci, 2003, 261, 312–319.

162   J. Patel, L. Radhakrishnan, B. Zhao, B. Uppalapati, R. C. Daniels, K. R. Ward and M. M. Collinson, Anal Chem, 2013, 85, 11610–11618.

163   T. A. Horbett, J Biomed Mater Res A, 2018, 106A, 2777–2788.

164   S. Hu and C. Hu, J Sens, 2009, 187615, 1–40.

165   P. Joshi, R. Mishra and R. J. Narayan, Curr Opin Biomed Eng, 2021, 18, 100274.

166   E. Peltola, A. Aarva, S. Sainio, J. J. Heikkinen, N. Wester, V. Jokinen, J. Koskinen and T. Laurila, Physical Chemistry Chemical Physics, 2020, 22, 16630–16640.

167   E. P. Widmaier, H. Raff and K. T. Strang, in Vander's Human Physiology, The Mechanisms of Body Function, McGraw-Hill Higher Education, 11th edn., 2008, pp. 528–565.

168   R. Roshni, C. R. McRae and D. K. Y. Wong, Diam Relat Mater, 2021, 114, 108322.

169   S. Siraj, C. R. McRae and D. K. Y. Wong, Electrochim Acta, 2019, 305, 137–144.

170   S. Siraj, C. R. McRae and D. K. Y. Wong, Sens Actuators B Chem, 2021, 327, 128881.

171   M. L. Huffman and B. J. Venton, Analyst, 2009, 134, 18–24.

172   B. J. Venton and Q. Cao, Analyst, 2020, 145, 1158–1168.

173   R. M. Wightman, Anal Chem, 1981, 53, 1125A-1134A.

174   S. E. Calhoun, C. J. Meunier, C. A. Lee, G. S. McCarty and L. A. Sombers, ACS Chem Neurosci, 2019, 10, 2022–2032.

175   M. T. Cryan and A. E. Ross, Anal Chem, 2019, 91, 5987–5993.

176   P. Puthongkham and B. J. Venton, Analyst, 2020, 145, 1087–1102.

177   K. E. Dunham and B. J. Venton, Analyst, 2020, 145, 7437–7446.

178   Y. Li, C. M. Fleischer and A. E. Ross, Chemical Communications, 2020, 56, 8023–8026.

179   B. P. Jackson, S. M. Dietz and R. M. Wightman, Anal. Chem, 1995, 67, 1115–1120.

180   P. Hashemi, E. C. Dankoski, J. Petrovic, R. B. Keithley and R. M. Wightman, Anal Chem, 2009, 81, 9462–9471.

181   M. L. A. V. Heien, P. E. M. Phillips, G. D. Stuber, A. T. Seipel and R. M. Wightman, Analyst, 2003, 128, 1413–1419.

182   M. E. Weese, R. A. Krevh, Y. Li, N. T. Alvarez and A. E. Ross, ACS Sens, 2019, 4, 1001–1007.

183   R. Malik, C. McConnell, N. T. Alvarez, M. Haase, S. Gbordzoe and V. Shanov, RSC Adv, 2016, 6, 108840–108850.

184   B.-Y. Chang and S.-M. Park, The Annual Review of Analytical Chemistry is online Annual Rev. Anal. Chem, 2010, 3, 207–229.

185   E. P. Randviir and C. E. Banks, Analytical Methods, 2013, 5, 1098–1115.

186   Y. Huang, A. Hara, C. Terashima, A. Fujishima and M. Takai, Carbon N Y, 2019, 152, 354–362.

187   M. Farcas, N. P. Cosman, D. K. Ting, S. G. Roscoe and S. Omanovic, Journal of Electroanalytical Chemistry, 2010, 649, 206–218.

188   X. Yang, J. Kirsch, J. Fergus and A. Simonian, Electrochim Acta, 2013, 94, 259–268.

189   D. B. Xochitl, S. Sevda, K. Vanbroekhoven and D. Pant, Chem Soc Rev, 2012, 41, 7228–7246.

190   T. Nakamura, K. Homma and K. Tachibana, Ann Biomed Eng, 1992, 20, 289–305.

191   S. J. Cobb and J. V. Macpherson, Anal Chem, 2019, 91, 7935–7942.

192   E. Proksch, Journal of Dermatology, 2018, 45, 1044–1052.

193   H. Ashfaq, Ed., Handbook of Blood Gas / Acid-Base Interpretation, Springer, Second edi., 2013.

194   D. Mcshane, J. C. Davies, M. G. Davies, A. Bush, D. M. Geddes and E. W. F. W. Alton, 2003, 37–42.

195   A. A. Pezzulo, X. X. Tang, M. J. Hoegger, M. H. Abou Alaiwa, S. Ramachandran, T. O. Moninger, P. H. Karp, C. L. Wohlford-Lenane, H. P. Haagsman, M. Van Eijk, B. Bánfi, A. R. Horswill, D. A. Stoltz, P. B. McCray, M. J. Welsh and J. Zabner, Nature, 2012, 487, 109–113.

196   G. Sachs and B. Wallmark, Scand J Gastroenterol, 1989, 24, 3–11.

197   P. Lindberg, A. Brndstrm, B. Wallmark, H. Mattsson, L. Rikner and K. J. Hoffmann, Med Res Rev, 1990, 10, 1–54.

198   S. Fierro, R. Seishima, O. Nagano, H. Saya and Y. Einaga, Sci Rep, 2013, 3, 3257.

199   S. Fierro, N. Mitani, C. Comninellis and Y. Einaga, Physical Chemistry Chemical Physics, 2011, 13, 16795–16799.

200   K. Chaisiwamongkhol, C. Batchelor-Mcauley and R. G. Compton, Analyst, 2017, 142, 2828–2835.

201   E. Prats-Alfonso, L. Abad, N. Casañ-Pastor, J. Gonzalo-Ruiz and E. Baldrich, Biosens Bioelectron, 2013, 39, 163–169.

202   H. Cao, V. Landge, U. Tata, Y.-S. Seo, S. Rao, S.-J. Tang, H. F. Tibbals, S. Spechler and J.-C. Chiao, IEEE Trans Biomed Eng, 2012, 59, 3131–3139.

203   Z. Zulkarnay, S. Shazwani, B. Ibrahim, A. J. Jurimah, A. R. Ruzairi and S. Zaridah, An overview on pH measurement technique and application in biomedical and industrial process, Proceedings - 2nd International Conference on Biomedical Engineering, ICoBE, 2015.

204   S. Fan, S. Khuntia, C. H. Ahn, B. Zhang and L. Tai, Chemosensors, 2022, 10, 22.

205   S. A. Grant, K. Bettencourt, P. Krulevitch, J. Hamilton and R. Glass, Sens Actuators B Chem, 2001, 72, 174–179.

206   K. Chaisiwamongkhol, C. Batchelor-Mcauley and R. G. Compton, Analyst, 2019, 144, 1386.

207   F. Bernal-Reyes, M. Acosta-Elias, A. J. Burgara-Estrella, O. Alvarez-Bajo, O. I. Gavotto-Nogales, F. J. Antunez-Dominguez, L. Placencia-Camacho and H. M. Sarabia-Sainz, Instrum Sci Technol, 2020, 48, 361–375.

208   H. Y. Y. Nyein, W. Gao, Z. Shahpar, S. Emaminejad, S. Challa, K. Chen, H. M. Fahad, L. C. Tai, H. Ota, R. W. Davis and A. Javey, ACS Nano, 2016, 10, 7216–7224.

209   J. Liu, W. Lu, L. Zhang, J. Yang, Z.-P. Yao, Y. He and Y. Li, Biosens Bioelectron, 2021, 193, 113534.

210   J. J. García-Guzmán, C. Pérez-Ràfols, M. Cuartero and G. A. Crespo, Trends in Analytical Chemistry, 2021, 135, 116148.

211   H. Lu, S. Zada, L. Yang and H. Dong, Front Bioeng Biotechnol, 2022, 10, 1–17.

212   B. L. Zhang, X. P. Zhang, B. Z. Chen, W. M. Fei, Y. Cui and X. D. Guo, Microchemical Journal, 2021, 162, 105830.

213   J. J. García-Guzmán, C. Pérez-Ràfols, M. Cuartero and G. A. Crespo, ACS Sens, 2021,

6, 1129–1137.

214   C. Hegarty, A. McConville, R. J. McGlynn, D. Mariotti and J. Davis, Mater Chem Phys, 2019, 227, 340–346.

215   J. X. Zhou, F. Ding, L. N. Tang, T. Li, Y. H. Li, Y. J. Zhang, H. Y. Gong, Y. T. Li and G. J. Zhang, Analyst, 2018, 143, 4469–4475.

216   G. K. Mani, K. Miyakoda, A. Saito, Y. Yasoda, K. Kajiwara, M. Kimura and K. Tsuchiya, ACS Appl Mater Interfaces, 2017, 9, 21651–21659.

217   L. A. Beardslee, G. E. Banis, S. Chu, S. Liu, A. A. Chapin, J. M. Stine, P. J. Pasricha and R. Ghodssi, ACS Sens, 2020, 5, 891–910.

218   K. Kalantar-Zadeh, N. Ha, J. Z. Ou and K. J. Berean, ACS Sens, 2017, 2, 468–483.

219   S. Mukherjee, S. Suleman, R. Pilloton, J. Narang and K. Rani, Sensors, 2022, 22, 4228.

220   M. A. Kwiatek and J. E. Pandolfino, Digestive and Liver Disease, 2008, 40, 156–160.

221   R. H. Hunt, Arch Intern Med, 1999, 159, 649–657.

222   C. Cheng, Y. Wu, X. Li, Z. An, Y. Lu, F. Zhang, B. Su and Q. Liu, Sens Actuators B Chem, 2021, 349, 130781.

223   B. Kuo, M. Maneerattanaporn, A. A. Lee, J. R. Baker, S. M. Wiener, W. D. Chey, G. E. Wilding and W. L. Hasler, Dig Dis Sci, 2011, 56, 2928–2938.

224   S. S. C. Rao, B. Kuo, R. W. McCallum, W. D. Chey, J. K. DiBaise, W. L. Hasler, K. L. Koch, J. M. Lackner, C. Miller, R. Saad, J. R. Semler, M. D. Sitrin, G. E. Wilding and H. P. Parkman, Clinical Gastroenterology and Hepatology, 2009, 7, 537–544.

225   W. Weitschies, L. Müller, M. Grimm and M. Koziolek, Adv Drug Deliv Rev, 2021, 176, 113853.

226   K. M. Herdman, C. B. Breslin and N. J. Finnerty, Electrochim Acta, 2019, 298, 484–495.

Chapter 2. EXPERIMENTAL

This chapter details the chemicals, materials, and instrumentation used throughout this thesis. More specific experimental information is provided within each chapter.

2.1. CHEMICALS

All solutions were prepared using ultra-pure water with a resistivity of ≥ 18.2 MΩ cm at 25°C (Millipore, Watford, UK). Chemicals were used as received, and weighed using an analytical balance (A200S, Sartorius, Göttingen, Germany). A summary of the chemicals used can be found in Table 2.1. Solution pH values were measured using a commercial glass pH probe (SevenGo pro, Mettler Toledo).

Table 2.1.   List of chemicals used with details of suppliers.

Chemical	Supplier	Details
Anhydrous potassium carbonate K_2CO_3	Fisher Scientific	Extra pure
Argon gas	BOC	Pureshield, 99.998%
Boric acid H_3BO_3	Scientific Lab Supplies	> 99.0%
Bovine serum albumin	Sigma Life Science	Lyophilised powder ≥ 96.0%
Calcium chloride dihydrate $CaCl_2$	Sigma Aldrich	≥ 99.0%
Citric acid monohydrate $C_6H_8O_7$	Sigma Aldrich	≥ 99.5%
Glucose $C_6H_{12}O_6$	Sigma Aldrich	≥ 99.5%

4-(2-hydroxyethyl)-1-piperazineethanesulfonic acid (HEPES)	Sigma Aldrich	≥ 99.5%
Hexaammineruthenium (III) chloride $[Ru^{(III)} (NH_3)_6^{3+}]Cl_3$	Strem Chemicals	99.0%
Hydrogen peroxide H_2O_2	Sigma Aldrich	30% w/w
Iridium tetrachloride $IrCl_4$	Alfa Aesar	99.8%
Magnesium sulfate, anhydrous $MgSO_4$	Sigma Aldrich	≥ 99.5%
Mucin from porcine stomach	Sigma Life Science	Type II
Oxalic acid dihydrate $C_2H_2O_4$	Sigma Aldrich	≥ 99.0%
Potassium chloride KCl	Acros Organics	Extra pure
Potassium hexachloroiridate (IV) $K_2 [Ir^{(IV)} Cl_6]^{2-}$	Sigma Aldrich	99.99 % trace metals basis
Potassium nitrate KNO_3	Acros Organics	99+%, for analysis
Sheep's blood in Alsever's	TCS Bioscience	
Silicon tubing	RS Components	3.2 mm bore diameter
Silver nitrate $AgNO_3$	Sigma Aldrich	99.99 % trace metals basis
Sodium chloride $NaCl$	Sigma Aldrich	For analysis
Sodium hydroxide $NaOH$	Sigma Aldrich	> 99.99%
Sulphuric acid	Fisher Scientific	≥ 95.0%

H_2SO_4		
Tertiary sodium phosphate Na_3PO_4	Acros Organics	≥ 99.0%

2.2. MATERIALS

Materials used for sensor fabrication and experimental set up in this thesis are summarised in Table 2.2.

Table 2.2.   List of materials used with details of suppliers.

Materials	Supplier	Details
3D printer Resin	FormLabs	Formlabs Clear Resin
Alumina polish	Buehler	ø= 0.05 µm particles
Boron doped diamond	Element Six	Electroanalytical grade
CarbiMet (silicon carbide) paper	Buehler	P120, P180, P240, P1000
Conductive adhesive, Ag epoxy	Chemtronics, Circuitworks	-
Copper wire	R.S. Components	-
Epoxy Resin	Araldite	5-minute epoxy
Glass capillaries	Harvard Apparatus Ltd.	O.D. 2 mm, I.D. 1.16 mm
Glassy Carbon electrode	CH Instruments, IJ Cambria	ø = 3 mm
Hamilton glass syringes	-	100 mL
Leak-free silver-silver chloride electrode	Alvatek	LF 1-45
Polishing pads	Buehler	MicroCloth PSA
Pt wire	Goodfellows	-

Saturated calomel electrode	CH Instruments, IJ Cambria	-
Syringe pump	KD Scientific	Dual syringe

2.3. ELECTRODE FABRICATION

2.3.1. Preparation of BDD

All work in this thesis was undertaken using cylinders of polycrystalline BDD with a 1 mm diameter (boron dopant density $>10^{20}$ B atoms cm^{-3}, minimal sp^2-carbon content,[1,2] Element Six) laser machined from a 6 inch freestanding polycrystalline BDD wafer using a 355 nm Nd:YAG 34 ns laser micromachine (E-355H-ATHI-O system, Oxford Lasers). The BDD wafer had a thickness of 357 μm and was polished to ~nm roughness on the growth (front) face and lapped on the nucleation (rear) face.

2.3.2. Oxidative acid treatment and thermal anneal procedure

After laser micro-machining, all BDD samples underwent an oxidative acid treatment to remove loosely bound sp^2 and oxygen-terminate the BDD surface. Samples were heated at ~200°C for 30 min in a solution containing 0.75 g of KNO_3 per mL of concentrated H_2SO_4. The samples were removed and rinsed before placing in concentrated H_2SO_4 and heated for an additional 30 min.[3] Once cooled, samples were thoroughly rinsed with ultrapure water and left to air dry on lint-free cloth. To remove any further sp^2 carbon, particularly from the laser machined edge regions a thermal anneal at 600°C in air for 5 h was performed with the polished face against the supporting quartz slide to exclude oxygen to prevent etching of the polished face.

2.3.3. Incorporation of pH sensitive BDD-Q and sp^2-BDD

For pH sensing applications such as those discussed in Chapter 3 and 5, and preparation of sp^2-BDD in Chapter 4, a further laser micro-machining process is undertaken prior to the addition of an electrical contact, to produce patterned regions of sp^2 carbon into the BDD surface.[4,5] The sp^2 carbon features were produced by rastering the laser beam in a circular pattern with a nominal

pulse density of 1×10^6 pulses per cm^2 with a pulse fluence of 14 J cm^{-2}.[6] Followed by the same oxidative acid procedure as described in section 2.4.2. The patterned BDD samples do not undergo an additional thermal anneal after patterning, as the desire is to utilise the properties of the laser induced sp^2 carbon.

2.3.4. Formation of an Ohmic contact to BDD

For all electrochemical experiments an ohmic contact was prepared on the rear face of the BDD. Layers of Ti (10 nm)/Au (400 nm) were sputtered (Moorfields MiniLab 060 platform sputter/evaporator) onto the back (lapped, nucleation face) of the BDD samples under vacuum ($< 10^{-5}$ mbar) and the samples were subsequently annealed in air at 400°C for 5 h, to allow the Ti to react with the BDD to form titanium carbide (TiC), which helps to lower the potential barrier from the BDD to the metal contact,[7] creating a reliable Ohmic contact.

2.3.5. Electrode manufacture

2.3.5.1. Glass sealed electrodes

To produce useable electrodes, the prepared BDD cylinders were placed into heat-pulled (Narishiage PB-7) borosilicate glass capillaries with the Ti/Au sputtered side facing the open capillary end. A vacuum was then applied and the BDD cylinders were heat sealed within the capillaries, melting the glass around the front and side faces of the BDD to seal the sides of the electrode. An external electrical contact was established by filling the glass capillary with conductive silver epoxy and inserting a copper wire until pressed against the Ti/Au sputter contact.

The BDD electrode surface was then exposed by polishing away the glass from the tip using carbimet abrasive paper, incrementally moving from grit sizes P120, P180, and P240, then finally exposing the BDD round out of the surrounding glass with a P1000 carbimet paper. Note, care must be taken to ensure that the glass capillary is held perpendicular to the abrasive disks, failure to do so results in the exposure of the laser ablated edges of the BDD cylinders and a poorly defined electrode surface. The electrodes were imaged (Olympus BH-2-HLSH) to check that all glass remnants had been removed from the

electrode surface, exposing the full electrode area. White light interferometry was used to measure the area of the electrodes (section 2.5.3).

2.3.5.2. All Diamond electrodes

An alternative method to the glass casing, is to fabricate all-diamond devices consisting of BDD electrodes encased in an insulating diamond during the growth process (Figure 2.1),[8] which can be sealed in a tougher polymer-based casing than the glass capillary. Directly growing BDD into the intrinsic diamond provides the best seal between the two materials than with other electrode sealing materials. These electrodes are fabricated by laser micromachining into an insulating diamond substrate, then overgrowing a layer of BDD. This layer of BDD is then polished back to expose the coplanar all-diamond electrode.[8]
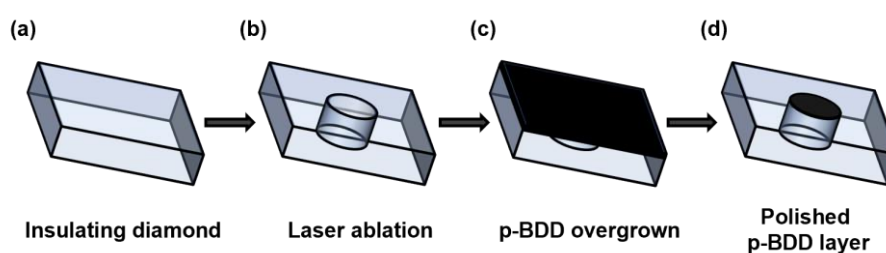
Figure 2.1. Schematic for all-diamond electrode manufacturing process, (a) the growth of insulating diamond, (b) the laser micromachining of the insulating diamond in the pattern of the electrode required, (c) a layer of BDD overgrown, and (d) the subsequent polish back to reveal BDD electrode coplanar with the surrounding insulating diamond.[8]

2.3.6. Iridium oxide pH sensor fabrication

The iridium oxide (IrOx) solution was prepared as described in literature.[9-11] 4.45 mM iridium tetrachloride, 1 mL hydrogen peroxide (H_2O_2, 30% w/w), and 39 mM oxalic acid dihydrate were added sequentially to 100 mL of water and stirred for 30-, 10-, and 10-min intervals, respectively. Anhydrous potassium carbonate was added until a pH of 10.5 was achieved, resulting in a pale yellow-green solution. This was stirred for 48 h until the solution had

stabilised, and the appearance changed to a blue-purple colour. The IrOx solution was stored refrigerated and bought to ambient temperature before use. Anodic deposition of an IrOx onto a BDD electrode (1 mm diameter) was performed in the IrO_x deposition solution using a chronoamperometric method, where the potential was pulsed for 100 × 0.2 s steps between 0 V and +0.8 V versus a saturated calomel electrode (SCE). The film quality was assessed via CVs conducted at 1 mV s^{-1} between 0 V to 1 V vs SCE in 0.1 M H_2SO_4 and considered successful where a peak current of ~4 μA (51 μAcm^{-2}) was observed. The pH response is reliant on the hydration of the film and a difference in storage and measurement matrix can affect equilibration times,[12–14] therefore, the resulting film was hydrated in pH 7 buffer solution 2 days prior to use and stored in this buffer solution when not in use.

2.4. INSTRUMENTATION

2.4.1. Potentiostats

Three potentiostats were used throughout this thesis,

Table 2.3.   Potentiostats used in each chapter

Chapter	Potentiostats
3. *Ex vivo* Electrochemical pH Mapping of the Gastrointestinal Tract in the Absence and Presence of Pharmacological Agents	CHI-760 E, CH Instruments Autolab PGSTAT128N, Metrohm
4. Characterising the Impact of Biological Fouling on Carbon Electrodes using Electrochemical Techniques	Ivium Compactstat, Alvatek (Ivium Technologies)
5. Assessing boron doped diamond electrodes under flow for biomedical applications	Autolab PGSTAT128 N, Metrohm

2.4.2. 3D Printing

The components of the flow cell developed and applied in Chapter 5 were 3D printed using a Form 3 printer (Formlabs, Massachusetts, USA). A computer-aided design (CAD) software, Fusion 360 (Autodesk, USA) is used to design the objects to be printed. The Form 3 is a stereolithographic (SLA) 3D printer. SLA printers use a photosensitive thermoset polymer resin, set by an ultraviolet (UV) laser beam,[15] Figure 2.2.

In SLA 3D printer, a UV laser and galvanometers are used to guide the laser beam, allowing it to build the CAD model layer-by-layer in the photopolymer resin. Once the model has been completed it requires postprocessing, which involves the removal of uncured resin through by washing with isopropyl alcohol (IPA) before a final UV cure to ensure the photopolymer achieves its full material properties. All Formlabs resins are polymethylmethacrylate (PMMA) based with a 405 nm photo-initiator, although the exact chemical composition varies. SLA is ideal for printing devices with small features, and those that are required to be water-tight, such as the flow cells used in Chapter 5.
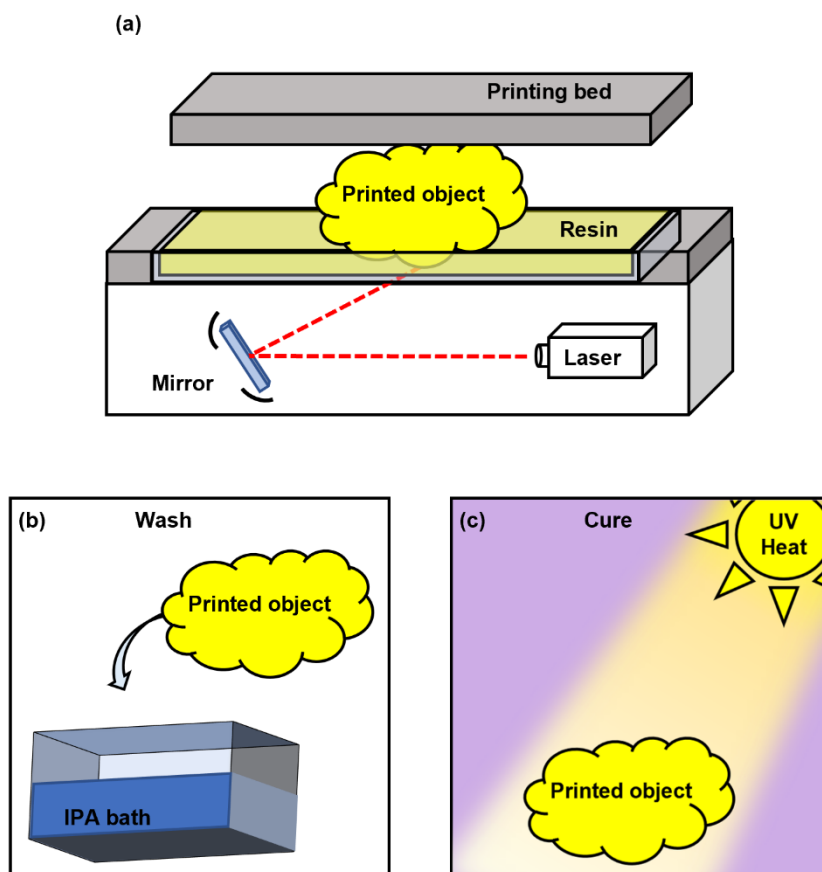
Figure 2.2. (a)Schematic of an SLA 3D Printer, once the desired object is printed, it is (b) washed in an IPA bath, and (c) cured using UV laser beam.

2.4.3. White Light Interferometry

White light interferometry (WLH) is used to measure the topography of a surface through optical interference. A broad-spectrum light source is used that is collimated using a condenser lens. The light is split into two beams, one reflected from a reference mirror and the other scattered by the sample. The reflected beams are relayed to a charge coupled detector, forming an interference pattern.[16] From this, topographical information from the sample can be determined with sub-nm resolution. A Bruker Contour GT (Burker, USA) was used to determine surface area of BDD-Q electrodes used in this thesis.

2.5. ELECTROCHEMICAL CHARACTERISATION

To ensure the BDD was sufficiently doped, and the electrode has a sufficiently Ohmic electrical contact a series of electrochemical characterisation measurements were undertaken.

2.5.1. Capacitance

The working electrode was polished using an alumina slurry on a soft polishing pad followed by an alumina-free damp polishing pad to ensure a clean electrode surface, rinsed, and placed in a 0.1 M KNO_3 solution. In a three-electrode set up, utilising an SCE reference and Pt wire counter electrodes, a cyclic voltammogram was recorded between -0.1 V and 0.1 V starting at 0 V at 0.1 V/s until a stable response was observed to measure the capacitance of the electrode. The final CV was analysed using 63 Equation 2.1.

$$C_{dl} = \frac{i_{av}}{vA}$$
Equation 2.1

Where C_{dl} is the capacitance of the double layer ($\mu F/cm^2$), i_{av} is the average current (A) of the anodic and cathodic current at 0 V, v is the scan rate (V/s) and A is the electrode area (cm^2). High quality BDD is expected to have a capacitance value of $< 10 \mu F/cm^2$.[17]

2.5.2. Solvent window

A solvent window is the potential range within which an electrode material could be used for analytical measurements before solvent oxidation and reduction dominate the current response. A CV is recorded across a large potential range from a starting point where no reactions are expected to occur, sweeping the potential from at 0 V to -2 V and then between -2 V and +2 V repeatedly (3 cycles). The current of the second CV was converted to current density (mA/cm^2) and the solvent window is defined as the potential range in which a current of no more than ±0.4 mA/cm (based on the region where solvent reactions occur).[2,17] For high quality BDD the solvent window is expected to exceed 3 V, any incorporated sp^2 material will reduce this range as it facilitates inner sphere reactions such as oxygen reduction and can itself be oxidised.[17]

2.5.3. Redox electrochemistry

A well-defined redox mediator, in this case ruthenium hexamine ($Ru(NH_3)_6^{3+}$), is used to probe the material and quality of contact. This particular mediator on BDD is advantageous as it shows fast electron transfer (> mass transport) and is electroactive in a region challenging for p-doped semiconducting BDD making it a good probe of the material quality.[17] A CV is recorded between +0.2 V and -0.6 V in 1 mM $Ru(NH_3)_6^{3+}$ with 0.1 M KNO_3, the potential separation (ΔE_p) between the cathodic and anodic peaks at 0.1 V/s can be compared to theory; a value < 70 mV is expected for a well doped BDD electrode with a good ohmic contact under standard conditions, although the theoretical value for a macroelectrode is 57 mV, the size of the BDD electrodes used means that some contribution of hemispherical diffusion from the edges is also expected which will increase this value.[18] Additionally, for a given scan rate and concentration of analyte, the peak current can be predicted according to the Randles-Sevcik equation, Equation 2.2,

$$i_p = 0.4463nFAC \left(\frac{nFvD}{RT}\right)^{\frac{1}{2}}$$

Equation 2.2

where, n is the number of electrons transferred, F is the Faraday's constant, A is the area of the electrode (cm^2), C is the concentration of the redox species ($molcm^{-3}$), v is the scan rate (V), D is the diffusion coefficient of the redox couple, R is the ideal gas constant, and T is the temperature (K).

2.5.4. Quinone surface coverage measurement

For electrodes with deliberate sp^2 carbon incorporation measurement of the relative amount of sp^2 carbon can be useful to compare electrode behaviours. An indirect measure using quinone electrochemistry can be used to infer the sp^2 carbon content.[5] A CV is conducted in 0.1 M H_2SO_4 at 0.1 V/s between 0 V to -2 V, then to +2 V, and back to 0 V for 20 cycles in a three electrode set up. Quinone surface coverage analysis was undertaken in a pH 2 Carmody buffer using CV between 0 and 0.7 V *vs*. SCE at 0.1 V/s. The peak between 0.25 and 0.6 V is baselined with a straight line and integrated to give the area under the peak (A_p). The quinone surface coverage (Γ) is calculated by,

$$\Gamma = \frac{A_p}{nAFv} \qquad\qquad \text{Equation 2.3}$$

Where n is the number of electrons transferred, A is the electrode surface area, and F is Faraday constant.

2.6. REFERENCES

1   L. A. et al. Hutton, J. G. Iacobini, E. Bitziou, R. B. Channon, M. E. Newton and J. V Macpherson, *Anal. Chem.*, 2013, **85**, 7230–7240.

2   L. Hutton, M. E. Newton, P. R. Unwin and J. V Macpherson, *Anal. Chem*, 2009, **81**, 1023–1032.

3   S. J. Cobb, F. H. J. Laidlaw, G. West, G. Wood, M. E. Newton, R. Beanland and J. V Macpherson, *Carbon N. Y.*, 2020, **167**, 1–10.

4   Z. J. Ayres, A. J. Borrill, J. C. Newland, M. E. Newton and J. V Macpherson, *Anal. Chem.*, 2016, **88**, 974–980.

5   Z. J. Ayres, S. J. Cobb, M. E. Newton and J. V Macpherson, *Electrochem. commun.*, 2016, **72**, 59–63.

6   T. L. Read, S. J. Cobb and J. V Macpherson, *ACS. Sens.*, 2019, **4**, 756–763.

7   S. A. Manifold, G. Klemencic, E. L. H. Thomas, S. Mandal, H. Bland, S. R. Giblin and O. A. Williams, *Carbon N. Y.*, 2021, **179**, 13–19.

8   M. B. Joseph, E. Bitziou, T. L. Read, L. Meng, N. L. Palmer, T. P. Mollart, M. E. Newton and J. V. MacPherson, *Anal. Chem.*, 2014, **86**, 5238–5244.

9   K. Yamanaka, *Jpn. J. Appl. Phys.*, 1989, **28**, 632–637.

10   K. Yamanaka, *Jpn. J. Appl. Phys.* , 1991, **30**, 1285–1289.

11   T. L. Read, E. Bitziou, M. B. Joseph and J. V Macpherson, *Anal. Chem*, 2014, **86**, 367–371.

12   S. Kakooei, C. Ismail and B. Ari-Wahjoedi, *Int. J. Mater. Sci. Innov.*, 2013, **1**, 62–72.

13   D. O'Hare, K. H. Parker and C. P. Winlove, *Med. Eng. Phys.*, 2006, **28**, 982–988.

14   T. Rajan, T. Read, A. Abdalla, B. Patel and J. Macpherson, *ACS Sensors*, 2020, **5**, 2858–2865.

15   J. J. Tully and G. N. Meloni, *Anal. Chem.*, 2020, **92**, 14853–14860.

16   P. Hariharan, *Basics of Interferometry*, Elsevier, 2007.

17   J. V. Macpherson, *Phys. Chem. Chem. Phys.*, 2015, **17**, 2935–2949.

18   R. S. Nicholson and I. Shain, *Anal. Chem.*, 1964, **36**, 1212.

Chapter 3.   *Ex-vivo* Electrochemical pH Mapping of the Gastrointestinal Tract in the Absence and Presence of Pharmacological Agents

3.1. Introduction

Disturbances in the pH homeostasis of the upper gastrointestinal (GI) tract, leads to many different health issues including gastritis, gastroduodenal ulceration, dyspepsia, and gastroesophageal reflux disease (GERD).[1–3] Under healthy conditions, the pH in the upper GI tract is maintained at ~7 in the oesophagus, dropping to ~2 in the stomach and rising to pH 5-6 in the duodenum (Figure 3.1).[4–6] The low pH in the stomach is due to gastrin-stimulated proton-potassium pumps[7] in oxyntic glands secreting gastric acid.[8] Gastric acid is secreted in response to chemical and mechanical stimulus.[9] In the duodenum, production and secretion of bicarbonate dominates, causing partial neutralisation of acid entering from the stomach and resulting in a pH rise.[10] Alterations in gastric acid production and/or bicarbonate excess or deficiency result in disturbances to the pH homeostasis. Drugs such as omeprazole, treat excess acid production disorders such as GERD by reducing acid production in the stomach, due to their action as a proton pump inhibitor (PPI).[1,11] The hormone, melatonin, has been used effectively in combination with omeprazole for GERD treatment,[12] as it provides gastric mucosal protection by inhibiting acid secretion, whilst stimulating duodenal bicarbonate secretion.[13,14] Detecting pH changes across the GI can offer vital information to aid diagnosis and efficacy of treatments for GI related illnesses.
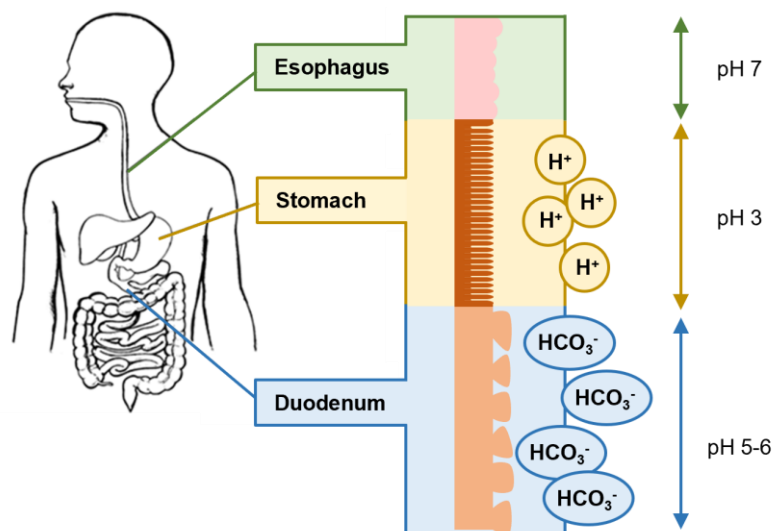
Figure 3.1. Diagram of the human body, with the oesophagus, stomach and duodenum labelled

pH measurements are typically performed using potentiometric glass pH sensors.[15] These electrodes show a Nernstian (-59 mV/pH unit) response and high selectivity towards protons (H$^+$).[15,16] However, the glass membrane is fragile, the sensors can be bulky, the electrodes often require frequent recalibration due to potential drift, and a stable pH response can take minutes, dependent on solution conditions.[17] When miniaturisation of the sensor is required, metal-metal oxide electrodes, in particular iridium oxide (IrOx) films are often used.[17–22] When electrochemically deposited, IrOx films exhibit Nernstian to super-Nernstian responses (-60 to -80 mV/pH unit).[20,23–25] Such electrodes have shown variability in response time ranging from 0.3 s to 190 s;[20,23,26–28] the longer response times are associated with increases in solution alkalinity.[20,23] High concentrations of chloride have been shown to result in film dissolution,[18] suggesting that IrOx films are not suitable for long-term application in chloride-containing systems.

Quinone (Q) functionalised carbon-based electrodes, operated as voltammetric pH sensors, have also attracted interest, as the quinones undergo proton coupled electron transfer (Q + 2H$^+$ + 2e$^-$ → QH$_2$) and thus show a Nernstian voltammetric pH response.[29] The quinones are either directly integrated into the electrode surface, as is the case for sp^2 bonded carbon materials[30–33] and hybrid sp^2-boron doped diamond electrodes (BDD-Q

electrodes),[34] or are tethered chemically to the electrode surface.[35,36] The latter is far more susceptible to degradation if the electrode requires mechanical cleaning. Q-functionalised electrodes perform well under buffered conditions, providing a pH response in the time taken to produce a voltammetric scan (i.e. seconds).[32–34] In unbuffered solutions, the situation is more complicated due to local proton depletion/accumulation during the voltammetric measurement. The use of low Q surface coverages coupled with pulsed voltammetric measurements[37] or Q structures that promote inter and intra-molecular hydrogen bonding,[38,39] have been explored to negate this effect.

There is limited information concerning pH measurements across the upper GI tract; measurements have largely focused on the stomach only, *ex-vivo* and *in-vivo*. For example, IrOx electrodes were used *ex-vivo* to measure the pH of isolated stomach tissue.[40,41] To minimise electrode fouling, measurements were made under flow, however, this comes at a loss of spatial resolution due to flow-induced mixing of local pH gradients. *In-vivo* pH measurements of gastric acid in the stomach were carried out using glass potentiometric electrodes,[42,43] whilst a BDD microelectrode placed in the stomach of a mouse was used to record stomach pH.[44] The latter measured the amperometric signal associated with proton reduction, however, unlike the techniques highlighted above, this method lacks selectivity for protons, any redox species active at the operating potential will be reduced. Although still in their infancy, *in-vivo* pH measurements have been performed using ingestible wireless transmitting capsules (e.g., SmartPill)[45] that record pH, pressure, and temperature during transit.[46,47] The pH component of the SmartPill is an ion-selective field effect transistor. However, such devices suffer from frequent loss of signal, large pH-drift, and difficulty in accurately determining the location of the capsule.[5]

This study aims to map the pH profile of the upper GI tract of a mouse, under first homeostasis and then in response to pharmacological treatment (both omeprazole and melatonin). The measurement is made under diffusion only conditions, to minimise flow induced pH mixing, and the electrode itself is used to mechanically stimulate the tissue in order to induce acid secretion. To determine the most suitable pH technology for this measurement, we first assess the suitability of three different electrochemical approaches, traditional pH

sensitive glass, IrOx electrodeposited on BDD (BDD-IrOx), and BDD-Q in physiologically relevant 0.5% w/v mucin. Mucin, which coats the surface of epithelial organs is a useful mimic for the GI environment,[48–50] and a common electrode fouling agent.[50] The most promising methodology, in terms of robustness, minimal fouling, ability to rapidly measure pH, with a spatial footprint capable of differentiating between different regions of the GI tract, is then applied.

3.2. EXPERIMENTAL

3.2.1. Solutions

Solutions were prepared using ultrapure water (Milli-Q, resistivity $\geq$ 18.2 MΩ cm at 25 °C). All chemicals were used as received. Carmody buffers were prepared over the physiological range pH 3-8 using boric acid (H_3BO_3, 99.97%, Sigma-Aldrich), citric acid monohydrate ($C_6H_8O_7$, $\geq$99.5%, Sigma-Aldrich), and tertiary sodium phosphate (Na_3PO_4, $\geq$95%, Sigma-Aldrich).[52] BDD/BDD-Q electrode characterisations were conducted in 0.1 M KNO_3 (99%, Sigma-Aldrich), 1 mM ($Ru(NH_3)_6^{3+/2+}$ (99%, Strem Chemicals), 0.1 M H_2SO_4 (Fisher Scientific), and pH 2 Carmody buffer. The IrOx deposition solution was prepared from iridium tetrachloride hydrate (99.9%, Alfa Aesar), hydrogen peroxide solution (H_2O_2, 30% w/w, Fisher Scientific), oxalic acid dihydrate (HO_2CCO_2H, $\geq$99%, Sigma Aldrich), and anhydrous potassium carbonate (K_2CO_3, $\geq$99%, Fisher Scientific). Mucin from porcine stomach (Sigma-Aldrich) 0.5% w/v in HEPES buffer solution, pH 7.4 (135.5 mM NaCl, 5.9 KCl, 2.5 mM $CaCl_2$, 1.2 mM $MgSO_4$, 5.0 mM HEPES, 3.5 mM NaOH, 10.0 mM glucose) was prepared and used as a biological mimic of the GI tract environment. pH measurements were made using a Mettler Toledo SevenGo pH portable meter and InLab Expert Go-ISM glass probe (bulb size = 10 mm), kept in the Mettler Toledo InLab storage solution, when not in use. All pH electrodes were calibrated using Carmody buffers of pH 3, 4, 6, 7 and 8. Pharmacological tests were conducted on mouse GI tissue (2 months old, C57BL6) using 10 µM omeprazole ($C_{17}H_{19}N_3O_3S$, Sigma-Aldrich), and 1 µM melatonin ($C_{13}N_{16}N_2O_2$, $\geq$98%, Sigma-Aldrich) in HEPES buffer solution. The

preparation of IrOx solution and the electrodeposition of IrOx film on BDD is described in detail in Chapter 2.

3.2.2. BDD and BDD-Q pH sensor fabrication and characterisation

Polycrystalline BDD cylinders of 1 mm diameter (357 μm thickness; boron dopant density $>10^{20}$ B atoms cm^{-3}; minimal sp^2-carbon content, Element Six), polished on the top (growth) surface to approximately nanometre scale roughness, were machined from a 6-inch freestanding BDD wafer using a 355 nm Nd:YAG 34 ns laser micromachiner (E-355H-ATHI-O system, Oxford Lasers). The BDD cylinders were cleaned by immersing in ~200 °C, concentrated H_2SO_4 (analytical reagent grade ≥ 95 %, Fischer Scientific) saturated with KNO_3 for 30 mins. Samples were then rinsed with ultrapure water and cleaned in concentrated H_2SO_4 at ~200 °C for 30 minutes.[53] The BDD cylinders were annealed at 600 °C in air for 5 hours to remove any sp^2 bonded carbon created during the laser machining process.[53] To provide an Ohmic electric contact, Ti (10 nm) / Au (400 nm) was sputtered (Moorfields MiniLab 060 platform sputter/evaporator) onto the backside of the cylinder and annealed at 400°C for 5 hours. These were then sealed in glass capillaries (O.D. 2 mm; I.D. 1.16 mm, Harvard Apparatus Ltd., Kent, U.K.) using the procedure outlined previously.[54]

For BDD-Q electrodes, the acid-cleaned and annealed BDD cylinders were laser micro-machined to produce a patterned hexagonal array of sixty-one sp^2-bonded carbon containing pits (diameter = 50±2 μm, depth = 5±2 μm, centre-to-centre spacing = 100 μm), following a published procedure.[35] Each pit was composed of a series of concentric rings, machined with a pulse fluence of ~14 J cm^{-2}, with pulses pitched at 1.5 μm, and rings pitched at 3 μm. After laser machining, the electrodes were acid cleaned at ~200 °C for 30 min in concentrated H_2SO_4 saturated with KNO_3, rinsed, followed by a final treatment in concentrated H_2SO_4 at ~200 °C for 30 minutes. This procedure leaves a very robust form of sp^2 bonded carbon, which has withstood the oxidative acid clean, in the laser machined regions of the BDD surface.[53] An Ohmic contact was formed and the BDD-Q sealed in glass, as described above. The electrode surface and pit profiles were analysed *via* white light interferometry (WLI: Contour GT, Bruker).

3.2.3. Electrochemical measurements

Electrochemical measurements (voltammetric or open circuit potential (OCP)) were conducted using a potentiostat (CHI-760E, CH Instruments Inc., USA, or AutoLab PGSTAT128N, Metrohm, UK). For the BDD-Q electrode, measurements were made using a SCE (IJ Cambria Scientific Ltd., UK), or a non-leak silver-silver chloride reference electrode (Ag|AgCl, Alvatek Ltd., UK), and a platinum wire (Goodfellow) counter electrode. Prior to use the electrochemical response and quinone surface coverages associated with the laser micromachined sp^2 bonded carbon regions of the BDD-Q electrode were characterised using standard protocols described previously.[35,55] Given the very low Q surface coverages[38] and to negate any possible proton depletion/accumulation effects, the pH response of the BDD-Q electrode was recorded using square wave voltammetry (SWV) using previously defined parameters: frequency = 150 Hz, amplitude = 100 mV, step potential = 1 mV.[35,38] SWV also offers a reduced scan time over other pulse techniques such as differential pulse voltammetry. The BDD-Q electrode was stored dry when not in us. Between measurements, where necessary, the electrodes were polished first with alumina (0.05 μm, Buehler, Germany) paste on a micro cloth pad (Buehler), and then on a wetted (ultrapure water) alumina-free pad.

For the glass pH probe, as commercial pH meters provide the user with only the final pH reading, to access the OCP-time data, the pH probe was connected to an AutoLab PGSTAT128N potentiostat. The OCP was measured (data point every 0.1 s) against a non-leak Ag|AgCl reference until the change in OCP was ≤ 0.1 mV (corresponding to 0.001 pH units respectively). Once stabilised the OCP was recorded for a further 30 s and the OCP data averaged over this time period, to give the final pH reading. The measurements were conducted in order of decreasing acidity. The glass pH electrode was stored in the Mettler Toledo InLab storage solution when not in use, and was cleaned in accordance with manufacturer guidelines by soaking the electrode in 0.1 M HCl solution.[56] For IrOx, OCP measurements were conducted against a non-leak Ag|AgCl reference, using the CHI-760E and the same protocol adopted for making stable OCP measurements. These measurements were conducted by first decreasing pH and

then increasing, in repeat cycles, obtaining at least three measurements at each pH.

3.2.4. Field Emission Scanning Electron Microscopy

Field-emission scanning electron microscopy (FE-SEM) was used to image the BDD-Q electrode before and after SWV scans in 0.5% w/v mucin in HEPES buffer solution. FE-SEM was performed using a Zeiss Supra 55VP, using an in-lens detector at an acceleration voltage of 5 kV.

3.2.5. Biological preparation

Animal experiments were carried out in compliance with the relevant laws and institution (University of Brighton) guidelines. Experimental procedures were conducted under ARRIVE guidelines.[57] C57BL6 male mice (2 months old) were euthanised using CO_2 gas. The oesophagus, stomach, and duodenum were isolated and placed in HEPES buffer solution (pH 7.4) prior to sample preparation. The tissue was then cut along the middle, lightly stretched, and pinned flat onto a polydimethylsiloxane (PDMS) plate using stainless steel pins (diameter = 50 μm), resulting in final tissue dimensions of ~ 1.5 × 5.5 cm. To keep the tissue viable, the pinned tissue was covered with HEPES buffer solution.

3.2.6. Biological experiments

For *ex-vivo* BDD-Q pH measurements, the tissue sample was positioned in the centre of the PDMS plate, with the electrode mounted on a micromanipulator for reproducible placement on the tissue; counter and reference electrodes were positioned close-by (Figure 3.2).
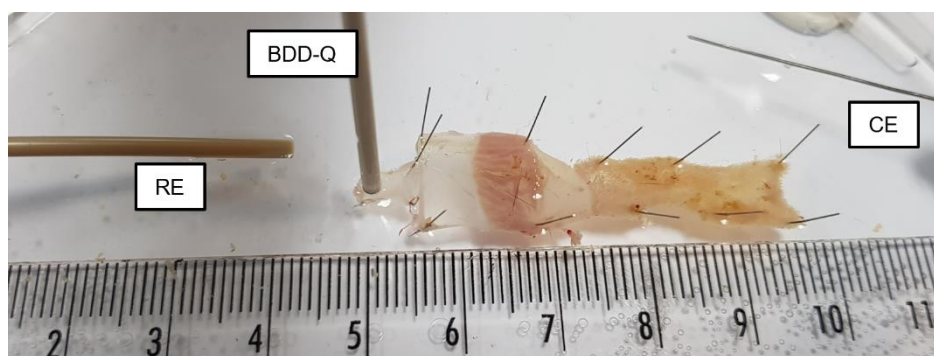
Figure 3.2. Three-electrode set-up used for ex-vivo pH measurement across the upper gastrointestinal tract, indicating the location of the non-leak Ag|AgCl reference electrode (RE), BDD-Q pH electrode, and Pt counter electrode (CE).

For each measurement, the BDD-Q electrode was brought into contact with the tissue (to mechanically stimulate acid production), and then retracted to ~ 0.5 mm using a micro-positioner to maintain a constant separation from the tissue; the tissue surface varied in height, especially in the mid-region of the stomach. After measurement, the electrode was removed, rinsed using ultrapure water, and returned to the tissue. One measurement was made on the oesophagus, five on different regions of the stomach, and four on different regions of the duodenum. Figure 3.3 shows a schematic of the upper GI tract, outlining the areas where the measurements were made. The HEPES buffer was then replaced with omeprazole (10 µM)[58] in HEPES buffer, to assess the influence of the PPI. The tissue was then perfused using HEPES buffer and treated with the hormone melatonin (1 µM),[13] a stimulant for bicarbonate production in the duodenal mucosa, in HEPES buffer. Recordings commenced after 20 mins exposure to the specific treatment.
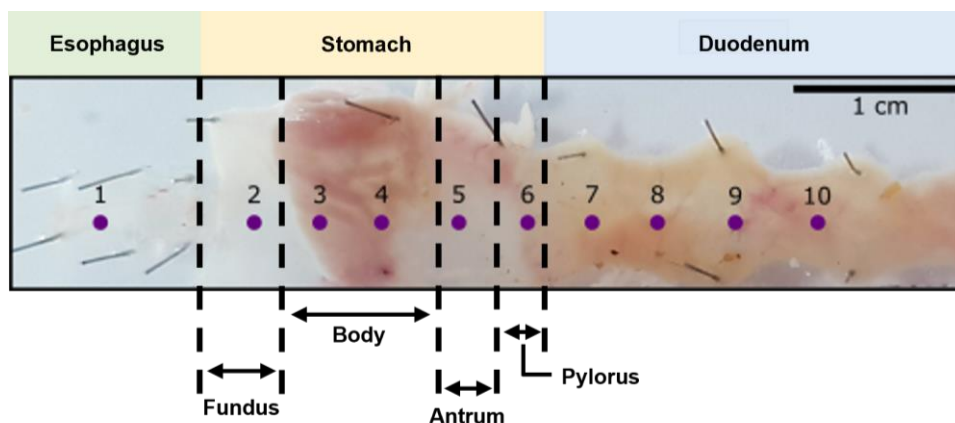
Figure 3.3. Optical image of a mouse GI tract indicating the regions of pH measurement showing (1) oesophagus, (2-6) stomach, and (7-10) duodenum

3.2.7. Data analysis

Data analysis was conducted using OriginPro 9.1 (OriginLab Corp.), Python 3.6 and GraphPad Prism 8. For BDD-Q the SWVs were smoothed using a rolling mean with a window of 10 data points, in order to remove low amplitude noise. The pH peak was identified using the first derivative method within the bounds +0.3 V to -0.2 V *vs* Ag|AgCl. Where the first derivative is equal to zero, a turning point occurs, and the peak minima are identified by a positive second derivative at that point. For each SWV, the peak current and potential values were recorded, and calibration curves were fitted using linear regression. To evaluate statistical differences in the pH of the tissue between treatments, a two-way ANOVA adjusted for Sidak correction was employed, an appropriate correction for multiple comparisons. Differences were considered statistically significant at a probability of $p < 0.05$.

3.3. RESULTS AND DISCUSSION

3.3.1. Potentiometric pH sensing technologies

Figure 3.4 illustrates (i) the mode of action of the pH measurement and (ii) typical OCP-time traces in 0.5% w/v mucin in HEPES buffer, for (a) glass and (b) BDD-IrOx pH electrodes. 0.5% was deemed physiologically relevant based on measurement of mucin concentration extracted from the GI tract of a mouse,

after placement of tissue in 25 mL of oxygenated Krebs buffer for a period of 1 hour. The glass and BDD-IrOx pH electrodes were calibrated by measuring the OCP in Carmody buffers (pH 3-8) before and after measurement in mucin. Between measurements the electrodes were gently rinsed with ultrapure water.
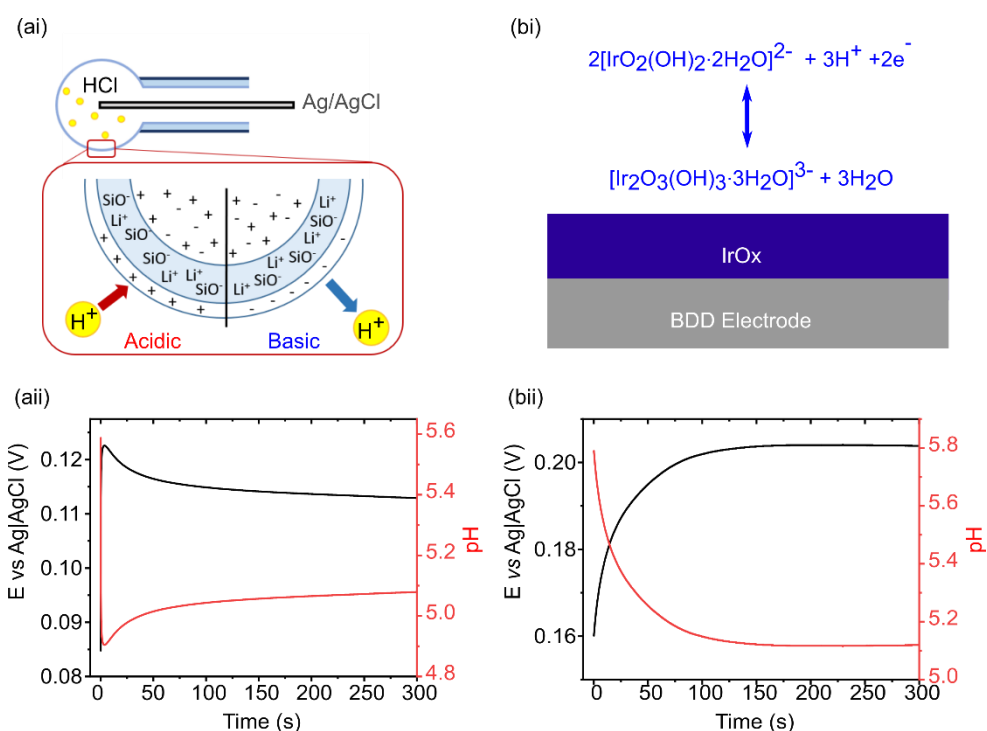
Figure 3.4.   Schematic of the potentiometric pH sensors (ai) glass pH electrode, and (bi) BDD-IrOx pH electrode (this electrode can operate potentiometrically or voltammetrically, we use the potentiometric mode in this investigation). Open circuit potential measurements were conducted in 0.5% w/v mucin in HEPES solutions using (aii) glass pH electrode, and (bii) BDD-IrOx pH electrode.

The data in Figure 3.5 shows the pre- and post-calibrations using a glass pH electrode after conducting pH measurements in 0.5% w/v mucin in HEPES solution (for ≤ 1 mV and ≤ 0.1 mV). After every post-calibration, the glass pH electrode was cleaned by soaking in 0.1 M HCl solution in according with manufacturer guidelines.[58] This procedure was performed three times.
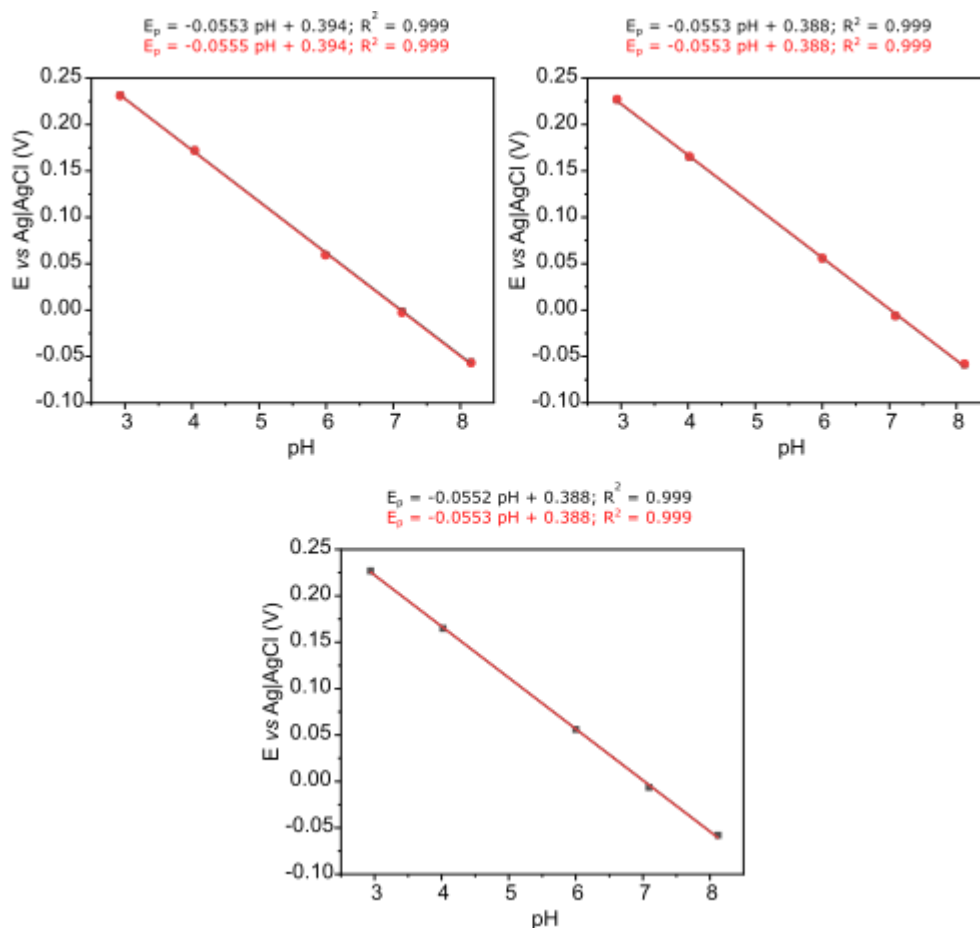
Figure 3.5. Before (black-square) and after (red-circle) measurement in 0.5% w/v mucin-HEPES buffer solution calibration (n=3) for glass pH electrode.

Similarly, the BDD-IrOx electrode was calibrated and placed in 0.5% mucin solution, to make a stable pH measurement (for ≤ 1 mV and ≤ 0.1 mV), then rinsed and re-calibrated (Figure 3.6). After every re-calibration, the electrode was polished in alumina slurry, and a fresh IrOx film deposited onto the BDD electrode. This process was performed three times.

Iridium oxide pH electrode

$E_p = -0.0727$ pH $+ 0.739$; $R^2 = 0.999$ $E_p = -0.0671$ pH $+ 0.594$; $R^2 = 0.999$
$E_p = -0.0721$ pH $+ 0.727$; $R^2 = 0.999$ $E_p = -0.0669$ pH $+ 0.595$; $R^2 = 0.999$
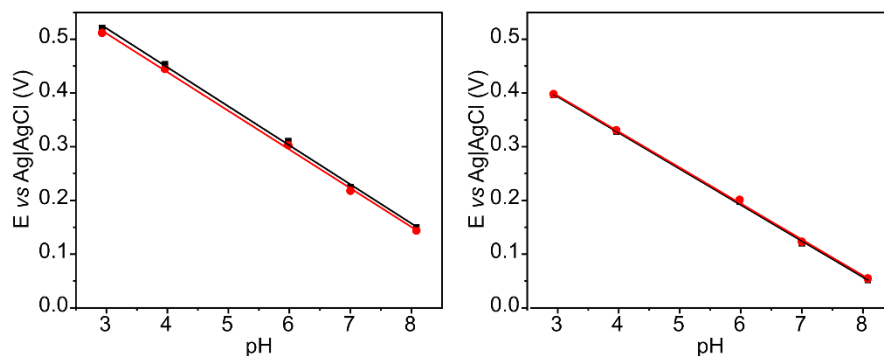
$E_p = -0.0652$ pH $+ 0.539$; $R^2 = 0.999$
$E_p = -0.0657$ pH $+ 0.550$; $R^2 = 0.998$
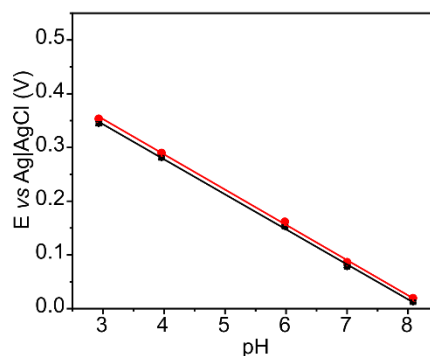
Figure 3.6. Before (black-square) and after (red-circle) measurement in 0.5% w/v mucin-HEPES buffer solution calibration (n=3) for the BDD-IrOx pH electrode

For both electrodes, the calibrations pre- and post-placement in the mucin solution showed minimal difference in gradient and intercept (Figure 3.5 and Figure 3.6). Using the pre-mucin placement calibration data, the OCPs were converted to pH values as shown in Figure 3.4 aii and bii. Note, whilst for the same IrOx electrode, the calibration gradient is unaffected by placement in 0.5% mucin, for each freshly prepared IrOx electrode, different calibration gradients were recorded (Figure 3.6) with a maximum gradient observed of 73 mV/pH, and minimum of 65 mV/pH. This could be due to the variation in Ir^{3+}/Ir^{4+} ratio, or the hydration level of the film.[18,59] The fact that the ratio or hydration level of the film cannot be precisely controlled means the electrode cannot be reproduced exactly each time.

OCP measurements in 0.5% mucin HEPES solution were performed until the change in response is ≤ 0.1 mV. From the data collected two pH values were determined one at ≤ 1 mV and the other ≤ 0.1 mV, which correspond to 0.01 and 0.001 pH units respectively, reflective of the stability criteria available on a commercial pH meter. The average time required for the glass electrode to obtain a stable pH response in the mucin solution was 150 ± 60 s (≤ 1 mV) and 750 ± 60 s (≤ 0.1 mV), n = 3 (same electrode). For comparison, in mucin-free media (Carmody buffer pH 4) the response time was measured as 65 ± 17 s (≤ 1 mV) and 165 ± 60 s (≤ 0.1 mV), n = 3. Figure 3.4 aii displays the first 300 s where the largest changes are evident., Figure 3.7, shows 800 s of OCP data collection for both electrodes while in 0.5% mucin.
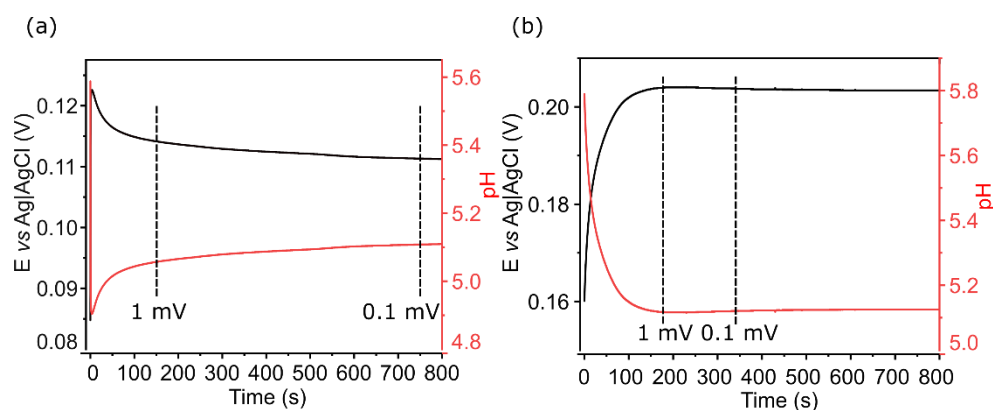
Figure 3.7. OCP measurements conducted in 0.5% w/v mucin in HEPES solution using (a) glass pH electrode and (b) IrOx pH electrode, with 1 mV and 0.1 mV thresholds (indicated by dashed vertical black lines).

The pH of mucin measured with the glass pH probe, assuming ≤ 1 mV accuracy was 5.10 ± 0.04 (n =3) and 5.123 ± 0.013 (n=3) for ≤ 0.1 mV. A separate measurement in the same mucin solution using the Mettler Toledo pH meter gave a pH of 5.020 ± 0.106 (automatic endpoint determination setting was set to 0.001 pH unit accuracy), n = 3 (same electrode and meter).

In Figure 3.4 bii, the OCP-time profile is also shown for the IrOx electrode in 0.5% w/v mucin HEPES solution, over 300 s. Here the electrode can be seen to reach a stable pH of 5.19 ± 0.08 (≤ 1 mV) and 5.20 ± 0.08 (≤ 0.1 mV) in 190 ± 35 s and 330 ± 104 s respectively, (n = 3, three different electrodes). In mucin-free

78

media (Carmody buffer pH 4) the response time was measured as < 1 s (for both ≤ 1 mV and ≤ 0.1 mV). For the glass and IrOx electrodes the decreased times to reach a stable reading in the Carmody buffer suggests that mucin presence is significantly affecting stabilisation times, possibly due to time-dependent adsorption effects.

The longer the stabilisation time the less responsive the pH electrode is to dynamic pH changes. For both electrodes fairly lengthy stabilisation timescales are required leading to greater diffusional mixing between local pH gradients on the GI tissue. Moreover, given the mouse GI tract dimensions, Figure 3.3 to map areas of interest, ten pH measurements every few mm along the length of the tract, are required. The size of the glass pH bulb diameter used (ca. 10 mm) poses a spatial problem for this application. Whilst it is possible to obtain pH-sensitive glass probes with smaller diameters (commercially 8-12 μm probes are available),[60] reduced size comes with significantly increased fragility. An essential part of this experiment is mechanical stimulation of the tissue, in the vicinity of the measurement, by the probe itself; the use of fragile micro-glass pH electrode would prove challenging. Contact of the probe with the tissue, for stimulation, is also problematic for the IrOx-coated electrode, which whilst of an appropriate size (1 mm diameter), is likely to suffer from the film being compromised upon mechanical impact with the tissue.

3.3.2. Voltammetric pH sensing technology

Figure 3.8a show a WLI of a BDD-Q pH sensor, illustrating the position of the sixty-one laser-ablated pits in the BDD electrode surface. Figure 3.8b (inset) shows ten consecutive SWV scans at the BDD-Q electrode (0.6 to -0.3 V, frequency: 150 Hz, amplitude: 0.1 V, increment: 1 mV) recorded in 0.5% w/v mucin in HEPES solution. The time taken for one SWV scan is only 6 s and is an advantage of the voltammetric approach over the OCP timescales for both the glass and BDD-IrOx pH electrodes. Prior to measurement in mucin, the BDD-Q electrode was calibrated in pH 3-8 Carmody buffers (n = 6 per buffer).
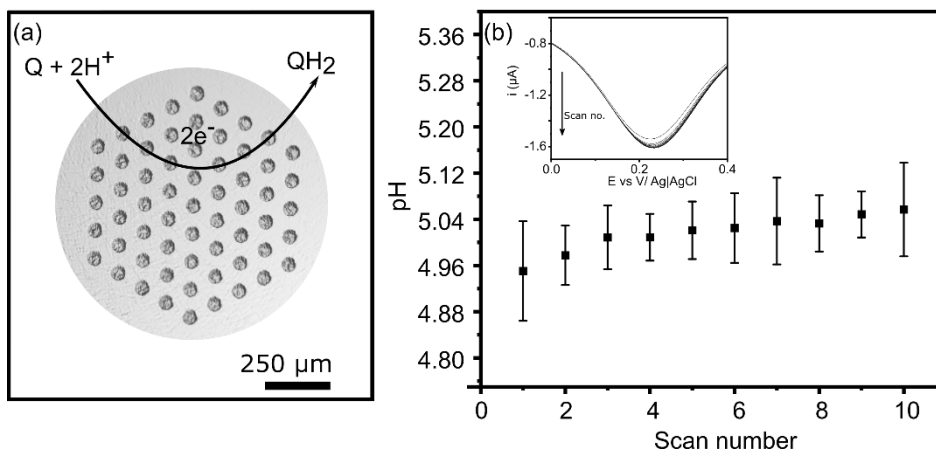
Figure 3.8. (a) White light interferometry image of a BDD-Q pH electrode with the redox reaction responsible for the pH response, (b) average pH against scan number, for ten consecutive SWV scans conducted in 0.5% w/v mucin in HEPES solution, with standard deviation error bars n = 4; inset shows the ten SWV scans in mucin for pH determination.

After recording the ten SWV scans (measurement time = 60 s), the BDD-Q electrode was gently rinsed and recalibrated. This procedure was repeated using the same electrode and two other BDD-Q electrodes (i.e., *n* = 4 in total); calibrations shown in Figure 3.9. The pre- and post-calibrations, for each electrode, are very similar in gradient and intercept. The pre-mucin calibration was used to convert peak potential to pH. Figure 3.9a and b were collected using the same BDD-Q electrode, where after post-calibration of (a), the electrode was polished using an alumina slurry, and calibrated for the repeat (b).
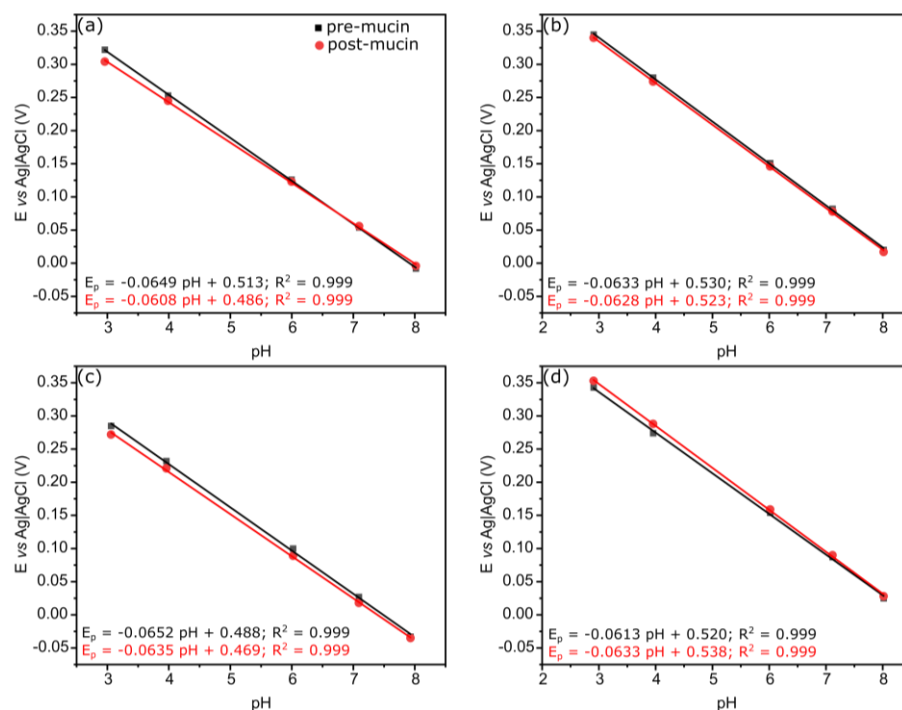
Figure 3.9. Before (black – square) and after (red – circle) measurement in 0.5% w/v mucin-HEPES buffer solution calibration (n = 4) for BDD-Q pH electrode.

FE-SEM images of the BDD-Q electrode surface after (a) polishing using alumina and rinsing with ultrapure water and (b) after ten consecutive SWV scans, removal from the 0.5% mucin – HEPES solution and gently rinsing the electrode with water, are shown in Figure 3.10. In Figure 3.10a, the BDD grains (light and dark regions) are clearly visible, representing low and higher boron doped regions of the polished surface,[61] with three recessed laser-machined pits evident, which contain the sp^2 bonded carbon regions. After placement in mucin, running ten consecutive SWV scans and gently rinsing (Figure 3.10b), interestingly, whilst the image appears very similar, there is now little contrast, even though the imaging conditions were the same. This may suggest some mucin remaining on the surface even after the rinse process but is not conclusive. However, even if present, there is clearly not enough mucin to impact deleteriously on the calibration data, Figure 3.9.
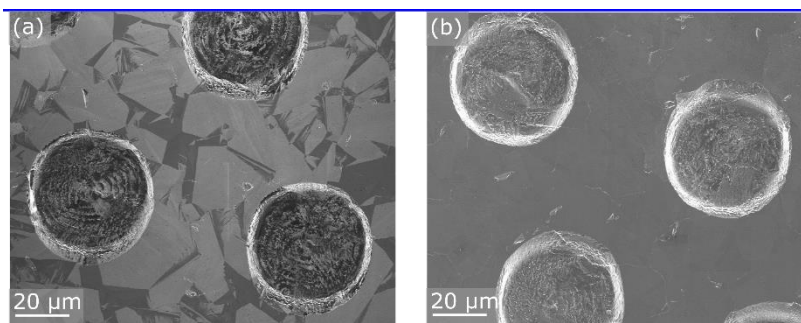
Figure 3.10. FE-SEM images of BDD-Q pH electrode (a) polished with alumina slurry and rinsed, (b) after ten consecutive SWV measurements in 0.5% w/v mucin in HEPES buffer solution and rinsing.

In the mucin-HEPES solution, taking the first scan data, Figure 3.8b, a pH value of 4.950 ± 0.09 was recorded. In comparison the Mettler Toledo pH meter recorded a value of 4.968 ± 0.13 (n = 4, same pH probe and meter). The error is slightly lower for the BDD-Q electrode than the glass pH probe. Considering the repeat scans, if errors are ignored and the average pH per scan number (black square data in Figure 3.8b) is compared, the data does show a very small decrease in peak potential (from 0.197 V to 0.190 V), equivalent to a pH increase from 4.951 to 5.057. The origin of this very small deviation in pH with repeat scans is investigated further in Chapters 4 and 5. Mucin time-dependent adsorption[62] may be one possibility (Chapter 4).

3.3.3. BDD-Q ex-vivo experiments

From an assessment of all three electrodes in terms of time required to record one pH value, the size and robustness of the electrode, and minimal shifts in the pre- and post-mucin calibrations, the BDD-Q electrode was deemed the most appropriate for GI tract pH mapping (Figure 3.3). Ten measurements were typically performed across the GI tissue sample, to include the oesophagus (1), stomach (2-6) and duodenum (7-10).

It was first necessary to validate that the pre-calibration of the BDD-Q electrode was not compromised by contact with the GI tract tissue. In order to assess the electrode performance, nine measurements were performed across the GI tract (measurement 10 in Figure 3.3, was omitted due to tissue size), using

three BDD-Q electrodes. Given the large variation in pH across the GI tract, whilst the very small change in pH arising from repetitive scans (Figure 3.8b) could be accommodated, a short rinse step (~ 10 s) was included between each measurement. This was a precaution to remove any possible mucin (or other species) adsorption exacerbated from contact with the tissue, during mechanical stimulation and was adopted in all GI tract measurements. Even with this rinse step the timescale for BDD-Q measurements is still faster than that possible with glass pH and IrOx electrodes based on the 0.5% mucin data in Figure 3.4aii and bii. Importantly, calibration of the electrode pre- and post-tissue pH measurement showed minimal difference for all three BDD-Q electrodes (Figure 3.11) indicating the electrodes had not been compromised through contact with the tissue.

BDD-Q oxide pH electrode

$E_p = -0.0688$ pH $+ 0.580$; $R^2 = 0.999$
$E_p = -0.0668$ pH $+ 0.560$; $R^2 = 0.999$

$E_p = -0.0673$ pH $+ 0.565$; $R^2 = 0.999$
$E_p = -0.0660$ pH $+ 0.546$; $R^2 = 0.999$

$E_p = -0.0674$ pH $+ 0.575$; $R^2 = 0.999$
$E_p = -0.0663$ pH $+ 0.557$; $R^2 = 0.999$
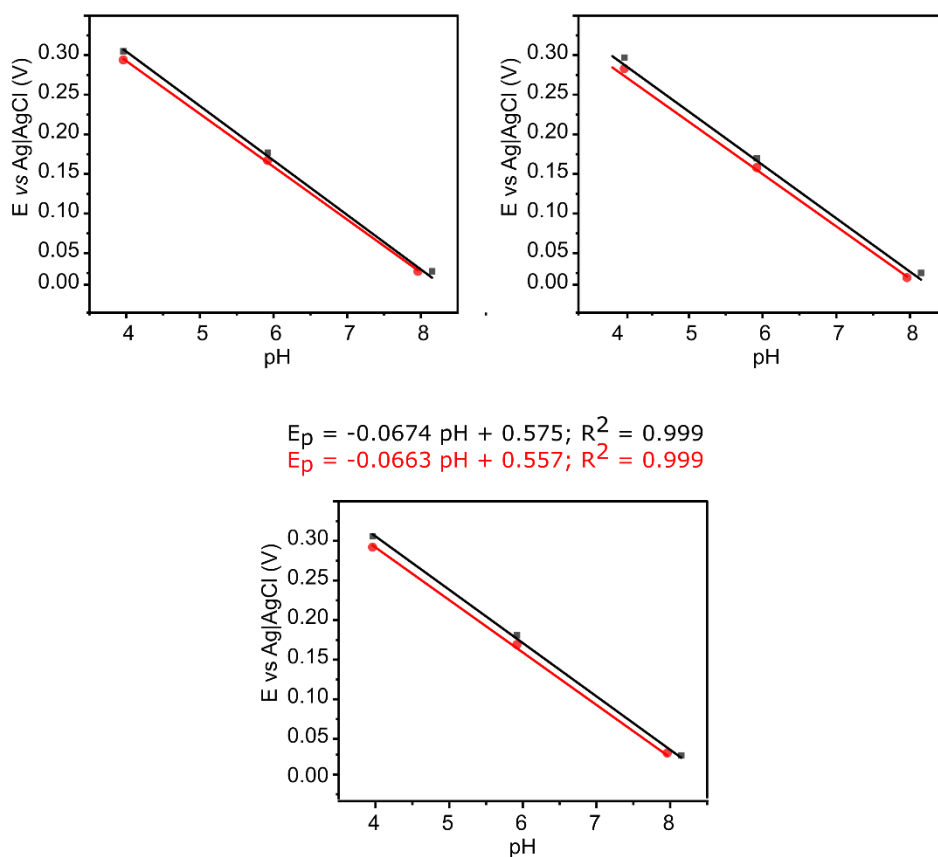
Figure 3.11. Before (black-square) and after (red-circle) calibration, after conducting nine measurements across the gastrointestinal tract

with rinsing between each measurement using three BDD-Q pH electrodes.

BDD-Q pH measurements across the mouse upper GI tract are shown in Figure 3.12, (a) in HEPES buffer only, (b) with the addition of 10 µM omeprazole and (c) with the addition of 1 µM melatonin, under stationary conditions. During these measurements the BDD-Q electrode was brought into contact with the tissue, to create the mechanical stimulus needed for acid secretion. Six tissues were used in total, i.e., $n = 6$, with the same BDD-Q electrode. The pH values recorded in Figure 3.12 represent the mean of these six samples, with the sample standard deviation as error bars. The pH was calculated using the buffer calibration recorded prior to each tissue measurement.
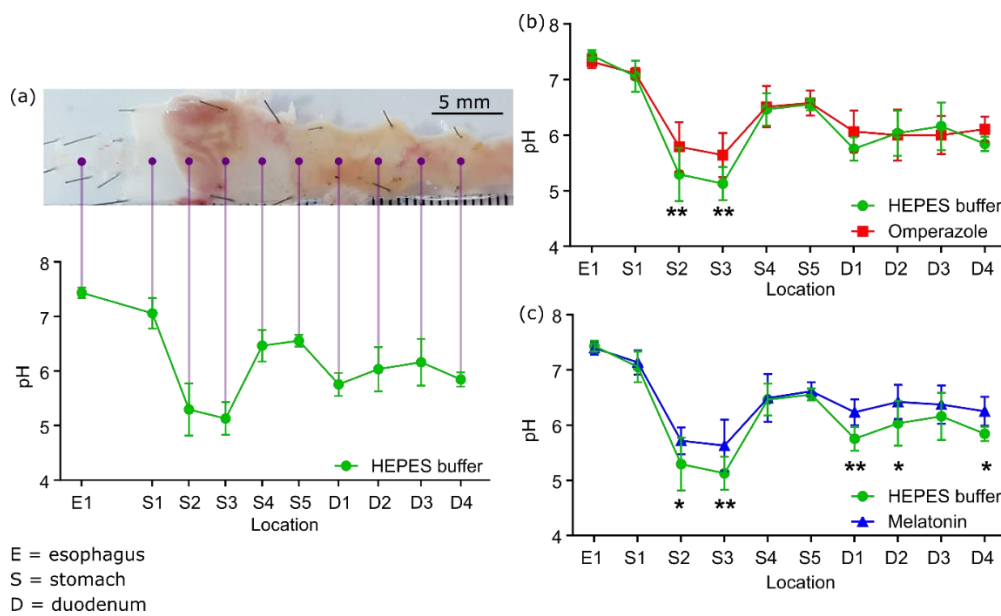
Figure 3.12. BDD-Q electrode measurements of the pH across different regions of mouse gastrointestinal tract in (a) HEPES buffer solution only (green line), (b) 10 µM omeprazole in HEPES buffer solution (red line), and (c) 1 µM melatonin in HEPES buffer solution (blue line). Data represents an average of 6 tissue sample, with standard deviation error bars, where **$p<0.01$ and *$p<0.05$. Note the HEPES buffer measurement in (a-c) is the same data and was recorded prior to addition of either omeprazole or melatonin.

In the absence of pharmacological treatments (Figure 3.12a), the oesophagus is found to be neutral (E1 pH = 7.43 ± 0.097), while the stomach goes from neutral (S1 pH = 7.06 ± 0.28) to slightly acidic (S2 pH = 5.29 ± 0.48; S3 pH = 5.13 ± 0.30), before becoming more alkaline (S4 pH = 6.46 ± 0.29; S5 pH = 6.56 ± 0.11) towards the duodenum, which itself is more alkaline (D1 pH = 5.75 ± 0.21; D2 pH = 6.03 ± 0.41; D3 pH = 6.16 ± 0.43; D4 pH = 5.85 ± 0.13). The stomach pH is slightly higher than expected, but this is due to the acid secreted from the cells being buffered by the HEPES solution (pK_a = 7.56). These results demonstrate the effectiveness of the BDD-Q electrode at recording GI tissue pH. Conducting these measurements under static conditions and in close proximity to the tissue, allows for accurate spatial pH measurement in multiple locations along the upper GI tract.

Having successfully recorded pH measurements in physiologically typical tissue, the effects of pharmacological treatments were explored. Figure 3.12b shows the effect of adding omeprazole (10 μM) to the HEPES buffer solution. Here, a two-way ANOVA at a 5% significance level, with the Sidak correction for multiple comparisons was employed. The data demonstrates statistical significance in the pH of the body region of the stomach (S2 and S3), where the pH has risen, S2 pH = 5.79 ± 0.48; S3 pH = 5.64 ± 0.30, compared to that in untreated tissue. The tissue was then rinsed and left for 20 mins in HEPES buffer solution in order to help the tissue recover its original state. The buffer was then replaced with fresh solution containing 1 μM of melatonin in order to study the effect of this hormone on tissue pH. The pH response after melatonin treatment is presented in Figure 3.12c. Statistically significant differences in pH were observed in the duodenum and stomach (two-way ANOVA with Sidak correction). The D1-D4 regions of the duodenum and the body regions of the stomach (S2 and S3) all became more alkaline *i.e.* (D1 pH = 5.99 ± 0.25; D2 pH = 6.23 ± 0.35; D3 pH = 6.30 ± 0.37; D4 pH = 6.05 ± 0.36) and (S2 pH = 5.72 ± 0.24; S3 pH = 5.63 ± 0.46) compared to pH measurements in the untreated tissue.

Omeprazole is a known PPI targeting the H^+/K^+-ATPase pump in the body regions of the stomach. The pH mapping measurements clearly highlight the *ex-vivo* action of omeprazole in suppressing gastric acid release in the body regions of the stomach (S2 and S3) of the GI tract, whilst leaving the oesophagus

and duodenum unaffected. Upon addition of melatonin (Figure 3.12c), a potent bicarbonate agonist,[13,63] the pH probe demonstrates a statistically significant increase in pH in the duodenum regions of the GI tract (specifically D1, D2 and D4). Melatonin is also thought to inhibit gastric acid production,[63] and the pH probe shows statistically higher pH, again in the body regions of the stomach compared to the untreated tissue. Whilst this response could be due to melatonin, however, as the pH values recorded are very similar to those determined in the presence of omeprazole, it is possible omeprazole was left behind, even after flushing the tissue with buffer post-treatment.

3.4. CONCLUSION

This study reports the first *ex-vivo* pH profile map of the upper GI tract (of a mouse) from oesophagus to duodenum, in the absence and presence of the pharmacological agents, omeprazole and melatonin, using an electrochemical pH sensor. pH electrodes for measurement in this *ex-vivo* environment ideally require the following properties, (i) high temporal resolution (the longer the measurement timescale the greater the impact of diffusional mixing from neighbouring zones); (ii) a meaningful spatial resolution, ≤ 1 mm for the tissue employed herein; (iii) robustness, as contact with the tissue was used to both mechanically stimulate acid release and maintain a constant height separation and (iv) minimal impact of biological adsorption. Of the three pH electrodes assessed, BDD-Q appeared the most promising, recording the fastest response time (6 s versus ~100's of s), having an appropriate spatial footprint, and suitable robustness for repeated contact with the tissue surface.

Using BDD-Q it was possible to track the pH falling from near neutral conditions in the oesophagus, to acidic in the stomach and rising to more alkaline in the duodenum. The importance of spatial resolution was illustrated by employing a small enough BDD-Q probe such that clear pH variations could be visualised even within specific regions of the GI tract (stomach). Utilising a robust, stable probe was also important in enabling the impact of pharmacological treatment protocols to be readily assessed on the same tissue using the same probe. Adding omeprazole caused the body regions of the stomach to rise in pH, whilst melatonin resulted in an increase in pH in both the

body regions of the stomach and the duodenum. To combat any possible electrode fouling from tissue contact the probe was briefly rinsed in between measurement. Future work would look to *in-situ* cleaning routes. Given, one advantage of a voltammetric sensor (BDD-Q), over a potentiometric one (BDD-IrOx and glass) is the ability to apply currents/voltages, electrochemical *in-situ* cleaning routes could be considered. Finally, possible future developments could also see this technology move from *ex-vivo* to *in-vivo* through incorporation of the BDD-Q sensor into endoscopic probes or ingestible wireless transmitting capsules.

3.5. REFERENCES

1   R. H. Hunt, Archives of internal medicine, 1999, 159, 649–657.

2   P. Holzer, American journal of physiology. Gastrointestinal and liver physiology, 2007, 292, G699-705.

3   D. J. Ostlie and G. W. Holcomb, Ashcraft's Pediatric Surgery, 2010, 379–390.

4   D. F. Evans, G. Pye, R. Bramley, A. G. Clark, J. Dyson, J. D. Hardcastle, T. J. Dyson and J. D. Hardcastle, Gut, 1988, 29, 1035–1041.

5   J. M. Maurer, R. C. A. Schellekens, H. M. Van Rieke, C. Wanke, V. Iordanov, F. Stellaard, K. D. Wutzke, G. Dijkstra, M. Van Der Zee, H. J. Woerdenbag, H. W. Frijlink and J. G. W. Kosterink, PLoS ONE, 2015, 10, 1–17.

6   M. Koziolek, M. Grimm, D. Becker, V. Iordanov, H. Zou, J. Shimizu, C. Wanke, G. Garbacz and W. Weitschies, Journal of Pharmaceutical Sciences, 2015, 104, 2855–2863.

7   G. Spencer and D. C. Metz, in Practical Gastroenterology and Hepatology: Esophagus and Stomach, eds. N. J. Talley, K. R. DeVault and D. E. Fleischer, Wiley-Blackwell, 2010, pp. 16–21.

8   I. M. P. Joseph, Y. Zavros, J. L. Merchant and D. Kirschner, Journal of Applied Physiology, 2003, 94, 1602–1618.

9   M. L. Schubert and D. A. Peura, Gastroenterology, 2008, 134, 1842–1860.

10   E. P. Widmaier, H. Raff and K. T. Strang, in Vander's Human Physiology, The Mechanisms of Body Function, McGraw-Hill Higher Education, 11th edn., 2008, pp. 528–565.

11   P. Lindberg, A. Brndstrm, B. Wallmark, H. Mattsson, L. Rikner and K. J. Hoffmann, Medicinal Research Reviews, 1990, 10, 1–54.

12   T. S. Kandil, A. A. Mousa, A. A. El-Gendy and A. M. Abbas, BMC Gastroenterology, 2010, 10, 1–9.

13   M. Sjöblom and G. Flemström, J. Pineal Res., 2003, 34, 288–293.

14   C. S. Bang, Y. J. Yang and G. H. Baik, Medicine, 2019, 98, e14241.

15   D. A. Skoog, F. J. Holler and S. R. Crouch, Principles of Instrumental Analysis, Cengage Learning, Boston, USA, 7th Editio., 2016.

16   M. T. Ghoneim, A. Nguyen, N. Dereje, J. Huang, G. C. Moore, P. J. Murzynowski and C. Dagdeviren, Chem Rev, 2019, 119, 5248–5297.

17   S. Głab, A. Hulanicki, E. Gunnar and F. Ingman, Crit Rev Anal Chem, 1989, 21, 29–47.

18   D. O'Hare, K. H. Parker and C. P. Winlove, Med Eng Phys, 2006, 28, 982–988.

19   D. Daomin Zhou, Microelectrodes for in-vivo determination of pH, Elsevier Inc., 2008.

20   S. R. Ng and D. O'Hare, Analyst, 2015, 140, 4224–4231.

21   L. Manjakkal, D. Szwagierczak and R. Dahiya, Progress in Materials Science, 2020, 109.

22   B. A. Patel, C. A. Anastassiou and D. O'Hare, in Body Sensor Networks, ed. G.-Z. Yang, Springer-Verlag London Limited, 2006, pp. 41–88.

23   S. A. M. Marzouk, S. Ufer, R. P. Buck, T. A. Johnson, L. A. Dunlap and W. E. Cascio, Analytical Chemistry, 1998, 70, 5054–5061.

24   V. M. Tolosa, K. M. Wassum, N. T. Maidment and H. G. Monbouquette, Biosensors and Bioelectronics, 2013, 42, 256–260.

25   A. N. Bezbaruah and T. C. Zhang, Analytical Chemistry, 2002, 74, 5726–5733.

26   P. J. Kinlen, J. E. Heider and D. E. Hubbard, Sensors and Actuators B, 1994, 22, 13–25.

27   W.-D. D. Huang, H. Cao, S. Deb, M. Chiao and J. C. Chiao, Sensors and Actuators, A: Physical, 2011, 169, 1–11.

28   G. M. da Silva, S. G. Lemos, L. A. Pocrifka, P. D. Marreto, A. V. Rosario and E. C. Pereira, Analytica Chimica Acta, 2008, 616, 36–41.

29   H. Kahlert, Journal of Solid State Electrochemistry, 2008, 12, 1255–1266.

30   F. E. Galdino, J. P. Smith, S. I. Kwamou, D. K. Kampouris, J. Iniesta, G. C. Smith, J. A. Bonacin, C. E. Banks, F. Flávia, E. Galdino, J. P. Smith, S. I. Kwamou, D. K. Kampouris, J. Iniesta, G. C. Smith, J. A. Bonacin and C. E. Banks, Anal. Chem., 2015, 87, 11666–11672.

31   V. G. H. Lafitte, W. Wang, A. S. Yashina and N. S. Lawrence, Electrochemistry Communications, 2008, 10, 1831–1834.

32   M. Lu and R. G. Compton, Analyst, 2014, 139, 4599–4605.

33   M. Lu and R. G. Compton, Analyst, 2014, 139, 2397–2403.

34   Z. J. Ayres, A. J. Borrill, J. C. Newland, M. E. Newton and J. V Macpherson, Anal. Chem., 2016, 88, 974–980.

35   G. G. Wildgoose, M. Pandurangappa, N. S. Lawrence, L. Jiang, T. G. J. Jones and R. G. Compton, Talanta, 2003, 60, 887–893.

36   P. T. Lee, J. C. Harfield, A. Crossley, B. S. Pilgrim and R. G. Compton, RSC Advances, 2013, 3, 7347–7354.

37   S. J. Cobb, Z. J. Ayres, M. E. Newton and J. V. Macpherson, J Am Chem Soc, 2019, 141, 1035–1044.

38   C. Dai, P. Song, J. D. Wadhawan, A. C. Fisher and N. S. Lawrence, Electroanalysis, 2015, 27, 917–923.

39   C. Dai, C.-W. I. Chan, W. Barrow, A. Smith, P. Song, F. Potier, J. D. Wadhawan, A. C. Fisher and N. S. Lawrence, Electrochimica Acta, 2016, 190, 879–886.

40   E. Bitziou, D. O'Hare and B. A. Patel, Analytical Chemistry, 2008, 80, 8733–8740.

41   E. Bitziou and B. A. Patel, American Journal of Physiology - Gastrointestinal and Liver Physiology, 2012, 303, 396–403.

42   I. Synnerstad, M. Johansson, O. Nylander and L. Holm, American Journal of Physiology - Gastrointestinal and Liver Physiology, 2001, 280, G121–G129.

43   C. Schade, G. Flemström and L. Holm, Gastroenterology, 1994, 107, 180–188.

44   S. Fierro, R. Seishima, O. Nagano, H. Saya and Y. Einaga, Scientific Reports, 2013, 3, 3257.

45   K. Kalantar-Zadeh, N. Ha, J. Z. Ou and K. J. Berean, ACS Sensors, 2017, 2, 468–483.

46   A. E. Mikolajczyk, S. Watson, B. L. Surma and D. T. Rubin, Clinical and Translational Gastroenterology, 2015, 6, 100.

47   L. A. Beardslee, G. E. Banis, S. Chu, S. Liu, A. A. Chapin, J. M. Stine, P. J. Pasricha and R. Ghodssi, ACS Sensors, 2020, 5, 891–910.

48   J. Perez-Vilar and R. L. Hill, The Journal of Biological Chemistry, 1999, 274, 31751–31754.

49   A. P. Corfield, BBA - General Subjects, 2015, 1850, 236–252.

50   A. Fagan-Murphy, F. Watt, K. A. Morgan and B. A. Patel, Journal of Electroanalytical Chemistry, 2012, 684, 1–5.

51   W. R. Carmody, J. Chem. Educ., 1961, 38, 559–560.

52   S. J. Cobb, F. H. J. Laidlaw, G. West, G. Wood, M. E. Newton, R. Beanland and J. V Macpherson, Carbon, 2020, 167, 1–10.

53   L. Hutton, M. E. Newton, P. R. Unwin and J. V Macpherson, Anal. Chem, 2009, 81, 1023–1032.

54   Z. J. Ayres, S. J. Cobb, M. E. Newton and J. V Macpherson, Electrochemistry Communications, 2016, 72, 59–63.

55   M. Toledo, 2014, 44.

56   C. Kilkenny, W. J. Browne, I. C. Cuthill, M. Emerson and D. G. Altman, PLoS Biology, 2010, 8, 1–5.

57   H. Larsson, E. Carlsson, U. Junggren, L. Olbe, S. E. Sjöstrand, I. Skånberg and G. Sundell, Gastroenterology, 1983, 85, 900–907.

58   M. Toledo, 2014, 44.

59   S. Kakooei, C. Ismail and B. Ari-Wahjoedi, International Journal of Material Science Innovations (IJMSI), 2013, 1, 62–72.

60   G. Klinkenberg, K. Q. Lystad, D. W. Levine and N. Dyrset, Journal of Applied Microbiology, 2001, 91, 705–714.

61   N. R. Wilson, S. L. Clewes, M. E. Newton, P. R. Unwin and J. V. Macpherson, Journal of Physical Chemistry B, 2006, 110, 5639–5646.

62   S. J. Cobb and J. V. Macpherson, Analytical Chemistry, 2019, 91, 7935–7942.

63   C. S. Bang, Y. J. Yang and G. H. Baik, Medicine, 2019, 98, e14241.

Chapter 4. CHARACTERISING THE IMPACT OF BIOLOGICAL FOULING ON CARBON ELECTRODES USING ELECTROCHEMICAL TECHNIQUES

4.1. INTRODUCTION

A major factor limiting the use of electrochemical sensors for biological studies is the fouling caused by the complex biological matrix itself. Fouling typically involves the passivation of an electrode surface by an agent that forms an impermeable or partially permeable layer on the surface, modifying charge and electron transfer at the electrode/electrolyte interface.[1] Electrode fouling can negatively affect the sensitivity, detection limit, reproducibility, and reliability of the electrochemical sensor.[1,2] In particular, in vivo measurements expose the sensors to a complex matrix of proteins, which easily adsorb on the sensing surface.[3]

Electrode fouling that occurs by the adsorption of biological macromolecules is mostly due to proteins as a result of their abundance in biological samples. It is well documented that the adsorption of proteins to surfaces is a complex process, not driven or dominated by any single factor but a combination of several factors.[4] Some of the factors that can affect protein absorption are: (i) the type and concentration of protein; (ii) the temperature (under most conditions the adsorption is an endothermic process); (iii) the ionic strength; (iv) size (smaller proteins diffuse quicker and arrive at the surface faster), and; (v) the pH which can affect the overall charge of the protein (minimise protein-protein repulsions while at their isoelectric point, pI).[4–6] The types and quantity of proteins that are adsorbed to a material surface, as well as their arrangement, orientation, and conformation, depends not only on the solution conditions but also the characteristics of the material surface such as surface chemistry (hydrophobicity), roughness, and charge.[5]

Carbon-based electrodes, such as glassy carbon (GC), pyrolytic carbon, reduced graphene oxide, carbon nanotubes, and boron doped diamond (BDD), have been favoured in medical/bio-related devices, due to their biocompatibility, low background currents, cost, and the capability for surface regeneration.[7]

Several electrochemical techniques, such as, cyclic voltammetry (CV),[8–14] chronoamperometry (CA),[15] electrochemical impedance spectroscopy (EIS),[11,16–18] and electrochemical quartz crystal microbalance,[19–21] either individually, or in combination with non-electrochemical techniques, have been used to study protein adsorption on electrode surfaces.

Blood is an example of a complex biological fluid which contains a mixture of different proteins with potential to cause fouling.[22] Of particular interest is serum albumin, which regulates the colloidal osmotic pressure of blood, and is by far, the most abundant protein in blood.[23,24] Bovine serum albumin (BSA) fouling of electrode surfaces has been studied by probing the faradaic response of a surface-sensitive redox couple (ferrocyanide) and a biologically relevant redox species (dopamine), using CV and EIS.[11] The data showed that BDD generally exhibited the least fouling in most conditions compared to GC.

Further studies found that adsorption of human serum albumin on gold was promoted by both positive and negative applied potentials, as shown by in situ ellipsometry.[25] Complementary CV measurements of the redox behaviour of ferricyanide indicated partial blocking of the electrode surface as determined from the reduction in peak currents.[25] A comprehensive study was recently conducted on the effect of BSA and fetal bovine serum (FBS) adsorption on the electron transfer kinetics of a positively and negatively charged redox complex ($Ru(NH_3)_6^{3+}$ and $IrCl_6^{2-}$) on both tetrahedral amorphous carbon (ta-C), and SU-8 based pyrolytic carbon (PyC).[12] Redox behaviour on PyC was observed to be less affected by BSA and FBS than for a ta-C electrode. For these experiments, the redox responses were not recorded in solutions containing the BSA/FBS, instead the electrodes were transferred between solutions with protein, and solutions with redox mediators. Hence it is difficult from this study to translate the results to *in-vivo* studies, where the analyte of interest is present in a complex mixture with proteins.

Similarly, mucins are a family of glycoproteins critical in maintaining the homeostasis in harsh environments.[26] These include the air-water interface of the respiratory system, the acidic environment of the stomach, and secretory epithelial surfaces of specialised organs (liver, pancreas, eye, etc.) that fluctuate

in pH, ionic concentration, oxygenation, and hydration.[27–29] Fouling of electrochemical sensors due to the presence of mucin is also a well-known issue, as discussed in Chapter 3.[15,30–32] Previously, 0.5% mucin was found to be detrimental to the detection of serotonin using CV on GC and BDD.[30] Interestingly, the same study also demonstrated that 5% BSA showed no fouling on BDD and GC electrodes.[30] A separate study focusing on BDD, explored the time dependent effect 0.5% mucin can have on the double-layer capacitance (C_{dl}) of BDD over a period of 30 mins using both CA and EIS. The results demonstrated that upon exposure to mucin, the C_{dl} increased slightly, then decreased to reach a plateau by 30 mins.[15] This decrease in C_{dl} was associated with fouling of the oxygen-terminated BDD surface, which is hydrophilic and can likely interact with mucin, through the hydrophilic carbohydrate side chains of the glycoprotein.

In our previous work we have developed and studied the use of localised sp^2-bonded carbon on BDD (sp^2-BDD) as an electrode surface capable of detecting pH changes in the gastrointestinal tract (*ex-vivo*, Chapter 3)[31] and in blood (*in-vitro*).[33] The accurate characterisation of sensors and biological fouling is crucial for the optimisation of medical devices that interact with complex biological environments. Inaccurate or incomplete characterisation may hinder the discovery of promising biomaterials, as initial findings may not translate to *in-vivo* assessments. In this chapter we investigate the effect of different biological matrices on the electrochemical responses of BDD, sp^2-BDD, and GC in the presence of mucin and BSA at their biological concentrations (0.5% and 5% (w/v) respectively). For these studies, the entire sp^2-BDD surface was converted from BDD to non-diamond carbon using a laser ablation process.[34] The BDD is an sp^3 bonded carbon electrode whilst GC is an sp^2 bonded carbon electrode which shows short range crystallinity.[35] High resolution transmission electron microscopy and electron energy loss spectroscopy studies reveal the sp^2-BDD electrode surface comprises of a very thin layer of ordered graphite capped with an ultra-thin layer of amorphous carbon.[36] Comparing the response of the three different electrode surfaces will be of interest, especially given our interest in using hybrid sp^2-BDD electrodes for biological electrochemical sensing (Chapters 3 and 5).[33]

To investigate time dependent fouling, CV of hexaamineruthenium ($Ru(NH_3)_6^{3+/2+}$) and hexachloroiridate ($IrCl_6^{2-/3-}$) were recorded in the presence of mucin and BSA. Secondly, the change in C_{dl} was examined in 0.1 M KCl solution under positive and negative potentials in the absence and presence of fouling agents using CV. Finally, we explored the potential dependence on protein film formation, and the subsequent effect it can have on the electrochemical deposition of silver.

4.2. EXPERIMENTAL

4.2.1. Chemicals

Solutions were prepared using ultrapure water (Milli-Q, resistivity ≥ 18.2 MΩ cm at 25°C). All chemicals were used as received. Measurements were carried out in 0.1 M potassium chloride (KCl, extra pure, Acros Organics) with 1 mM hexaamineruthenium (III) chloride ($Ru(NH_3)_6^{3+}$, 99%, Strem Chemicals), or 1 mM potassium hexachloroiridate (IV) ($IrCl_6^{2-}$, 99.99%, Sigma Aldrich). Effects of a biological matrix was simulated by adding 0.5% (w/v) mucin from porcine stomach Type II (Sigma Life Science), or 5% (w/v) bovine serum albumin (BSA, ≥ 96%, Sigma Life Science) to 0.1 M KCl. Silver electrodeposition was conducted using 1 mM silver nitrate ($AgNO_3$, 99.99%, Sigma Aldrich) dissolved in 1 M potassium nitrate (KNO_3, 99+%, Acros Organics). Solution pH was measured using a Mettler Toledo SevenGo pH portable meter and InLab Expert Go-ISM glass probe, kept in the Mettler Toledo InLab storage solution when not in use. All electrodes, before use, were polished with alumina (0.05 μm, Buehler, Germany) paste on a MicroClothTM polishing pad (Buehler), and then on a wetted (ultrapure water) alumina-free pad.

4.2.2. Electrode preparation

Cylinders of polycrystalline BDD with a 1 mm diameter (boron dopant density >10^{20} B atoms cm^{-3}, minimal sp^2-carbon content,[37] Element Six) were machined from a 6 inch freestanding polycrystalline BDD wafer using a 355 nm Nd:YAG 34 ns laser micromachiner E-355H-ATHI-O system, Oxford Lasers). The wafer was of 357 μm thickness with nanometre scale roughness of the growth

face, achieved through polishing. Once the BDD discs were cut, they were acid cleaned for 30 minutes in ~200 °C, concentrated H_2SO_4 (analytical reagent grade ≥ 95 %, Fischer Scientific) that had been saturated with KNO_3, followed by a second 30 minute treatment in ~200 °C, concentrated H_2SO_4, to remove any loosely bound sp^2.[36] The BDD discs were annealed at 600°C in air for 5 hours to minimise any non-diamond carbon on the sidewalls from the laser machining process.[36] To prepare the sp^2-BDD electrodes, the surface of the acid cleaned BDD discs were laser micromachined (with fluence of 14 J cm-1, just above the ablation threshold of BDD)[33,34] in a spiral pattern to leave a layer of sp^2 bonded carbon covering the entire BDD surface. A similar high temperature oxidative acid treatment, as for the BDD discs, was followed to remove any loosely bound sp^2-carbon.

To provide an electrical contact Ti (10 nm) / Au (400 nm) was sputtered (Moorfields MiniLab 060 platform sputter/evaporator) onto the backside (lapped ~100 nm roughness) of the discs, then annealed at 400 °C in air for 5 hours to form an ohmic contact.[38,39] These BDD and sp^2-BDD discs were then sealed in glass capillaries (O.D. 2 mm; I.D. 1.16 mm, Harvard Apparatus Ltd., Kent, UK) using the procedure outlined in Chapter 2.[38,40] The electrode surface and laser profiles were analysed via optical microscopy (Leica DM4000M) and white light interferometry (WLI; Contour GT, Bruker) prior to electrochemical characterization.

4.2.3. Electrochemical measurements

For all electrochemical measurements a three-electrode configuration was used on an Ivium compactstat (Ivium Technologies B.V.). All CV measurements were performed using the current averaging mode[41] on the Ivium, recommended for analysis of surface adsorbed species, in aerated solutions (unless otherwise stated). A saturated calomel electrode (SCE, IJ Cambria Scientific Ltd.) and a coiled platinum wire (Goodfellow) served as the reference and counter electrodes, respectively. The SCE was routinely monitored for any drift (relative to a master SCE reference electrode), given its use in fouling solutions. The coiled Pt wire counter electrode was flame cleaned before use to remove any unwanted contaminants. 1 mm BDD, sp^2-BDD, or 3 mm GC (CH

Instruments, IJ Cambria Scientific Ltd.) electrodes were used as the working electrode.

The diffusion coefficient, D, of 1 mM $Ru(NH_3)_6^{3+/2+}$ in 0.1 M KCl was determined by steady-state CV using a platinum microelectrode (diameter = 26.5 µm measured optically) at a scan rate of 5 mV/s. 0.5% mucin or 5% BSA was dissolved in the 1 mM $Ru(NH_3)_6^{3+/2+}$ solution to study the effect of protein presence on D ($Ru(NH_3)_6^{3+}$). The C_{dl} of the three carbon-based electrodes were determined using current averaging CV with a window of 200 mV at three potentials ranges (1) -0.1 to 0.1 V, (2) 0.3 to 0.5 V and (3) -0.5 to -0.3 V, at 50 mV/s scan rate.

For all experiments involving $AgNO_3$, a leak-free silver-silver chloride (Ag|AgCl, 3 M KCl, Alvatek Ltd., UK) reference was employed, to avoid any chloride contamination from the porous frit of the SCE reference. Leakage of chloride ions can result in the formation of AgCl precipitate. All $AgNO_3$ solutions were purged in Ar to avoid any side reactions from the presence of oxygen. Each electrode was held at +0.4 V or -0.4 V vs SCE for 900 s in a 0.1 M KCl solution containing either 0.5% mucin or 5% BSA, and the electrode was gently rinsed before placing in $AgNO_3$ solution, to record CV at 100 mV/s.

4.2.4. Kinematic viscosity measurement

Kinematic viscosity is measured using a gravimetric U-tube capillary ("Q" Glass Company, inc., Routine, size 300) viscometer by recording the time it takes for solution to travel through the orifice of the capillary (from the start mark to the stop mark) under the force of gravity. Equation 4.1 is used to calculate the kinematic viscosity of the solution of interest, η_s, at 22°C,

$$\eta_s = \frac{\eta_w \rho_s t_s}{\rho_w t_w}$$ Equation 4.1

where η_w is the kinematic viscosity of water, ρ_s and ρ_w is the density of the solution of interest and water respectively, and t_s and t_w is the time taken for the solution meniscus and water meniscus to drop from the start to stop mark. The flow of an aqueous solution 0.1 M KCl containing 1 mM $Ru(NH_3)_6^{2+}$ or 1 mM $IrCl_6^{2-}$ in the absence and presence of 5% w/v albumin and 0.5% w/v mucin was

recorded (n = 6), and the average time taken to flow between the two points used to calculate the kinematic viscosity.

4.2.5. White Light Laser Interferometry

White light laser interferometry (WLI) images were recorded using a Bruker ContourGT (Bruker Nano Inc., Tuscon, AZ, USA). A three-dimensional (3D) rendering of interferometry data was performed and the roughness of the GC electrode surface was quantifies using Gwyddion 2.41 (Czech Metrology Institute, CZE). An average of the roughness profiles across the electrode surface is reported.

4.2.6. Field Emission Scanning Electron Microscopy (FE-SEM)

A Zeiss SUPRA 55 VP FE-SEM was used with an in-lens detector and a secondary electron emission detector to obtain images of BDD and sp^2-BDD, with Ag nanoparticles (NPs) at 5 kV. The NPs had been electrochemically deposited by holding at -0.2 V vs Ag|AgCl for 60 s, on either a freshly alumina polished (and rinsed) surface or on a surface modified with 0.5% mucin or 5% BSA by holding at +/- 0.4 V vs SCE for 900 s.

4.2.7. Data Analysis

D was calculated by averaging the current over 100 mV of the CV plateau region. The limiting current at a disc microelectrode, i_{lim}, is expressed in Equation 4.2,

$$i_{lim} = 4naFDC \hspace{3cm} \text{Equation 4.2}$$

where n is the number of electrons (= 1), a is the electrode disk radius (= 0.00133 cm), F is the Faraday constant (= 96485 $Cmol^{-1}$), and C is the analyte concentration (1×10^{-6} mol cm³). The CV macroelectrode data were analysed by measuring the cathodic or anodic peak current, i_{pc} or i_{pa}, and the peak-to-peak separation, ΔE_p. ImageJ software has been used to analysis the particle sizes in the FE-SEM images for the silver electrodeposition on BDD and BDD-Q electrodes.

4.3. RESULTS AND DISCUSSION

4.3.1. Faradaic: Effect of biological matrices on the response of redox couples

Diffusion coefficient measurement using platinum microelectrode

The presence of proteins in solution can directly affect the D of redox molecules, due to an increase in solution viscosity.[42] A Pt microelectrode (diameter = 26.5 µm) was used to estimate D of $Ru(NH_3)_6^{3+}$, (Figure 4.1a) and D of $IrCl_6^{2-}$ in 0.1 M KCl (Figure 4.1b), in the absence, pH 6.32 (Figure 4.1, black) and in the presence of 0.5% (w/v) mucin, pH 3.80 (Figure 4.1, red) under degassed conditions. The same experiment was carried out in 5% (w/v) BSA, pH 6.96 (Figure 4.1, blue).
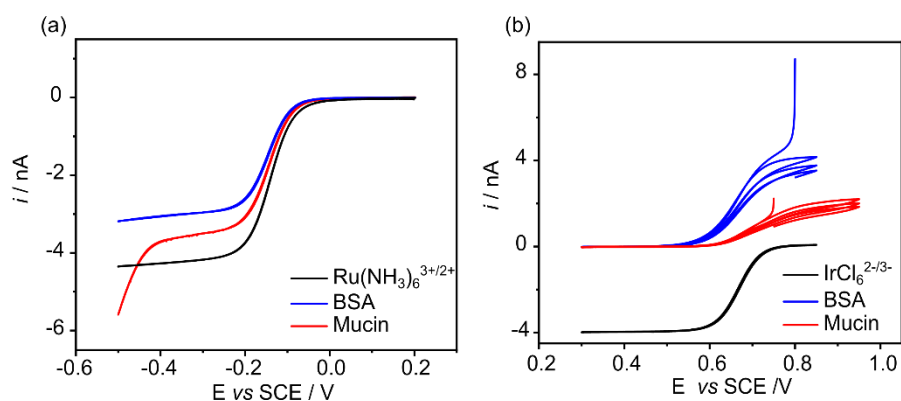
Figure 4.1. CVs of (a) 1 mM $Ru(NH_3)_6^{3+/2+}$ and (b) 1 mM $IrCl_6^{2-/3-}$ in 0.1 M KCl (black, solid line) performed using Pt microelectrode (diameter = 26.5 µm), with 0.5% mucin (red) and 5% BSA (blue) at 5 mV/s, performed under Ar.

In the absence of proteins in Figure 4.1a, for $(Ru(NH_3)_6)^{3+}$, the current reaches steady state at -4.31 nA, and D calculated using Equation 4.2 was 8.30 $\times 10^{-6} \pm 0.07$ cm^2/s (n = 3), is in good agreement with the literature value of 8.43 $\times 10^{-6}$ cm^2/s ($\pm$ 0.03).[43] Upon addition of 0.5% mucin, the pH of the solution drops from pH 6.32 to pH 3.80, and the current reaches steady state at -3.59 nA. The further increase in current past the plateau region is most likely due to proton reduction in the more acidic solution. In the presence of mucin, D ($Ru(NH_3)_6^{3+}$) has dropped by 23% to 6.87 $\times 10^{-6} \pm 0.09$ cm^2/s, and with BSA (pH 6.96),

it has dropped by 34% to $5.87 \times 10^{-6} \pm 0.09$ cm^2/s. This data indicates that the presence of proteins has clearly affected the diffusion of $(Ru(NH_3)_6)^{3+}$ to the electrode surface, with BSA having the greatest affect. The theoretical D for $Ru(NH_3)_6{}^{3+}$ was calculated for mucin and BSA containing $Ru(NH_3)_6{}^{3+}$ solution, using the Stokes-Einstein equation (Equation 4.1),

$$D = \frac{k_B T}{6\pi \eta_s R_0}$$ Equation 4.1

where, k_B is the Boltzmann's constant (1.38×10^{-23} J/K), T is temperature (K), η_s is the kinematic solution viscosity (cm^2/s), and R_0 is the solute radius calculated based on the D measured for $(Ru(NH_3)_6)^{3+}$. The kinematic viscosity of the protein solutions with redox mediators were measured using a capillary U-tube viscometer and calculated using Equation 4.1, for mucin and albumin was 1.23 and 1.21 mm^2/s respectively. From this the D was estimated, giving 6.78 and 6.77 $\times 10^{-6}$ cm^2/s for mucin and BSA respectively. This suggests the difference in D observed in mucin is due to the increase in solution viscosity. However, in the presence of BSA, in addition to the increased viscosity, there is possibly also an adsorption event driving the change in D.

Figure 4.1b shows sigmoidal curves as expected for the reduction of $(IrCl_6)^{2-}$ to $(IrCl_6)^{3-}$. Using Equation 4.1, D was calculated as $7.74 \times 10^{-6} \pm 0.01$ cm^2/s. However, the scans in BSA and mucin are very different. At the potential where zero current should flow, the microelectrode is showing a positive current suggesting that there is an additional non-electrochemical pathway for $(IrCl_6)^{2-}$ to be converted to $(IrCl_6)^{3-}$. This means upon starting the scan there is a sizeable concentration of $(IrCl_6)^{3-}$ at the electrode surface which gets electrochemically oxidised to $(IrCl_6)^{2-}$ at the start of the scan. One possible explanation could be that the proteins are acting as reducing agents[44–46] to convert $(IrCl_6)^{2-}$ to $(IrCl_6)^{3-}$ in solution prior to starting the scan.

Ruthenium hexaammine cyclic voltammetry response

In order to probe the time-dependent adsorption of biologically relevant concentrations of mucin and BSA on the three different carbon-based electrode surfaces, the electron transfer kinetics of two differently charged redox probes,

Ru(NH$_3$)$_6$$^{3+/2+}$ and IrCl$_6$$^{2-/3-}$ were investigated by observing the change in the ΔE_p with time. Also included are the responses in a protein free solution i.e., 0.1 M KCl only (the control solution). Also monitored was the change in the reductive (for Ru(NH$_3$)$_6$$^{3+/2+}$ and IrCl$_6$$^{2-/3-}$) peak currents densities, j_{pc}, calculated using the geometric area of each electrode. Figure 4.2 shows (a) j_{pc} and (b) ΔE_p analysed from the CV recorded continuously for 912 s (one cycle takes 16 s, hence 57 CVs recorded) for (i) BDD, (ii) sp^2-BDD, and (iii) GC electrodes. The solution used contained 1 mM Ru(NH$_3$)$_6$$^{3+/2+}$ in 0.1 M KCl supporting electrolyte, no proteins added (black, squares), 0.5% w/v mucin (red, circles) and 5% w/v BSA (blue, triangles). Each data point represents the mean of n = 3, with standard deviation error bars.

Figure 4.2. (a) The cathodic peak current density, and (b) the peak-to-peak separation between anodic and cathodic peak potentials for the reduction of 1 mM Ru(NH$_3$)$^{3+/2+}$ in 0.1 M KCl, with 0.5% (w/v) mucin or 5% (w/v) BSA, performed using (i) BDD, (ii) sp^2-BDD, and (iii) GC electrodes in aerated solutions, at 100 mV/s for 912 s (average of n = 3, with standard deviation error bars).

In Figure 4.2, in the absence of proteins (black, squares), j_{pc} and ΔE_p for Ru(NH$_3$)$_6$$^{3+}$ reduction on BDD remains relatively stable at ~0.27 mA/cm^2 and
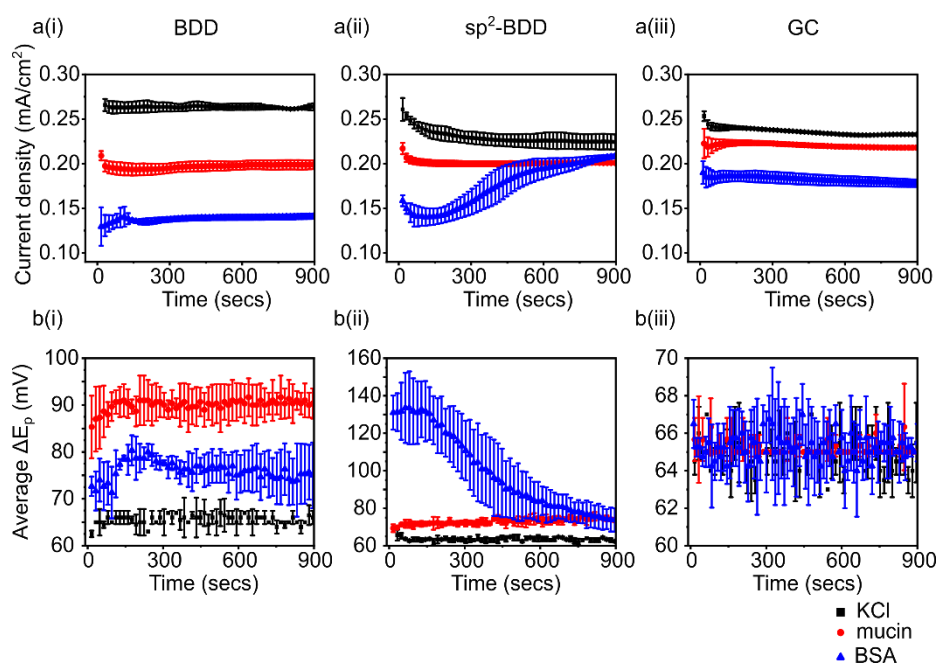
~65 mV respectively from the first scan to the last scan at 912 s. Similar behaviour is observed for sp^2-BDD and GC except the current takes a little longer to stabilise. ΔE_p also shows minimal change over time for both sp^2-BDD and GC, varying from 63 to 66 mV. All ΔE_p values are close to that expected for a diffusion-controlled reaction, 57 mV/n.[47]

The first scan after addition of 0.5% mucin (red, circles), shows that the j_{pc} for the reduction Ru(NH$_3$)$_6$$^{3+}$ on BDD has decreased by 22% to 0.21 mA/cm^2, and stabilises at 0.19 mA/cm^2, and ΔE_p has increased to 85 mV reaching a stable 90 mV by 912 s. Similarly, on sp^2-BDD, in the first scan, j_{pc} decreased to 0.22 from 0.26 mA/cm^2 (15%) in the absence of proteins and stabilised to 0.20 mA/cm^2 by 900 s. ΔE_p in the presence of mucin has increased to 69 mV and continues to slowly increase over 912 s to 74 mV. The first scan in the presence of mucin using GC also shows a decrease in j_{pc} to 0.22 mA/cm^2 (12%) which remains stable over time, however, ΔE_p shows minimal difference (64 to 66 mV) from the solution containing only Ru(NH$_3$)$_6$$^{3+}$. In the presence of mucin, from Figure 4.1, D for Ru(NH$_3$)$_6$$^{3+}$ was observed to decrease by 23%. Under macroelectrode conditions, the decrease in j_{pc} is similar, although interesting this decrease is less for the sp^2-BDD and GC electrodes. Whilst increased viscosity must be playing a role it is also useful to consider the changes in ΔE_p, whilst minimal for GC, there is a small, but notable increase for both BDD and sp^2-BDD, above the values recorded in just background electrolyte. This could indicate possible adsorption on these electrodes surfaces of the mucin which is impacting electron transfer.

The first CV scan after the addition of 5% BSA on BDD indicates a 52% decrease in j_{pc} (Ru(NH$_3$)$_6$$^{3+}$) from 0.27 to 0.13 mA/cm^2, which stabilises at 0.14 mA/cm^2 in 900 s, with ΔE_p varying from 73 mV (first scan) to a highest of 90 mV. The greatest effect of BSA is observed on the sp^2-BDD electrode, with j_{pc} starting at 0.16 mA/cm^2 in the first scan and reaching a lowest of 0.14 mA/cm^2 by 112 s (7th scan), but then increasing to 0.21 mA/cm^2 at 912 s (57th scan). Interestingly, the observed changes in j_{pc} over time correlates with a decrease in ΔE_p, starting at 131 mV, reaching a high of 134 mV at 80 s (5th scan) and dropping to 74 mV at 912 s (57th scan). This indicates that although BSA initially affects the peak current, and impedes electron transfer, over time the electrode recovers from the fouling causes by BSA and reaches a response closer to that observed in the

absence of any proteins. Furthermore, the reproducibility of the results (n = 3) suggests that this is a real effect.

The first scan on GC, shows 24% (0.19 mA/cm^2) decrease in j_{pc} caused by BSA, which stabilises at 0.18 mA/cm^2 by 912 s, and again ΔE_p shows minimal effect from BSA. The changes observed in GC can be correlated with the increase in viscosity, which in turn reduces the D for Ru(NH$_3$)$_6^{3+}$ (Figure 4.1a). However, the increased ΔE_p and the greater reduction in j_{pc} on BDD again likely indicates a combination of adsorption and viscosity changes. Furthermore, electron transfer kinetics at BDD and sp^2-BDD appear more affected by proteins than at GC. BDD inherently exhibits a lower electron transfer rate constant, k^0, than GC,[48] hence any changes in electron transfer at the electrode surface caused by the presence of proteins are likely to be more exaggerated on BDD than GC.

The data shown in Figure 4.3 are the CV responses for 1 mM Ru(NH$_3$)$_6^{3+/2+}$ for (i) BDD, (ii) sp^2-BDD and (iii) GC electrodes, at times of 16, 128, 480, and 912 s after addition of (a) 0.5 % mucin or (b) 5 % BSA, equivalent to scans 1, 8, 30, and 57. Initially, before addition of protein, and just in 0.1 M KCl, the voltammetric peak shape (black line) observed at all the electrodes corresponds to a diffusion-controlled, redox probe freely exchanging electrons with the electrode surface.
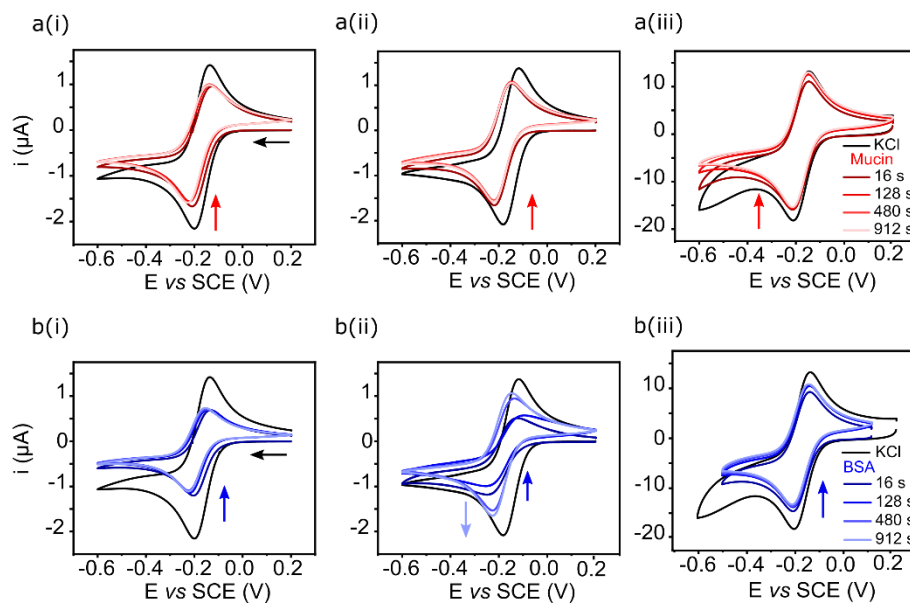
Figure 4.3. CVs for the reduction of 1 mM $Ru(NH_3)_6^{3+/2+}$ in 0.1 M KCl (black) obtained in the presence of (a) 0.5% mucin and (b) 5% BSA, using (i) BDD, (ii) sp^2-BDD, and (iii) GC electrodes, in aerated solutions at scan rate of 100 mV/s. CVs were acquired over 912 s.

For BDD, the CVs show slight distortions in the peak over time and the greatest decrease in current on the first scan. For sp^2-BDD, the voltammograms in the presence of 5% BSA show more clearly how the shape of the CV evolves over time. With repeated scanning the CV is more peak-shaped and the current increases. This evolution suggests that whilst BSA is adsorbing on the electrode surface and impeding electron transfer during the early scans, with time, the BSA may be desorbing from the surface, as electron transfer is becoming less hindered, and the current is increasing. This is the most interesting as it is the only system where there is a measurable increase in the rate of electron transfer with increasing scan number.

For the GC electrode, the presence of a second electron transfer process is noted at -0.5 V, which is attributed to the oxygen reduction reaction, ORR (Figure 4.3a, b(iii)). Interestingly, in the presence of mucin or BSA with continuous scans, its presence is less obvious, suggesting adsorption of both these proteins on the GC surface is impeding ORR (a surface sensitive reaction).

Hexachloroiridate cyclic voltammetry response

Proteins are charged molecules, where the overall charge is dictated by the pI of the protein. Mucin and BSA have a pI between pH 2-3[49] and 4-5[50] respectively. The pH of the 1 mM Ru(NH$_3$)$_6^{3+}$ solutions used with mucin and BSA were, 3.80 and 6.96 respectively. Hence under these conditions the protein molecules are overall negatively charged. An interesting experiment was therefore to explore the impact adsorption of a negatively charged molecule could have on a negatively charged outer-sphere redox couple, such as, IrCl$_6^{2-/3-}$. Figure 4.4 shows the reduction of IrCl$_6^{2-/3-}$ on (i) BDD, (ii) sp^2-BDD and (iii) GC electrodes at times of 14, 126, 476, and 910 s after addition of (a) mucin or (b) BSA, equivalent to scans 1, 9, 34, and 65.
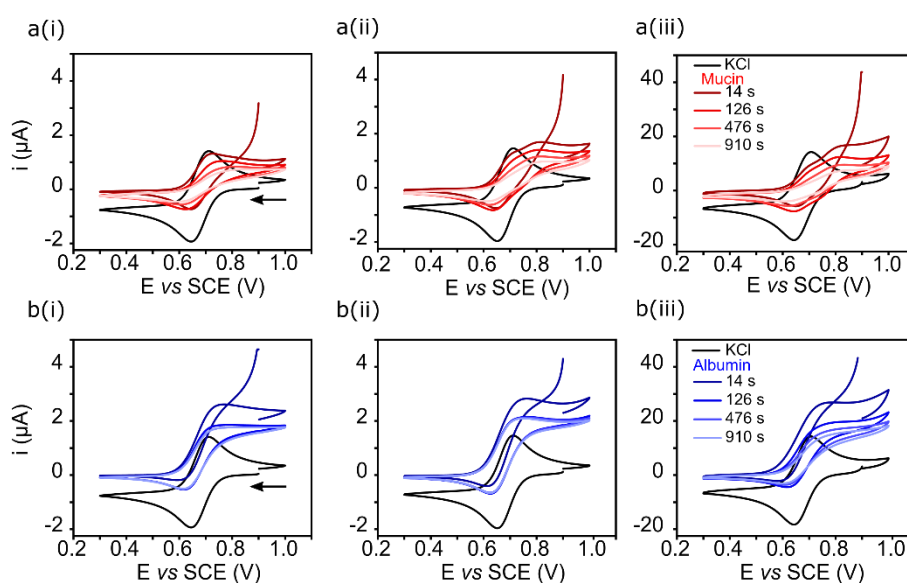
Figure 4.4. CVs for the reduction of 1 mM IrCl$_6^{2-/3-}$ in 0.1 M KCl (black) obtained in the presence of (a) 0.5% mucin and (b) 5% BSA, using (i) BDD, (ii) sp^2-BDD, and (iii) GC electrodes, in aerated solutions at scan rate of 100 mV/s. CVs were acquired over 910 s.

In contrast to Ru(NH$_3$)$_6^{3+}$, the electron transfer kinetics for IrCl$_6^{2-}$ are heavily affected by both mucin and BSA on all tested electrodes, clearly in agreement with the Pt microelectrode data in Figure 4.1b. Taking the BDD electrode first in the control solution. The CV is as expected showing a well-defined peak shaped CV of ΔE_p = 65 mV corresponding to reduction of (IrCl$_6$)$^{2-}$ to (IrCl$_6$)$^{3-}$ and subsequent oxidation. Then similar to the response using Pt microelectrode in Figure 4.1b, in the presence of mucin or BSA, the current starts

positive indicating the presence of the reduced form $IrCl_6^{3-}$ at a sizeable concentration. It is also interesting to note the current drops to zero in the region where reduction of $(IrCl_6)^{2-}$ is expected. This general behaviour is also seen on the sp^2-BDD and GC electrodes. Interestingly, in the presence of mucin, on the two sp^2-carbon based electrodes (Figure 4.4a (ii) sp^2-BDD and (iii) GC) a shoulder is observed in the first scan of the oxidation peak of $IrCl_6^{3-/2-}$ that could indicate two sites for electron transfer, which diminishes in prominence with repeated scans.

Next, we consider the behaviour of all three electrodes in the 5% BSA solution (Figure 4.4b). A similar result is seen as for the mucin, in that when starting the scan in the oxidative window an oxidative current pass, suggesting BSA generation of $(IrCl_6)^{3-}$. The larger oxidative currents at the start of the scan and reduced reductive currents as the potential is scanned more negative, suggests BSA is more effective than mucin at this reductive turnover. The wave shape is also more sigmoidal, as found with systems which have increased flux,[51] especially on BDD and GC. Due to the oxidative peak being less defined and reaching a plateau, it is more difficult to extract ΔE_p. We note, the OCP has shifted from +0.76 V for $IrCl_6^{2-}$ in 0.1 M KCl to ca. +0.30 V in the presence of mucin and BSA. In comparison the OCP of the control and different protein $Ru(NH_3)_6^{3+}$ solutions remained around +0.2 V.

As $IrCl_6^{2-}$ is being reduced to $IrCl_6^{3-}$ prior to applying a potential, the concentration of $IrCl_6^{2-}$ present in solution has reduced. Therefore, the change in j_{pa} for 1 mM $IrCl_6^{3-}$ oxidation is tracked over time as shown in Figure 4.5, using (a) BDD, (b) sp^2-BDD, and (c) GC electrodes, with no protein added (black, squares), 0.5% w/v mucin (red, circles), or 5% w/v BSA (blue, triangles). The peak current is reported in the absence of proteins. However, in the presence of BSA and mucin over the measurement time (910 s), the CV shape changes from peak to steady state, in this case the steady state current is reported.
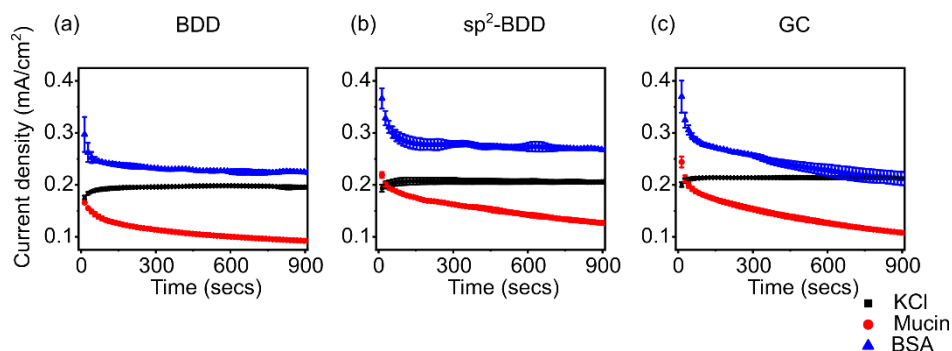
Figure 4.5. The anodic current density for the oxidation of 1 mM $IrCl_6^{3-/2-}$ in 0.1 M KCl, with 0.5% (w/v) mucin (red circle) or 5% (w/v) BSA (blue triangle), performed using (a) BDD, (b) sp^2-BDD, and (c) GC electrodes in aerated solutions, at 100 mV/s for 910 s (average of n = 3, with standard deviation error bars).

In the absence of protein, the oxidative currents recorded on BDD was 0.18 mA/cm^2, sp^2-BDD was 0.19 mA/cm^2, and GC was 0.20 mA/cm^2. The currents stabilise to 0.20 mA/cm^2 on BDD and sp^2-BDD, and 0.21 mA/cm^2 on GC in 910 s. The anodic currents decreased with consecutive scans in mucin with all electrodes. The first scan exhibits 0.17, 0.22, and 0.24 mA/cm^2 for BDD, sp^2-BDD, and GC respectively. The current continues to decrease and does not stabilise within the measurement time of 910 s, and the current reaches 0.09, 0.13, and 0.12 mA/cm^2 for BDD, sp^2-BDD, and GC respectively by 910 s.

In BSA, the j_{pa} of the first scan for BDD was 0.30 mA/cm^2, and for both the sp^2-BDD and GC electrodes, the current was 0.37 mA/cm^2. Similar to mucin, the current decreases and almost stabilises by the end of the measurement duration (910 s) for BDD (0.22 mA/cm^2) and sp^2-BDD (0.27 mA/cm^2) but does not stabilise for GC (0.21 mA/cm^2). This suggests that BSA has a greater fouling effect on GC than the other carbon-based electrodes, and the fouling observed with mucin seems similar on all three electrodes.

4.3.2. Non-Faradaic: Effect of biological matrices on the double layer capacitance

As one EIS spectrum takes ca. 180 s to record, within that timeframe we show there are already significant changes in the CV behaviour in the presence

106

of BSA or mucin (Figure 4.2 and 4.3) from that in the control solution. Due to the length of the EIS measurement, it is therefore not possible to accurately assess what happens during the initial stages of electrode contact with the protein containing solution. Furthermore, in an EIS experiment the measurement is only made at only one potential and it is well known that protein adsorption can be affected by the applied potential (and charge) on the electrode surface.[52–55] Therefore, experiments were undertaken where the change in C_{dl} was recorded over three different potential ranges, 0.0 V ± 0.1 V, +0.4 V ± 0.1 V and -0.4 V ± 0.1 V vs SCE, using (a) BDD, (b) sp^2-BDD, and (c) GC electrodes, Figure 4.6. C_{dl} was measured using the box CV method[56] in three different solutions, control 0.1 M KCl, 0.5% mucin in 0.1 M KCl and 5% BSA in 0.1 M KCl. C_{dl} is calculated using Equation 4.2:

$$C_{dl} = \frac{i_{av}}{vA}$$

Equation 4.2

where i_{av} is the average non-Faradaic current magnitude measured at the defined potential from each box CV from the forward and reverse sweep, v is the scan rate (50 mV/s) and A is the area of the electrode. The geometric area was assumed for all three electrodes. For BDD (Figure 4.6a) in 0.1 M KCl, the box CV starts distorting at potentials below -0.4 V vs SCE. Interestingly, deaerating the solution did not show any improvement, indicating other processes must be contributing even after degassing. Figure 4.6b, for sp^2-BDD, shows non-Faradaic regions at all potentials for capacitance analysis. The sp^2-BDD surface contains surface integrated quinone terminations, which are known to be pH sensitive as shown in Chapter 3.[34,57,58] The pH of 0.1 M KCl solution can vary from pH 6.00 to 6.95 (as the pH of unbuffered solutions can be affect by the amount of dissolved CO_2 present), hence the quinone pH response can be seen in the CVs for 0.0 V and +0.4 V vs SCE. For GC (Figure 4.6c) it was difficult to find a purely non-Faradaic (box-shaped) response in all potential regions investigated. However, the CV responses were still analysed to see if they could provide a qualitative assessment of the change in C_{dl}, from the protein-free solution to solutions containing different proteins.
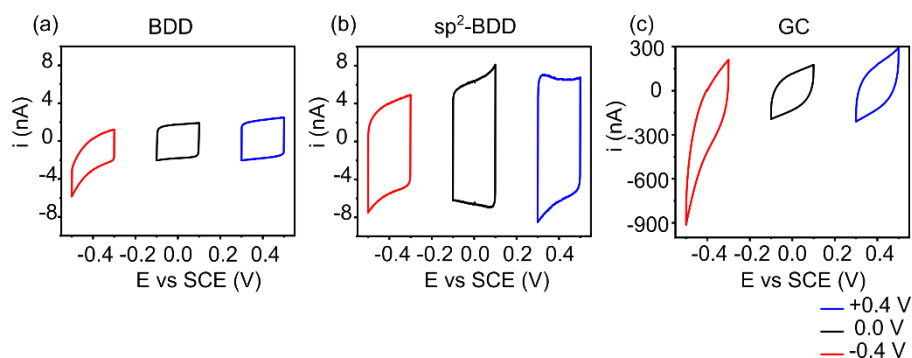
Figure 4.6. Box CVs for measuring the capacitance at different potential on (a) BDD (aerated), (b) sp^2-BDD (deaerated), and (c) GC electrodes (deaerated) shown in 0.1 M KCl.

Figure 4.7 shows the mean change in C_{dl} (ΔC_{dl}), which is the difference from the mean value measured in the control solution (0.1 M KCl = 5.14 ± 0.04, 5.17 ± 0.34, and 4.40 ± 0.06 µF/cm² for potentials +0.4, 0.0, and -0.4 V *vs* SCE respectively) to the mean value measured in the presence of protein. The C_{dl} values are extracted from the box CVs recorded over 904 s using a 1 mm BDD electrode at (a) +0.4 V, (b) 0 V, and (c) -0.4 V *vs* SCE in the presence of mucin (red circles) or BSA (blue triangles), in 0.1 M KCl at 50 mV/s. As each CV takes 8 s to record, there are therefore 112 data points. Each measurement is an average of three repeats, with standard deviation error bars.

Figure 4.7. BDD capacitance measured using CV at three potentials, (a) +0.4, (b) 0 and (c) -0.4 V (± 0.1 V) in the presence of two different fouling agents, 0.5% mucin (red circles) or 5% BSA (blue triangles), at 50 mV/s (average of n = 3, with standard deviation error bars).

In the presence of both 0.5% mucin and 5% BSA at +0.4 V and 0 V *vs* SCE the capacitance is always lower than the control measurement, with respect to time. However, within this there are variations, with the mucin continuing to decrease, whilst the BSA decreases then increases. In contrast, at -0.4 V *vs* SCE, whilst mucin causes a decrease in capacitance with time, with respect to the control, the BSA causes a slight increase in capacitance with time.

For both BSA and mucin, the greatest ΔC_{dl} is observed at the applied potential of +0.4 V *vs* SCE, a change of -0.59 ± 0.004 (at 128 s) and -0.68 ± 0.11 $\mu F/cm^2$ (at 904 s) respectively. Although for BSA by 904 s, the ΔC_{dl} increases to -0.48 ± 0.04 $\mu F/cm^2$. A similar response is observed at 0 V *vs* SCE where, the ΔC_{dl} reaches a maximum negative change at 264 s (-0.58 ± 0.10 $\mu F/cm^2$), then increases to -0.19 ± 0.13 $\mu F/cm^2$, reaching close to the control value in BSA. At 0 V *vs* SCE, the ΔC_{dl} for mucin stabilises by 904 s to -0.56 ± 0.19 $\mu F/cm^2$. This could suggest that BSA initially accumulates at the electrode surface, but then over time desorbs and moves away from the electrode surface resulting in the capacitance returning to a value close to that of the clean surface. Finally, at -0.4 V *vs* SCE, the electrode capacitance in the presence of mucin stabilises at -0.29 ± 0.01 $\mu F/cm^2$, with the smallest ΔC_{dl} observed. However, in the presence of BSA, the ΔC_{dl} starts close to the control (-0.001 ± 0.16 $\mu F/cm^2$ at 16 s) and increases to 0.30 ± 0.12 $\mu F/cm^2$ by 904 s. The reason for the increase in ΔC_{dl} is currently unclear and requires further exploring.

The addition of 0.5% mucin and 5% BSA decreased the pH of 0.1 M KCl solution from pH 6.20 to pH 3.89 and 6.00 respectively. As the pH is above the p*I* for both mucin and BSA,[49,50] the overall negatively charged proteins are likely to be electrostatically attracted to the more positively charged electrode surfaces (at +0.4 V *vs* SCE). This accounts for the greatest negative ΔC_{dl} observed. When proteins adsorb at the BDD-solution interface, whilst they can partially compensate the charge on the electrode surface, they are significantly bigger than simple (hydrated) ions e.g., K^+, Cl^-, and so will be of lower effective charge density. To contextualise, BSA is a small globular protein of size ~66 kDa. Atomic force microscopy revealed the native form if BSA has an equal-sided triangle structure with a side length of 9.2 nm, and the extended form has a length of 25

nm.[59,60] Mucin is a larger glycoprotein of size 0.5 to 20 MDa (depending on the length of the oligosaccharide chain) and transmission electron microscopy has revealed long fibres of ~400 nm in length.[28,61]

Figure 4.8 illustrates how the electrochemical double layer is modified in the presence of proteins. In the absence of proteins, the charge at the electrode surface is efficiently compensated by the counterions in solution, in this case K^+ and Cl^-. However, in the presence of proteins, the charge at the electrode surface is likely to be less efficiently compensated, therefore, the thickness of the double layer increases, which causes the capacitance to decrease.[55,62]
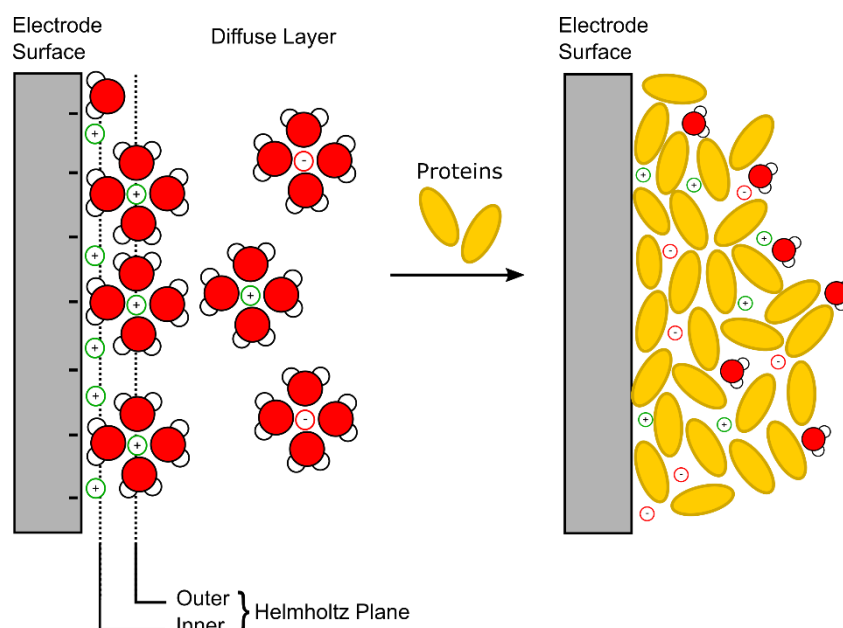
Figure 4.8. Illustration of the electrochemical double layer in the (left) absence and (right) presence of proteins, with red and white circles representing the water molecules, and yellow representing protein molecules.

Further to the charge at the electrode surface, the electrode surface chemistry (hydrophobicity) and roughness can also have an effect on how proteins interact and adsorb on the surface. For example, it was shown increasing the hydrophobicity (by introducing methoxy groups) on a GC electrode surface increased BSA adsorption.[63] Mucin is known to have a hydrophobic backbone and a hydrophilic oligosaccharide side chain,[64] therefore depending on the surface chemistry, it will reorganise itself to interact most appropriately with the surface.

The O-terminated BDD surface has been reported to be hydrophilic and smooth (RMS = 10 nm),[65,66] therefore, the changing ΔC_{dl} are likely to be predominantly due to the polarisation of the electrode surface. The exact charge of the electrode surface is dependent on the applied potential relative to the potential of zero charge (E_{pzc}), which for polycrystalline material such as BDD is challenging to measure. Interestingly, Wang *et al.* very recently reported a method for extracting out the E_{pzc} of the individual crystal grains associated with polycrystalline Pt using scanning electrochemical cell microscopy.[67] However, this method has yet to be applied to the individual crystal grains of polycrystalline BDD. We note that the open circuit potential in the control solution is 0.15 V *vs* SCE and, in the protein, containing solutions BSA and mucin OCP, it is 0.1 – 0.2 V *vs* SCE.

Figure 4.9 shows the mean ΔC_{dl} from control (0.1 M KCl = 16.5 ± 0.21, 16.5 ± 0.34, and 12.7 ± 0.53 µF/cm^2 for potentials +0.4, 0.0, and -0.4 V *vs* SCE respectively) to the presence of protein using a 1 mm diameter sp^2-BDD electrode at: (a) +0.4 V, (b) 0.0 V and (c) -0.4 V *vs* SCE, in the presence of mucin (red circles) or BSA (blue triangles) in 0.1 M KCl at 50 mV/s. Each measurement is an average of three repeats, with standard deviation error bars.
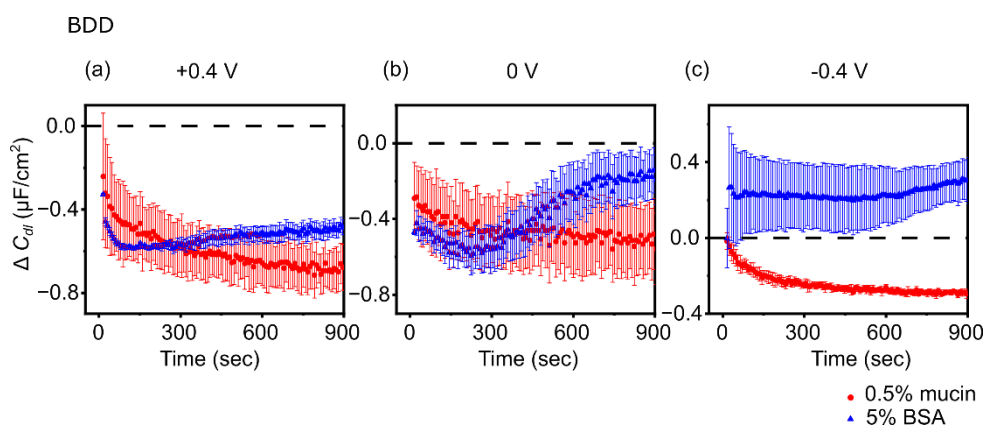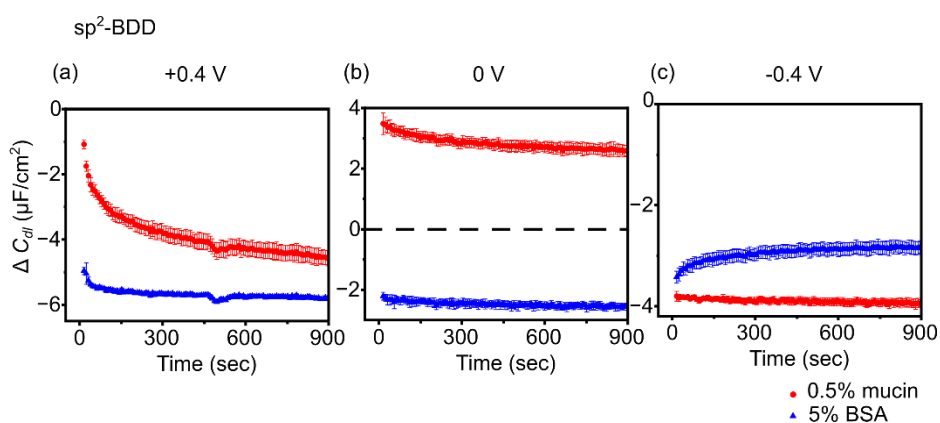

Figure 4.9. sp^2-BDD capacitance measured using CV at three potentials, (a) +0.4, (b) 0 and (c) -0.4 V (± 0.1 V) in the presence of two different fouling agents, 0.5% mucin (red circles) or 5% BSA (blue triangles), at 50 mV/s (average of n = 3, with standard deviation error bars).

Immediately noticeable compared to BDD is the fact that all the ΔC_{dl} values are now much bigger. However, similar to BDD is the fact the greatest ΔC_{dl} values for both mucin and BSA are observed at the applied potential of +0.4 V *vs* SCE at 904 s, giving -4.57 ± 0.22 and -5.81 ± 0.03 µF/cm², respectively. BSA also results in a negative value of ΔC_{dl} at 0 V and -0.4 V *vs* SCE (-2.53 ± 0.12 and -2.82 ± 0.14 µF/cm² respectively at 904 s). Likewise, mucin reduces the capacitance measured at -0.4 V *vs* SCE compared to the control (ΔC_{dl} -3.93 ± 0.07 µF/cm² at 904 s). However, interestingly for mucin, ΔC_{dl} measured at 0 V *vs* SCE has increased compared to the control and is now positive at +3.48 ± 0.36 µF/cm² (t = 16 s), reducing to +2.61 ± 0.17 µF/cm² at t = 904 s. This increase suggests mucin is now interacting differently with the sp² surface, compared to the BDD. Nevertheless, the change is still indicating that mucin is clearly affecting the electrode performance.

Overall, the data indicates that the sp²-BDD seems much more affected by proteins than BDD, as the difference in the mean ΔC_{dl} for sp²-BDD is greater. One possibility for this, could be due to the increase in the roughness of the sp²-BDD surface of RMS = 460 nm compared to 10 nm for BDD,[66] which provides more anchoring points for proteins to attach to compared to the smoother BDD surface.

Figure 4.10 shows the mean ΔC_{dl} from control (0.1 M KCl = 42.7 ± 1.05, 39.4 ± 3.69, and 46.4 ± 4.06 µF/cm² for potentials +0.4, 0, and -0.4 V *vs* SCE respectively) in the presence of protein, using a 3 mm diameter GC electrode at: (a) +0.4 V, (b) 0.0 V and (c) -0.4 V *vs* SCE, in the presence of mucin (red circles) or BSA (blue triangles) in 0.1 M KCl at 50 mV/s. Compared to BDD and sp²-BDD, the GC box CVs were the most distorted at all three potential ranges, therefore, the best way to interpret the data is only qualitatively, as there are clearly other processes interfering with the CV response (even in deaerated conditions).
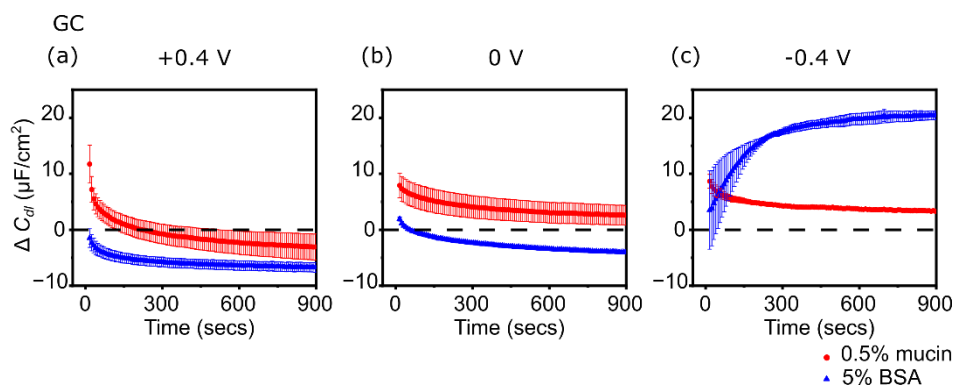
Figure 4.10. GC capacitance measured using CV at three potentials, (a) +0.4, (b) 0 and (c) -0.4 V (± 0.1 V) in the presence of two different fouling agents, 0.5% mucin (red circles) and 5% BSA (blue triangles), at 50 mV/s (average of n = 3, with standard deviation error bars).

Starting with mucin, at all three potentials, the change in capacitance decreases over time, at +0.4 V *vs* SCE change reaches below the control value and at 0.0 V and -0.4 V *vs* SCE, the ΔC_{dl} stabilises above the control value. A similar behaviour can be observed with BSA at +0.4 and 0.0 V *vs* SCE with ΔC_{dl} stabilising below control, however at -0.4 V *vs* SCE, the ΔC_{dl} increases over time. Interferometry showed that the average surface roughness of the GC electrode is RMS = 37 ± 8.6 nm, which is slightly rougher than the BDD electrode surface.

Thus, again the presence of proteins has had a significant effect on the capacitance of the electrode. However, due to the distortion of the shape of the CV and the difficulty in accurately determining a non-Faradaic region for GC, these changes should only be viewed qualitatively.

4.3.3. Effect of protein adsorption on the electrodeposition of silver

Direct imaging of the protein film on the electrode surface using FE-SEM proved to be difficult, due to the insulating nature of the proteins. Therefore, silver metal was electrodeposited, as an indirect method for providing information on protein adsorption on the surface. Here we investigate the Ag deposition CV response, Ag deposition pattern, and size of Ag particles as a means of providing an insight into protein adsorption on the electrode surface. A similar

approach has been previously used to study the film formation from serotonin electrochemical oxidation on BDD,[68] and to investigate β-casein protein adsorption on gold surfaces.[69]

Protein adsorption was allowed to take place by holding the electrode at either +/-0.4 V *vs* SCE for 900 s in 0.5% mucin or 5% BSA (both with 0.1 M KCl supporting electrolyte). This also allows the possibility to study the effect of applied potential on protein film formation. The electrode was then very gently rinsed prior to placing in a deaerated solution containing 1 mM $AgNO_3$ in 1 M KNO_3. Silver electrodeposition was also performed on a clean polished BDD electrode for comparison. The CV for Ag electrodeposition on the bare BDD electrode is shown in Figure 4.11a and b (black line). Here the potential was scanned from 0.4 to -0.8 V *vs* Ag|AgCl, to induce electrodeposition (for clarity data from +0.40 V to -0.45 V *vs* Ag|AgCl is shown) and then scanned back (-0.8 V to +0.8 V *vs* Ag|AgCl) to promote Ag dissolution from the electrode surface. The characteristic peak potential for Ag electrodeposition occurs at +0.17 V *vs* Ag|AgCl on the BDD electrode surface, whilst that for stripping occurs at +0.46 V *vs* Ag|AgCl. The CV response for 1 mM $AgNO_3$, after the electrode had been held at -0.4 V (red line) or +0.4 V (blue line) *vs* SCE for 900 s is shown in Figure 4.11 for (a) 0.5% mucin and (b) 5% BSA.
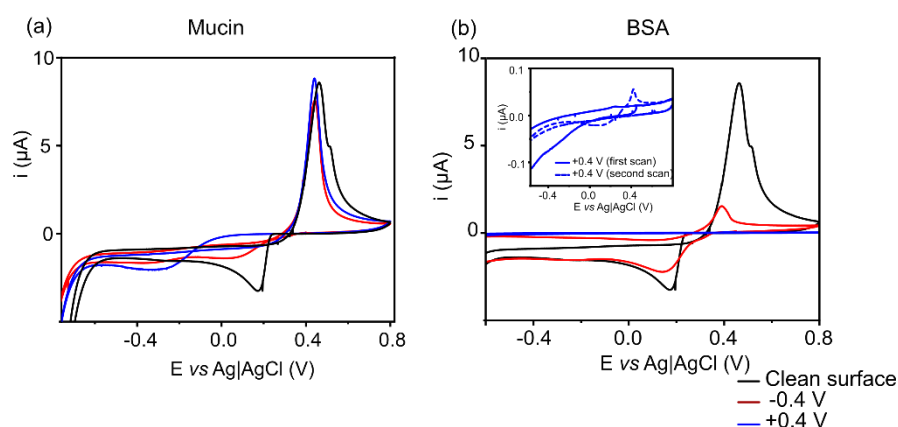
Figure 4.11. CVs for the silver electrodeposition (first scan unless stated otherwise) on clean BDD electrode (black), after holding at +0.4 V (blue) or -0.4 V *vs* SCE (red) in (a) mucin or (b) BSA for 900 s (inset show enlarged CV at deposition potentials, scan 1 = solid, scan 2 = dashed). Ag electrodeposition conducted under Ar.

For 0.5% mucin, after both applied holding potentials, the peak potentials for Ag electrodeposition have shifted negatively to +0.06 V and -0.33 V *vs* Ag|AgCl for -0.4 V and +0.4 *vs* SCE respectively. For BSA, after holding at -0.4 V *vs* SCE, the peak potential has also shifted negatively to 0.14 V *vs* Ag|AgCl (from +0.17 V *vs* Ag|AgCl). However, the CV response after holding at +0.4 V *vs* SCE shown in the insert in Figure 4.11b, shows no peak can be observed on the first scan but can be observed in the second scan at 0.08 V *vs* Ag|AgCl. The negative shift in potential, for both applied holding potentials during placement in the protein solutions (mucin and BSA), indicates a larger overpotential required for Ag electrodeposition, suggesting a resistive contribution. The potential needed after holding the electrode at +0.4 V *vs* SCE in both, mucin and BSA, is more negative than that after holding at -0.4 V *vs* SCE, indicating more protein adsorption which hinders electron transfer from the electrode to Ag^+ in solution. This is expected as shown above (from the C_{dl} data) where a more positive applied potential at the electrode surface appears to be promoting protein adsorption.

For BSA after holding at +0.4 V *vs* SCE, protein adsorption is sufficient enough to hinder electron transfer such that the first scan shows no deposition peak. The second scan only presents a small deposition peak of very low current. This suggests that protein adsorption is a reversible process, and over time some of the adsorbed protein molecules have diffused away from the electrode surface into solution leaving more regions available for Ag electrodeposition.

The effect of protein adsorption on Ag electrodeposition can be further observed through FE-SEM imaging, shown in Figure 4.12(a) a clean BDD surface, and Ag deposition on (b) clean BDD electrode, (c) after holding at +0.4 V *vs* SCE and (d) after holding at -0.4 V *vs* SCE in 0.5 % mucin for 900 s and performing Ag electrodeposition. A potential of -0.2 V *vs* Ag|AgCl for 60 s was chosen for Ag electrodeposition, as maintaining the same potential and electrodeposition conditions on all electrodes, allows for the comparison of the sluggish deposition kinetics in the presence of protein on the electrode surface.

Figure 4.12a shows the In-Lens FE-SEM image of a polished, annealed surface of a polycrystalline BDD electrode, which enables visualisation of grains

with different boron dopant concentrations (the darker grains contain higher boron dopant levels).[36] Figure 4.12b shows the secondary lens FE-SEM image for Ag electrodeposition on the clean BDD surface, there appears to be little grain dependence on the Ag deposition pattern (all images displayed here are representative of the whole surface). The length of time (60 s) and potential applied (-0.2 V *vs* Ag|AgCl) allows for the nucleation and growth of micron sized dendritic Ag particles on the BDD electrode. Previously, similar deposition conditions have shown that Ag electrodeposition is grain dependent on polycrystalline BDD,[68,70] however, here the surfaces used were unannealed. Annealing the surface is known to roughen the surface from 1.11 ± 0.07 nm to 41 ± 1 nm RMS.[36] Thus we argue the increased roughness is providing more regions for Ag to anchor and reducing any grain dependence on the deposition.
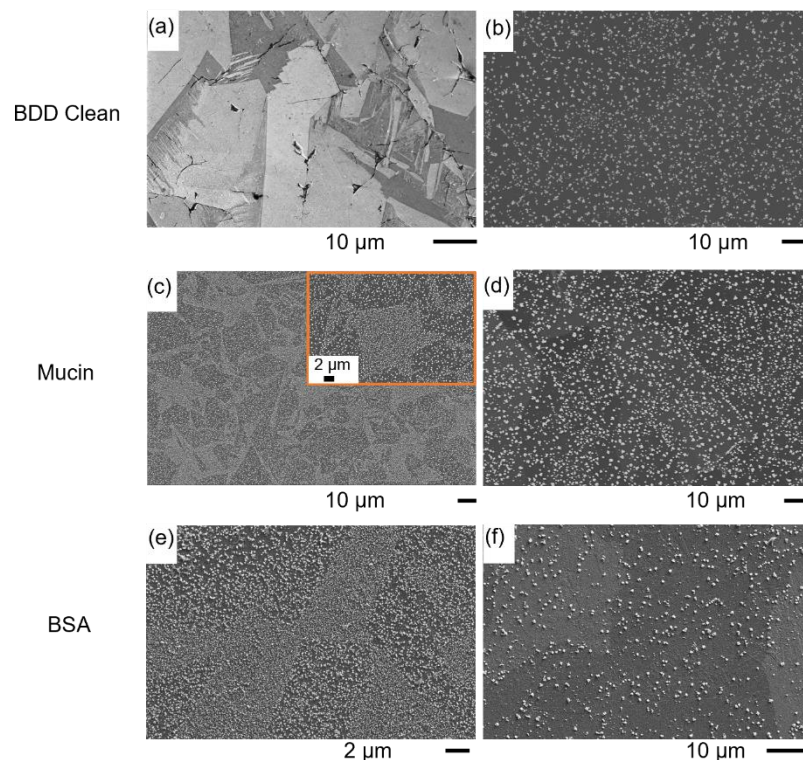
Figure 4.12. FE-SEM (a) In-Lens image of a polished annealed BDD surface, and (b-f) secondary lens images showing electrodeposition in 1 mM AgNO$_3$ in 1 M KNO$_3$ by applying a potential of -0.2 V vs. Ag|AgCl for 60 s on a (b) BDD electrode. Silver deposition after holding at (c) +0.4 V, and (d) -0.4 V *vs* SCE in mucin and (e) +0.4 V, and (f) -0.4 V *vs* SCE in BSA for 900 s each. Ag electrodeposition conducted under Ar.

Starting with mucin, Figure 4.12c shows Ag electrodeposited on BDD after the electrode had been held at +0.4 V *vs* SCE for 900 s in 0.5% mucin solution. The deposition varies between regions on the electrode surface, indicating a grain dependence on the deposition. The grains with higher boron doping shows densely deposited particles ranging from 70 to 300 nm, whereas the grains with less boron dopant density, shows Ag particles more spread out with sizes ranging from 120 – 600 nm. Compared to Ag deposition on the clean BDD surface, there is an increased grain dependence and the particles sizes have reduced. This behaviour highlights the presence of a "semi-permeable" layer of mucin on the surface of the electrode, which is acting to retard electron transfer. Thus, compared to the bare BDD case, the overpotential for Ag deposition is

reduced leading to the local resistivity of the differently doped boron grains now playing a more prominent role in controlling the electrodeposition structures formed.

After the -0.4 V *vs* SCE treatment in mucin solution, the Ag electrodeposition performed (Figure 4.12d) shows micron sized (0.6 – 2 µm) Ag deposits across the electrode surface, with accumulation on the grain boundaries, due to the rougher regions promoting easier anchoring for Ag particles. This is similar to the deposition observed on the clean BDD surface, suggesting there is less mucin adsorbed on the surface that could be influencing silver electrodeposition.

For BSA, the +0.4 V *vs* SCE treatment (Figure 4.12e) shows that Ag deposition is grain dependent. The grains with higher boron density shows densely packed Ag particles with sizes ranging from 20 – 160 nm, and less boron dense grains shows Ag particles ranging from 30 – 250 nm that are more spread out. The higher density of Ag particles, and smaller particles sizes compared to the +0.4 V *vs* SCE treatment in mucin, suggests that BSA has a greater effect on Ag electrodeposition. This is further supported by Figure 4.11, where Ag electrodeposition after +0.4 V *vs* SCE treatment was more hindered by BSA than mucin. After the electrode had been held at -0.4 V *vs* SCE for 900 s, the Ag deposition is very different (Figure 4.12f), with no grain dependence, and larger micron sized deposits, but a lower particle density compared to Ag on clean BDD, or after -0.4 V *vs* SCE treatment in mucin. This could mean there is some BSA on the surface that is guiding the Ag deposition.

From the silver electrodeposition results, Figure 4.13 shows a schematic illustrating the role of protein adsorption versus Ag deposition during the different deposition conditions on BDD. When the surface is polarised to +0.4 V *vs* SCE, the results suggest that an electrically insulating, semi-permeable (to ions) layer of protein is covering the electrode surface. This acts to kinetically retard Ag electrodeposition, with respect to deposition on a bare BDD surface, such that kinetic differences in the grains are revealed *via* the Ag electrodeposition patterns, at the stated electrodeposition potential. However, at -0.4 V *vs* SCE, it is likely the protein layer does not cover the surface fully, or it desorbs with time, leaving regions free for Ag+ access (independent of boron

dopant density), resulting in Ag deposition across the surface with no grain dependence.
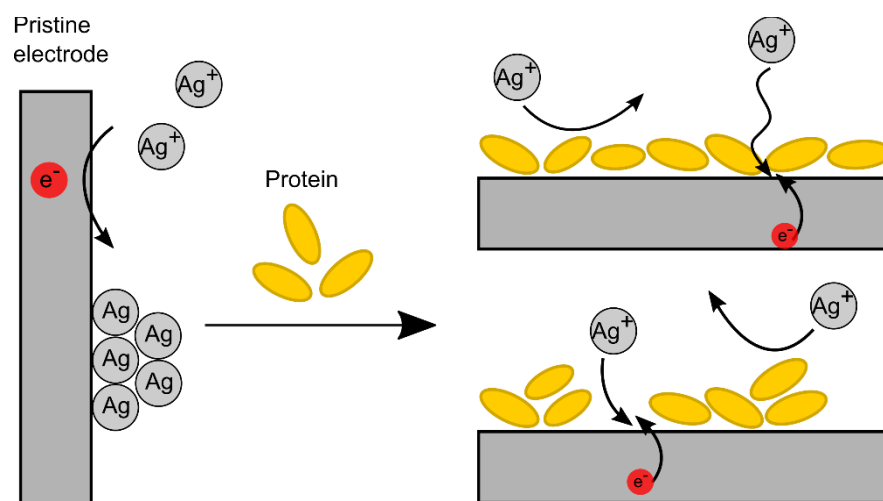
Figure 4.13. Schematic to illustrate our hypothesis on how the Ag electrodeposition is affected from protein adsorption on electrode surface.

Furthermore, as proteins have regions of positive and negative charge, the Ag ions can also electrostatically attract towards the negatively charged regions on the protein surface. Additionally, BSA and mucin are known reducing agents used in the synthesis of Ag nanoparticles,[44,71] therefore, there could also be the presence of Ag nanoparticles deposited around the proteins.

A similar experiment was carried out using the sp^2-BDD electrode (Figure 4.14). CVs were conducted in a deaerated solution of 1 mM AgNO$_3$ in 1 M KNO$_3$ on a (black line) BDD surface, after holding at (red line) -0.4 V *vs* SCE and (blue line) +0.4 V *vs* SCE in (a) 0.5% mucin and (b) 5% BSA solutions. The first CV scan on the bare surface (Figure 4.14a and b, black solid line) shows the characteristic peak potential for Ag electrodeposition at +0.32 V *vs* Ag|AgCl compared to +0.17 V *vs* Ag|AgCl on the BDD surface (Figure 4.11). This indicates the greater ease of Ag electrodeposition on the rougher sp^2-BDD surface (RMS 460 nm)[66] compared to BDD (RMS 10 nm), providing more attachment sites for anchoring Ag NPs and encouraging growth into larger particles.
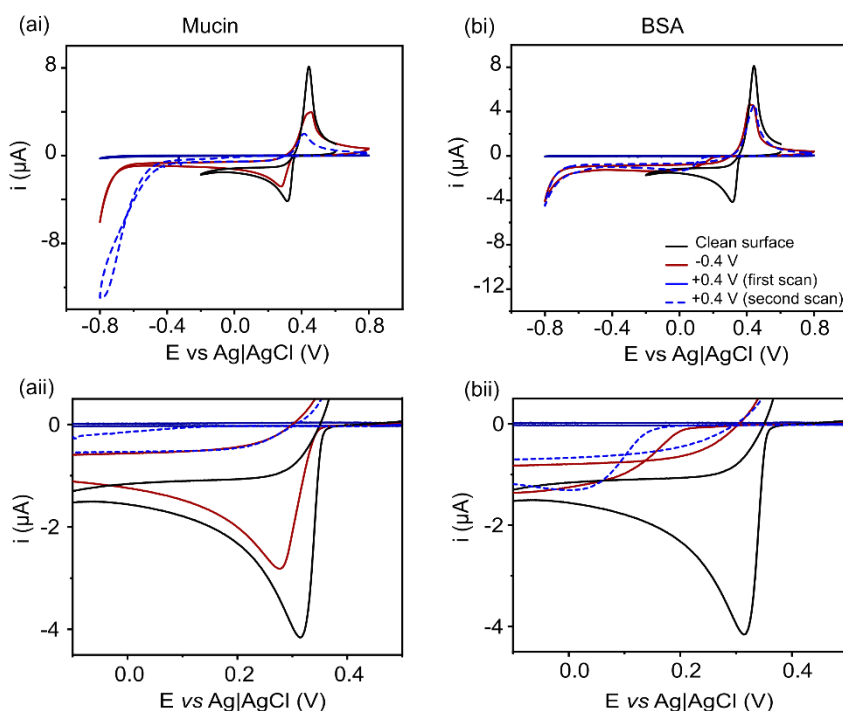
Figure 4.14. CVs for the silver electrodeposition (first scan unless stated otherwise) on clean sp²-BDD electrode (black), after holding at +0.4 V (blue, scan 1 = solid and scan 2 = dashed) or -0.4 V (red) in (ai) mucin or (bi) BSA for 900 s, (aii) and (bii) show enlarged CV at deposition potentials for mucin and BSA respectively. Ag electrodeposition conducted under Ar.

For mucin and BSA, Ag electrodeposition is greatly hindered after holding at +0.4 V *vs* SCE in the protein solutions, as the first scan does not show any notable deposition currents in the scan window. However, by the second scan, there is the appearance of a very low current deposition feature at +0.17 V *vs* Ag|AgCl and +0.01 V *vs* Ag|AgCl for mucin and BSA respectively. Furthermore, for both mucin and BSA in the second scan there is also the appearance of a stripping peak at +0.4 V *vs* Ag|AgCl suggesting that there has been some Ag deposited on the surface which is being removed at the more positive potential.

After holding at -0.4 V *vs* SCE in mucin solution for 900 s, the subsequent Ag deposition CV (Figure 4.14a, red line) shows the characteristic Ag peak has shifted very slightly from +0.32 V *vs* Ag|AgCl on the clean surface to +0.28 V *vs* Ag|AgCl, with a concurrent lower current response. Figure 4.14b (red line) shows the response of Ag deposition after holding at -0.4 V *vs* SCE in BSA for 900 s, the

peak current has greatly decreased from that recorded on the clean surface, and peak shifted to -0.09 V *vs* Ag|AgCl. Thus, even at the more negative applied potential on this surface, there is evidence of protein adsorption on the electrode surface that has affected Ag electrodeposition.

FE-SEM imaging of the Ag electrodeposition on protein modified sp^2-BDD electrodes can be seen in Figure 4.15 (a) a clean sp^2 – BDD surface, and Ag deposition on (b) clean sp^2 – BDD electrode, (c) after holding at +0.4 V *vs* SCE and (d) after holding at -0.4 V *vs* SCE in mucin and (e) +0.4 V *vs* SCE and (f) -0.4 V *vs* SCE in BSA for 900 s and subsequently electrodepositing Ag. A potential of -0.2 V *vs* Ag|AgCl for 60 s was chosen for Ag electrodeposition, to allow direct comparison to BDD by maintaining the same conditions.
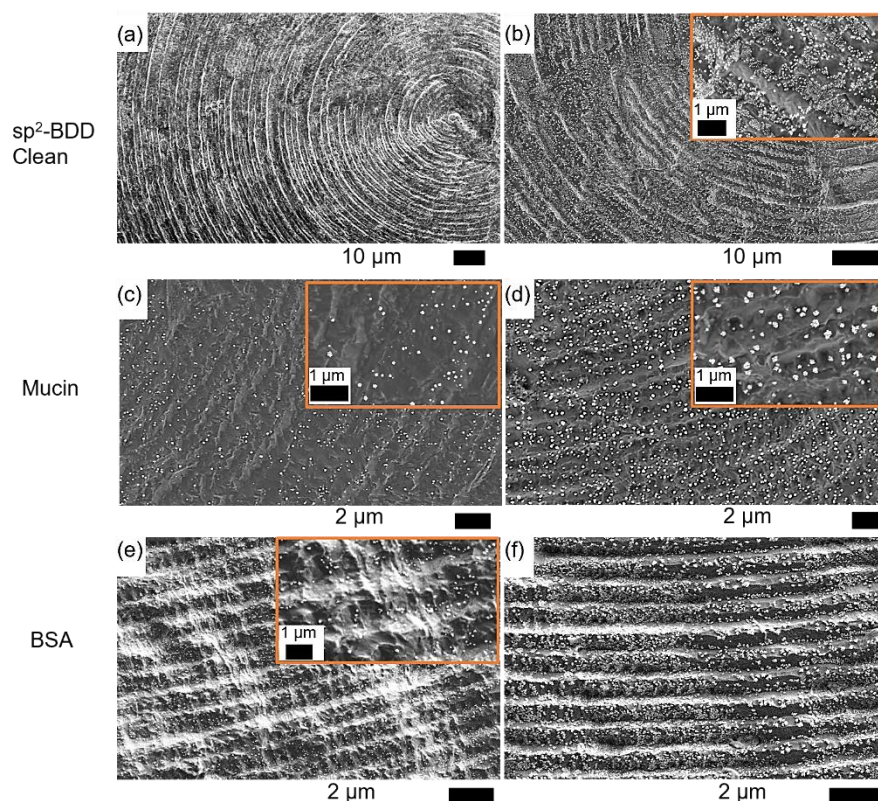
Figure 4.15. FE-SEM image In-Lens of (a) polished sp^2-BDD surface, and secondary lens images showing electrodeposition in 1 mM AgNO$_3$ in 1 M KNO$_3$ by applying a potential of -0.2 V vs. Ag|AgCl for 60 s on a (b) sp^2-BDD electrode. Silver deposition after holding at (c) +0.4 V, and (d) -0.4 V in mucin and (e) +0.4 V, and (f) -0.4 V in BSA for 900 s each. Electrodeposition conducted under Ar.

Figure 4.15a, shows the sp^2-BDD surface, where the laser ablation patterns, used to convert the BDD surface to sp^2 carbon, can be seen clearly. Figure 4.15b is a secondary lens image of the electrode surface after Ag electrodeposition at -0.2 V *vs* Ag|AgCl for 60 s, with the inset showing the enlarged surface, where Ag is clearly present more in the grooves of the lasered surface than on top. There is a mixture of particle sizes from 20 to 300 nm.

Ag electrodeposition in the presence of mucin was more difficult to observe on sp^2-BDD than BDD, additionally, the presence of insulating protein residues on the surface created charging and focusing issues while imaging. For the +0.4 V *vs* SCE treatment, Figure 4.15c, shows a low density of Ag particles (~250 to 300 nm) across the surface. Whereas, for -0.4 V *vs* SCE treatment (Figure 4.15d), there is a higher density of Ag particles of ~500 nm in size, deposited. Similar to the response observed in BDD, the most hindered Ag deposition occurs after +0.4 V *vs* SCE treatment, which agrees that mucin, an overall negatively charged molecules (in the conditions used), is electrostatically attracted to the positively charged electrode surface.

Figure 4.15e shows the Ag deposition after holding at +0.4 V *vs* SCE in BSA solution. Similar to the +0.4 V *vs* SCE treatment in mucin, there are Ag particles present in the grooves of the lasered surface, ~150 to 250 nm in size. Compared to the deposition observed on the clean sp^2-BDD, the lower particle density implies a hinderance to Ag deposition. After -0.4 V *vs* SCE treatment in BSA, there is a mixture of Ag particles ranging from 100 – 500 nm in higher density decorated around the grooves with little regions free of Ag. For both BDD and sp^2-BDD electrodes, there is a clear potential dependence on protein film formation. The more positive potentials favour the formation of the protein layer that hinder Ag deposition kinetics observed in the CV response, which can be observed clearly in the corresponding FE-SEM images.

4.4. CONCLUSIONS

The presence of protein, mucin and BSA, was found to increase the viscosity of the solution, which consequently decreased the diffusion coefficient of Ru(NH$_3$)$_6$$^{3+}$. On the other hand, IrCl$_6$$^{2-}$ undergoes a chemical reduction by the proteins to IrCl$_6$$^{3-}$ prior to applying a potential.

Furthermore, the time-dependent fouling on three carbon-based electrodes: BDD, sp²-BDD, and GC were explored. Firstly, by tracking the electron transfer kinetics and peak currents in the absence and presence of mucin or BSA, in solutions containing $Ru(NH_3)_6{}^{3+}$ and $IrCl_6{}^{2-}$. It was clear that the presence of proteins caused a decrease in the peak reduction current of $Ru(NH_3)_6{}^{3+}$ for all three electrodes, and the electron transfer kinetics for BDD and sp2-BDD was more affected by proteins than GC. The oxidation current for $IrCl_6{}^{3-}$ reduced over time, the current response in the presence of mucin were similar for all electrodes, however, BSA had a greater effect on GC than BDD or sp²-BDD.

Secondly, the ΔC_{dl} of the electrodes were tracked over time, at three different potentials using CV. The presence of proteins had significant effect on the capacitance. However, especially for GC, it was difficult to find regions that were purely non-faradaic to conduct accurate C_{dl} measurements. Although CV method was appropriate for BDD and sp²-BDD, this may not be the ideal method for other materials.

Finally, Ag electrodeposition has been used an indirect method to understand protein adsorption patterns at positive and negative potentials on BDD and sp²-BDD electrodes, as a result of the particle size variation and grain dependence on deposition in the presence of proteins. At negative applied potentials (-0.4 V vs SCE), there was a presence of low density and large particle (few microns) Ag deposits, whereas at positive applied potential (+0.4 V vs SCE), there was a high density of smaller (few nanometres) Ag deposits. Clearly suggesting that along with other surface properties (hydrophilicity, roughness etc), the surface polarisation is extremely important for protein adsorption.

4.5. REFERENCES

1   B. L. Hanssen, S. Siraj and D. K. Y. Wong, *Rev. Anal. Chem.*, 2016, **35**, 1–28.

2   M. J. Russo, M. Han, P. E. Desroches, C. S. Manasa, J. Dennaoui, A. F. Quigley, R. M. I. Kapsa, S. E. Moulton, R. M. Guijt, G. W. Greene and S. M. Silva, *ACS Sensors*, 2021, **6**, 1482–1507.

3   C. Jiang, G. Wang, R. Hein, N. Liu, X. Luo and J. J. Davis, *Chem. Rev.*, 2020, **120**, 3852–3889.

4   R. A. Latour, *Colloids Surfaces B Biointerfaces*, 2020, **191**, 110992.

5   D. R. Schmidt, H. Waldeck and W. J. Kao, *Protein Adsorption to Biomaterials*, Springer, 2009.

6   S. A. Bhakta, E. Evans, T. E. Benavidez and C. D. Garcia, *Anal. Chim. Acta*, 2015, **872**, 7–25.

7   P. Joshi, R. Mishra and R. J. Narayan, *Curr. Opin. Biomed. Eng.*, 2021, **18**, 100274.

8   K. E. Dunham and B. J. Venton, *Analyst*, 2020, **145**, 7437–7446.

9   M. E. Weese, R. A. Krevh, Y. Li, N. T. Alvarez and A. E. Ross, *ACS Sensors*, 2019, **4**, 1001–1007.

10   Y. Li, C. M. Fleischer and A. E. Ross, *Chem. Commun.*, 2020, **56**, 8023–8026.

11   R. Trouillon and D. O'Hare, *Electrochim. Acta*, 2010, **55**, 6586–6595.

12   E. Peltola, A. Aarva, S. Sainio, J. J. Heikkinen, N. Wester, V. Jokinen, J. Koskinen and T. Laurila, *Phys. Chem. Chem. Phys.*, 2020, **22**, 16630–16640.

13   P. E. Sharel, T. S. Miller, L. Meng, P. R. Unwin and J. V. Macpherson, *J. Electroanal. Chem.*, 2020, **872**, 114137.

14   B. Guo, J. Anzai and T. Osa, *Chem. Pharm. Bull*, 1996, **44**, 800–803.

15   S. J. Cobb and J. V. Macpherson, *Anal. Chem.*, 2019, **91**, 7935–7942.

16   A. R. Harris, P. Carter, R. Cowan and G. G. Wallace, *ChemElectroChem*, 2021, **8**, 1078–1090.

17   S. Omanovic and S. G. Roscoe, *Langmuir*, 1999, **15**, 8315–8321.

18   Y. Huang, A. Hara, C. Terashima, A. Fujishima and M. Takai, *Carbon N. Y.*, 2019, **152**, 354–362.

19   O. A. Sadik and M. C. Cheung, *Talanta*, 2001, **55**, 929–941.

20   M. Farcas, N. P. Cosman, D. K. Ting, S. G. Roscoe and S. Omanovic, *J. Electroanal. Chem.*, 2010, **649**, 206–218.

21   B. Beykal, M. Herzberg, Y. Oren and M. S. Mauter, *J. Colloid Interface Sci.*, 2015, **460**, 321–328.

22   C. Blaszykowski, S. Sheikh and M. Thompson, *Chem. Soc. Rev.*, 2012, **41**, 5599–5612.

23   T. Peters, *Adv. Clin. Chem.*, 1970, **13**, 37–111.

24   T. Peters, *Adv. Protein Chem.*, 1985, **37**, 161–245.

25   P. Ying, A. S. Viana, L. M. Abrantes and G. Jin, *J. Colloid Interface Sci.*, 2004, **279**, 95–99.

26   R. B. Brown, M. A. Hollingsworth and J. E. Schaffer, in *Encyclopedia of Biological Chemistry: Third Edition*, Elsevier, 2021, vol. 3, pp. 167–172.

27   R. B. Brown and M. A. Hollingsworth, *Encycl. Biol. Chem. Second Ed.*, 2013, 200–204.

28   R. Bansil and B. S. Turner, *Curr. Opin. Colloid Interface Sci.*, 2006, **11**, 164–170.

29   A. P. Corfield, *BBA - Gen. Subj.*, 2015, **1850**, 236–252.

30   A. Fagan-Murphy, F. Watt, K. A. Morgan and B. A. Patel, *J. Electroanal. Chem.*, 2012, **684**, 1–5.

31   T. Rajan, T. Read, A. Abdalla, B. Patel and J. Macpherson, *ACS Sensors*, 2020, **5**, 2858–2865.

32   G. Di Carlo, A. Trani, D. Zane, G. M. Ingo, M. Pasquali, A. Dell'Era and A. Curulli, *Electroanalysis*, 2014, **26**, 1409–1418.

33   T. L. Read, S. J. Cobb and J. V Macpherson, *ACS. Sens.*, 2019, **4**, 756–763.

34   Z. J. Ayres, A. J. Borrill, J. C. Newland, M. E. Newton and J. V Macpherson, *Anal. Chem.*, 2016, **88**, 974–980.

35   Y. Yi, G. Weinberg, M. Prenzel, M. Greiner, S. Heumann, S. Becker and R. Schlögl, *Catal. Today*, 2017, **295**, 32–40.

36   S. J. Cobb, F. H. J. Laidlaw, G. West, G. Wood, M. E. Newton, R. Beanland and J. V Macpherson, *Carbon N. Y.*, 2020, **167**, 1–10.

37   L. et al. Hutton, *Anal. Chem.*, 2013, **85**, 7230–7240.

38   L. Hutton, M. E. Newton, P. R. Unwin and J. V Macpherson, *Anal. Chem*, 2009, **81**, 1023–1032.

39   F. He, C. J. Liu, B. Eliasson and B. Xue, *Surf. Interface Anal.*, 2001, **32**, 106–109.

40   M. B. Joseph, E. Bitziou, T. L. Read, L. Meng, N. L. Palmer, T. P. Mollart, M. E. Newton and J. V. MacPherson, *Anal. Chem.*, 2014, **86**, 5238–5244.

41   C. Montella, *J. Electroanal. Chem.*, 2018, **808**, 348–361.

42   Y. Wang, C. Li and G. J. Pielak, *J. Am. Chem. Soc.*, 2010, **132**, 9392–9397.

43   Y. Wang, J. G. Limon-Petersen and R. G. Compton, *J. Electroanal. Chem.*, 2011, **652**, 13–17.

44   J. . Morales-Sánchez, J. Guajardo-Pacheco, M.-E. Noriega, Q. Cristina, M. E. Compeán-Jasso, J. González-Hernández and R. Facundo, *Mater. Sci. Appl.*,

2011, **02**, 578–581.

45   J. Perez-Vilar and R. L. Hill, *J. Biol. Chem.*, 1999, **274**, 31751–31754.

46   Z. Hong, B. Chasan, R. Bansil, B. S. Turner, K. R. Bhaskar and N. H. Afdhal, *Biomacromolecules*, 2005, **6**, 3458–3466.

47   R. S. Nicholson and I. Shain, *Anal. Chem.*, 1964, **36**, 1212.

48   S.-Y. Tan, R. A. Lazenby, K. Bano, J. Zhang, A. M. Bond, J. V Macpherson and P. R. Unwin, *Phys. Chem. Chem. Phys*, 2017, **8726**, 8726.

49   S. Lee, M. Mü, K. Rezwan, N. D. Spencer, M. Müller, K. Rezwan and N. D. Spencer, *Langmuir*, 2005, **21**, 8344–8353.

50   J. I. Anzai, B. Guo and T. Osa, *Bioelectrochemistry Bioenerg.*, 1996, **40**, 35–40.

51   A. J. Bard and L. R. Faulkner, *Electrochemical Methods Fundamentals and Applications*, John Wiley & Sons, 2001, vol. 677.

52   E. E. Htwe, Y. Nakama, Y. Yamamoto, H. Tanaka, H. Imanaka, N. Ishida and K. Imamura, *Colloids Surfaces B Biointerfaces*, 2018, **166**, 262–268.

53   T. E. Benavidez and C. D. Garcia, *Langmuir*, 2013, **29**, 14154–14162.

54   M. Rabe, D. Verdes and S. Seeger, *Adv. Colloid Interface Sci.*, 2011, **162**, 87–106.

55   S. E. Moulton, J. N. Barisci, A. Bath, R. Stella and G. G. Wallace, *Electrochim. Acta*, 2004, **49**, 4223–4230.

56   D. M. Morales and M. Risch, *JPhys Energy*, 2021, **3**, 034013.

57   M. Lu and R. G. Compton, *Analyst*, 2014, **139**, 4599–4605.

58   M. Lu and R. G. Compton, *Analyst*, 2014, **139**, 2397–2403.

59   B. Jachimska, K. Tokarczyk, M. Łapczyńska, A. Puciul-Malinowska and S. Zapotoczny, *Colloids Surfaces A Physicochem. Eng. Asp.*, 2016, **489**, 163–172.

60   B. Jachimska and A. Pajor, *Bioelectrochemistry*, 2012, **87**, 138–146.

61   I. Fiebrig, S. E. Harding, A. J. Rowe, S. C. Hyman and S. S. Davis, *Carbohydr. Polym.*, 1995, **28**, 239–244.

62   M. A. Macdonald and H. A. Andreas, *Electrochim. Acta*, 2014, **129**, 290–299.

63   A. J. Downard and A. D. Roddick, *Electroanalysis*, 1995, **7**, 376–378.

64   L. Shi, R. Ardehali, K. D. Caldwell and P. Valint, *Colloids Surfaces B*

Biointerfaces, 2000, **17**, 229–239.

65   L. J. Simcox, R. P. A. Pereira, E. M. H. Wellington and J. V. Macpherson, *ACS Appl. Mater. Interfaces*, 2019, **11**, 25024–25033.

66   J. J. Tully, Z. Zhang, I. M. Terrero Rodríguez, L. Butcher and J. V Macpherson, *Anal. Chem.*, 2022, **94**, 9856–9862.

67   Y. Wang, E. Gordon and H. Ren, *Anal. Chem.*, 2020, **92**, 2859–2865.

68   A. N. Patel, P. R. Unwin and J. V. MacPherson, *Phys. Chem. Chem. Phys.*, 2013, **15**, 18085–18092.

69   I. Bakos, Á. Vass, E. S. Muckley, I. N. Ivanov and Z. Keresztes, *Electrochem. commun.*, 2021, **124**, 106961.

70   A. L. Colley, C. G. Williams, U. D. H. Johansson, M. E. Newton, P. R. Unwin, N. R. Wilson and J. V. Macpherson, *Anal. Chem.*, 2006, **78**, 2539–2548.

71   N. Hendler, L. Fadeev, E. D. Mentovich, B. Belgorodsky, M. Gozin and S. Richter, *Chem. Commun.*, 2011, **47**, 7419–7421.

Chapter 5. ASSESSING BORON DOPED DIAMOND ELECTRODE UNDER FLOW FOR BIOMEDICAL APPLICATIONS

5.1. INTRODUCTION

Current approaches for the detection, identification, and treatment of critically ill patients often require bio-fluid samples obtained from a patient, to be sent to the lab for analysis, after which the results are forwarded to a physician for consideration and patient communication. This process can range from a few hours to several days depending on the characteristics of the target analyte, the measurement performed, and the level of expertise required to assess and disseminate the results. This long process can result in delayed response to some critical illnesses and have a real impact on the treatment efficiency. Methods for easy to use and rapid real-time detection of the physicochemical and biological changes produced by such illnesses and medical conditions would ensure rapid and efficient patient treatment, thus improving quality of life, and long-term treatment costs.[1]

As a prime example of this, for assessing the health status of an individual, measurement of blood pH can be very important and is one of the key metrics for patient condition and treatment. Disturbances in the body's finely balanced homeostasis impacts on many of the body's functions and can be reflected by small changes in blood pH.[2] Usually, intermittent sampling of arterial blood is made, and the samples are analysed in a central laboratory typically using a blood gas analyser. The snapshot in time nature of such measurements means that adverse events may be missed, and the health of the patient compromised.[3]

Whilst the potentiometric glass pH probe is commonly used for pH measurement due to its high proton selectivity and sensitivity,[4,5] its application *in vivo* is rather limited as a consequence of its fragility, difficulty in miniaturisation, and the need for frequent calibration.[2] A popular alternative for biomedical applications is the electrodeposited iridium oxide film (IrOx) pH sensor[6–11] which can be prepared on any electrode surface, allowing fabrication of miniaturised sensors. IrOx pH sensors have been used successfully to monitor in real-time the pH changes in brain tissue[12] and oesophagus for the monitoring

for gastroesophageal reflux disease.[13] However, being film-based, they suffer from long-term stability, a risk of film delamination and dissolution which results in toxic compounds being released into the fluid, and chloride complexation.[7]

The introduction of carbon-based pH sensors offers a biocompatible alternative, which is also capable of miniaturisation. Here it is the redox signature of quinone groups on the carbon surface which undergo proton-coupled electron transfer (PCET) that provide the pH sensitivity. These electrodes have shown a Nernstian response (-59 mV/pH unit at 298 K) to pH change.[14–17] As an electrode material, high quality BDD has been promoted in the literature as a low biofouling material, for both environmental[18,19] and biological applications,[20,21] thought to be due to its surface chemistry and low surface roughness.

Recent work has demonstrated the use of boron doped diamond-quinone (BDD-Q) electrodes, as sensors capable of exhibiting good pH sensitivity in buffered and unbuffered media.[16,17] Here the quinone groups were robustly integrated into the BDD surface via a laser machining process, which introduces regions of oxygen-terminated sp^2 bonded carbon into the surface (see also, Chapter 3 and 4). These regions also result in increased electrocatalytic activity and surface roughness compared to the starting BDD surface and thus may represent regions potentially susceptible to a higher risk of fouling, explored in Chapter 4. Furthermore, Chapter 3 explored the performance of both IrOx and BDD-Q pH sensors in the fouling media of 0.5% w/v mucin. It shown that the IrOx sensor pH response was significantly affected by the presence of mucin at the electrode surface.[22]

Wearable technologies for continuous non-invasive monitoring are increasingly popular. The best suited biofluids for non-invasive wearable sensors include sweat, wound fluid, interstitial fluid, tears, and saliva.[23–27] For sweat analysis, wearable patches, bands, and tattoos can facilitate electrochemical detection of biomarkers, such as glucose, and electrolytes.[28–31] However, it is not always clear how representative these measurements are of underlying tissue and blood levels. Electrochemical sensors implanted directly into the body offer accurate measurements of tissue analytes and have the potential to provide high temporal resolution.[32–35] For example, composite electrodes consisting of a carbon fibre core, coated with poly (*p*-xylylene) and poly(ethylene glycol)

polymer as an antifouling layer, have been implanted in the brain of a rat to monitor electrophysiological changes.[36] The sensor was able to provide a stable signal over 5 weeks in the brain without signal degradation. Schwerdt et al., reported a carbon fibre electrode implanted in the brain, capable of tracking and monitoring dopamine levels for up to one year.[37] Finally, implantable glucose sensors have been life-changing for diabetic patients, as this allows for continuous monitoring of blood glucose levels and be able to administer the appropriate insulin concentration required to balance changes.[38,39] However, implanted devices risk infection at the implant site, impaired specific response, possible thrombus formation,[40] which challenge sensor viability and longevity.[41]

An alternative approach is to develop analytical devices based on microfluidics, where rather than implanting the device biofluid is removed from the patient and taken to the sensor. There is also the possible advantage of solution flow across the device increasing mass transport of reactants to the electrode surface, thus increasing sensitivity, and decreasing the concentration of analyte that can be detected. Also fouling may be reduced in a flow environment. Such devices have been used to monitor patients with severe acute brain injury in intensive care units,[42–45] and monitoring cardiac arrest and resuscitation in animal models.[46]

Hydrodynamic fluidic flow cells are increasingly being produced using additive manufacturing (3D printing) techniques as these offer many advantages over traditional PDMS-based soft lithography.[42,47–50] These include access to a wider range of available materials, and a convenient route to scalability, which is essential in order to move from proof-of-concept lab-based systems to more easily manufacturable systems for early clinical trials. Devices can be produced in several unique and interesting geometries (e.g., solids containing internal voids)[48,50–52] and devices can be rapidly prototyped.

This study aims to develop a 3D printed flow cell in which BDD-Q pH electrodes can be readily incorporated, along with reference and counter electrodes and can easily be integrated with existing medical sampling lines. In this chapter, the hydrodynamic capabilities of an appropriately designed and 3D printed cell is first characterised by exploring the redox behaviour of 1 mM $Ru(NH_3)_6^{3+/2+}$ at different flow rates using a blank BDD disc electrode (1 mm

diameter). Following on from this, studies investigated the flow rate dependence on the pH measurement for both BDD-IrOx (buffered solutions) and BDD-Q (buffered and unbuffered solutions) pH electrodes. For biological pH measurements, firstly, the pH response of the BDD-Q electrode was investigated in 0.5% (w/v) mucin and 5% (w/v) bovine serum albumin (BSA) within the flow cell. As shown in Chapter 3 and 4, these are known fouling agents found in abundance in biological systems. Secondly, the response of the BDD-IrOx and BDD-Q pH electrodes in whole sheep's blood in Alsever's solution (an anticoagulant) was investigated.

5.2. EXPERIMENTAL

5.2.1. Solutions and Materials

Solutions were prepared using ultrapure water (Milli-Q, resistivity ≥ 18.2 MΩ cm at 25 °C). All chemicals were used as received. Flow cell characterisation measurements were carried out in solutions containing 1 mM hexaamineruthenium (III) chloride ($Ru(NH_3)_6^{3+}$, 99%, Strem Chemicals) with 0.1 M potassium nitrate (KNO_3, 99+%, Acros Organics). For studies in buffered solutions, buffers were prepared according to the procedure described by Carmody[53] over the pH range 2-10 using boric acid (H_3BO_3, 99.97%, Sigma-Aldrich), citric acid monohydrate ($C_6H_8O_7$, ≥ 99.5%, Sigma-Aldrich), and tertiary sodium phosphate (Na_3PO_4, ≥ 95%, Sigma-Aldrich) with a buffer capacity of 25-30 mM per pH unit.[53] For unbuffered solutions 0.1 M KNO_3 was pH adjusted with 1 M sulfuric acid (H_2SO_4, 98%, Sigma-Aldrich) or 1 M potassium hydroxide (KOH, ≥ 99.97%, Sigma-Aldrich) to create unbuffered solutions with pH values across the pH range 2-12. Flow measurements were conducted in the presence of two proteins that are commonly found in the body and provide a mimic for the environment in gastrointestinal tract (0.5% w/v mucin from porcine stomach (Type II, Sigma Life Science)) or in blood (5% bovine serum albumin (BSA, ≥ 96%, Sigma Life Science)), at biologically relevant concentrations. The mucin and BSA were added to a HEPES buffer solution, pH 7.4 (135.5 mM NaCl, 5.9 mM KCl, 2.5 mM $CaCl_2$, 1.2 mM $MgSO_4$, 5.0 mM HEPES, 3.5 mM NaOH, 10.0 mM glucose). All blood measurements were conducted in 50:50 sheep blood in Alsever's solution

comprising dextrose, sodium citrate, citric acid, and sodium chloride), obtained from TCS Biosciences Ltd. The preparation of IrOx solution and the electrodepositions of IrOx film on BDD is described in detail in Chapter 2.

5.2.2. Electrochemical Measurements

All voltammetric measurements were conducted using a three-electrode set-up, with SCE or silver-silver chloride (Ag|AgCl) reference electrodes (RE), and a coiled platinum wire counter electrode (CE, Goodfellow), using an Autolab PGSTAT128N potentiostat. Given the REs are used in fouling solutions, they were routinely monitored for any drift (relative to a master SCE RE). The coiled Pt wire was flame cleaned before use to remove any unwanted contaminants. A 1 mm diameter BDD disc, doped above the metallic threshold (minimal sp^2 content) and encapsulated with borosilicate glass,[54] was used as the working electrode (WE). This electrode employed to electrochemically characterise the flow hydrodynamics in the channel of the flow cell, using cyclic voltammetry (CV) at a scan rate of 100 mV/s. Fabrication of this electrode is described in Chapter 2.

For BDD-Q pH electrode experiments, a glass sealed 1 mm diameter BDD disk electrode containing a laser micromachined hexagonal array of 61, 50 μm diameter spots, with a centre-to-centre spacing of 100 μm was employed. Fabrication detailed in Chapter 2. The pH response was recorded using square wave voltammetry (SWV), parameters used include frequency = 100 Hz, amplitude = 50 mV, potential step = 4 mV. The BDD-Q electrode was stored dry when not in use, and between measurements, where necessary, the electrodes were polished first using alumina (0.05 μm, Buehler, Germany) paste on a micro-cloth pad (Buehler), and then on an ultra-pure water wetted alumina free pad.

For biological measurements with BDD-Q and BDD-IrOx electrodes, pH calibrations were performed pre- and post-biological measurement in mucin (0.5% w/v), BSA (5% w/v), or whole sheep's blood (in Alsever's solution). Calibrations were performed in Carmody buffer solutions before and after exposure to biological solutions. The electrodes were alternated between the biological media, and pH 7 Carmody buffer at least three times. For BDD-Q pH measurements, each pH measurement consists of six SWV scans, with the mean and standard deviation (error bars) reported. For the BDD-IrOx electrodes OCP

measurements are made with respect to a non-leak Ag|AgCl reference electrode, alternating between pH 7 Carmody buffer and biological media with at least three measurements in each solution. Each OCP measurement in buffer solutions are recorded for 60 s, and in the presence biological media this measurement time is extended until a plateau relative to the initial change is observed, and the end potential recorded.

All pH measurements were made using a Mettler Toledo SevenGo pH portable meter and InLab Expert Go-ISM glass probe prior to use with BDD-Q or IrOx electrodes. The glass probe is kept in the Mettler Toledo InLab storage solution when not in use, and a four-point calibration using pH 2, 4, 7, 10 Mettler Toledo standard buffer solutions was conducted, as per manufacturer guidelines.

5.2.3. Flow System and 3D Printed Flow Cell

All flow cells were designed using Autodesk Fusion 360 and printed using a Formlabs Form 3 stereolithography (SLA) printer. Flow cells were printed at a 50 µm layer height in Standard Clear Resin (Formlabs). The SLA parts (flow cell and electrode holders) were washed (FormWash, Formlabs) in isopropyl alcohol to remove any uncured resin then post-cured with 405 nm light at elevated temperatures (FormCure, Formlabs) according to manufacturer's recommended procedures.

A square shaped flow cell channel with dimensions of $2.5 \times 2.5 \times 30$ mm, tapered from the inlet pipe of 1 mm radius was designed. The WE is placed directly opposite the RE, in order to reduce the distance between these two electrodes, and so in turn minimise the uncompensated resistance in the system.[55] As the resin used for the 3D print is translucent, the position of both electrodes can be seen visibly. The CE is placed downstream, to avoid interference from the reactions occurs at the CE, as shown in Figure 5.1. The inlet and outlet tubing (silicone tubing 3.2 mm bore size) were connected directly to the cell, the direction of flow is indicated on the flow cell.
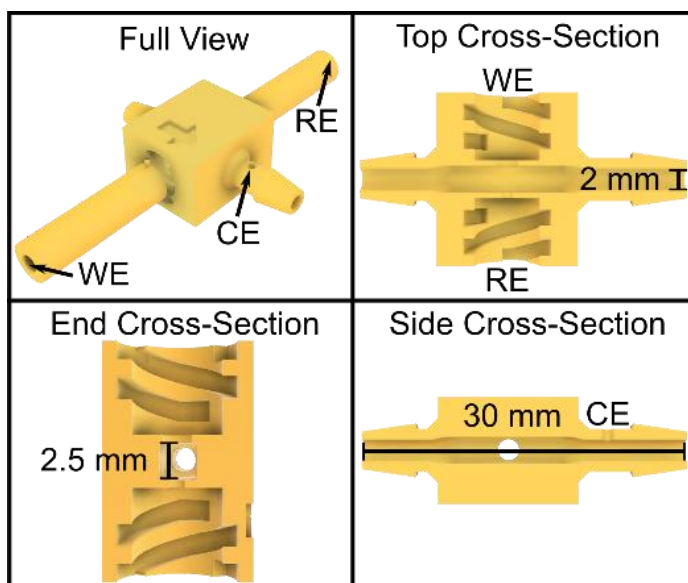
Figure 5.1. Schematic of the flow cell with cross-sections from top, end, and side of the cell, indicating the positions of working, reference, and counter electrodes.

Two separate syringes were used for the flow of fouling agents (BSA, mucin, and blood) and buffer solutions in the experiments conducted that involves alternating between solutions. Separate pipes were also used to avoid any cross contamination of fouling agents, these were manually switched between measurements, and cleaned between repeats by rinsing with ultra-pure water.

5.2.4. Data Analysis

Data analysis was conducted using OriginPro 9.85 (2021b, OriginLab Corp.), Python 3.6.5, and GraphPad Prism 9. For each individual SWV, excess electrical noise in the signal was removed using the Scipy Savitzky-Golay (an adjacent averaging method) filter with a second order polynomial and window length of five. The potential of the SWV current peak was identified using the Scipy find peaks function to identify minima within the bounds -0.2, and +0.45 V vs Ag|AgCl. A minimal horizontal distance between neighbouring peaks of 0.1 V is applied to remove false positives resulting from noise and the most prominent remaining peak is selected. For biological media data, this method is applied to the mean of six sweeps for a given run and the output data is further processed

using Origin to convert the potential values to a pH using the calibration conducted prior to exposure in biological media, and the mean of the six sweeps is reported with the standard deviation error bars.

For pH calibrations .csv files containing the mean smoothed data for each pH buffer are processed using the peak picking method describe above. Calibration parameters are extracted via linear regression of solution pH vs peak potential data, where each data point represents the mean value of the final five of six recorded sweeps after smoothing, with the first sweep discarded in each case. All figures and further analysis of data are prepared in Origin. To evaluate statistical difference in the alternating pH measurements conducted between fouling media (mucin, BSA, and blood) and buffer solutions, under stationary and flow conditions, a one-way analysis of variance (ANOVA) adjusted for Tukey correction was employed. Differences were considered statistically significant at a probability of $p < 0.05$.

5.3. RESULTS AND DISCUSSIONS

5.3.1. Device Fabrication & Electrochemical Characterisation of 3D Printed Flow Cell

It is essential for understanding electrochemical behaviour in the flow cell to first verify that the hydrodynamics of the flow cell are well-defined and predictable (laminar flow). In order to have an indication of the flow profile within the flow cell channel, the Reynolds number (Re) can be calculated using Equation 5.1. Typically, laminar flow has a Re < 2000, while a turbulent flow will give higher values.

$$Re = \frac{\bar{U}D_h}{v}$$
Equation 5.1

$\bar{U}$ is the mean fluid velocity (cm/s), which is related to V_f (cm^3/s) by Equation 5.2, D_h is the hydraulic diameter (cm), defined by Equation 5.3, and v is the kinematic viscosity ($\sim$0.01 cm^2 s^{-1} for water at 20 °C).

$$\bar{U} = \frac{V_f}{2hw_{ch}}$$
Equation 5.2

where, $2h$ and w_{ch} are the height and width of the square-shaped flow cell channel.

$$D_h = \frac{8hw_{ch}}{2h + w_{ch}} \qquad \text{Equation 5.3}$$

For the flow cell described here, under the flow rates explored (0.1 to 100 mL/min), the flow profile is well-defined and laminar with Re = 83 at the highest flow rate (100 mL/min). Previously, band[47] and micro-disk[56] electrodes have been used to access the flow characteristics within a channel flow cell, however, here we explore the use of a macro (1 mm diameter) BDD disk electrode, placed in the channel as shown in Figure 5.1. The flow cell was easily assembled with a commercial Ag|AgCl RE, Pt wire CE, and a BDD WE fabricated using in-house standard packaging methods.[54] Even under the higher volume flow rates (100 mL/min) explored, no leak from the flow cell was observed. The channel is designed such that the electrode surface sits co-planar with the wall to avoid interference with solution flow this was confirmed *via* a visual assessment.

Figure 5.2(a) shows CVs for the one-electron reduction of 1 mM $Ru(NH_3)_6^{3+}$ in 0.1 M KNO_3, using the BDD macroelectrode in the flow cell at a potential scan rate of 100 mV/s, over the V_f range 0.1-100 mL/min (the limit of syringe pump system). Figure 5.2(b) displays the steady state limiting current, i_{lim} (taken from the experimental CVs in (a)) versus $V_f^{1/3}$, to verify the dependence of flow rate with i_{lim} over the flow rates investigated.
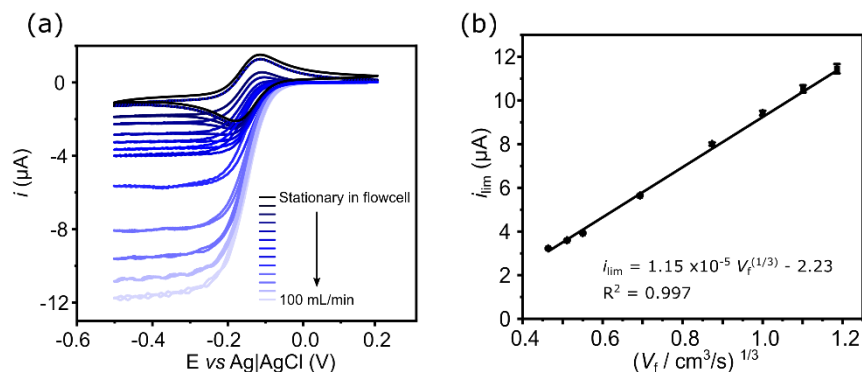
Figure 5.2. (a) CV for 1 mM $Ru(NH_3)_6{}^{3+/2+}$ redox process on BDD electrode in a flow cell, with increasing flow rates from stationary in the flow cell to 100 mL/min (b) plot of limiting steady-state current *vs* volume flow rate to ⅓ to fit the Levich equation (error bars represent the standard deviation of the mean of n = 3).

As shown in Figure 5.2, at a volume flow rate of 6 mL/min, there is a transition from a peak shaped CV to a CV which displays both a limiting current response, and the absence of a return peak. The latter is indicative of the increased mass transport of species to and away from the BDD electrode surface. Increasing convection increases the flux of reactants towards and products away from the electrode surface,[57] which in turn enhances the faradaic current signal, and also means there is no product to collect in the CV. At higher flow rates (60 – 100 mL/min) the current response in Figure 5.2a shows periodic oscillations, this is due to the noise generated from the pump.

Under fully developed laminar flow and for conditions where concentration changes are confined close to the channel wall (fast flow and/or short electrodes), such that the Poiseuille velocity profile can be linearized (the Lévêque approximation),[58] the i_{lim} response, should obey the Levich equation, which predicts a linear dependence of i_{lim} on $V_f^{1/3}$. Figure 5.2b shows a plot of i_{lim} versus $V_f^{1/3}$ where the experimental data also shows a linear relationship with an R^2 of 0.997 (n = 3). In the literature this behaviour is found most often for band electrodes incorporated into channel flow cells.[47,57]

5.3.2. BDD-Q & BDD-IrOx pH Electrodes

As detailed in the introduction, accurately detecting real-time changes in physiological pH could be crucial for the early detection of numerous diseases[2,59–61] and flow can be useful in bringing solution to the detector. For certain analytes, medical devices can take advantage of the relationship of flow with signal intensity to improve detection limits. Flow-based systems can also be used for continuous long-term monitoring,[42,43] demonstrating application, for example, within the intensive care unit for online monitoring of key neurochemical (glutamate, glucose, and lactate levels) changes of a brain injury patient.[42] With regards pH measurements in flow, it is important to ascertain that the measured pH is independent of the flow rate used.

Potentiometric IrOx pH sensors have been used extensively in the literature for pH sensing applications, in particular the ability to deposit pH sensitive IrOx on miniaturised sensor formats has driven interest in their use for biomedical applications.[7] Due to this popularity, IrOx electrodes were used in this study as a suitable performance comparison for BDD-Q pH sensors. The primary concern when using any electrodeposited film under flow is the potential for delamination at increased flow rates.

Herein, a 1 mm diameter BDD disk was functionalised with an IrOx film and inserted into the flow cell. The OCP of the sensor was measured in three different buffer solutions (4, 7, and 10) as a function of flow rate for three different flow rates (1, 10, and 100 mL/min). Unlike the potentiometric glass pH electrode which exhibits a Nernstian behaviour in response to pH changes,[10] the super-Nernstian behaviour (72 mV per pH unit change) observed in Figure 5.3 is expected for electrodeposited IrOx pH sensors.[62] Figure 5.3 shows the OCP of the IrOx-BDD electrode plotted as a function of pH for the stationary (n = 3) and at three different volume flow rates (n = 1) employed.
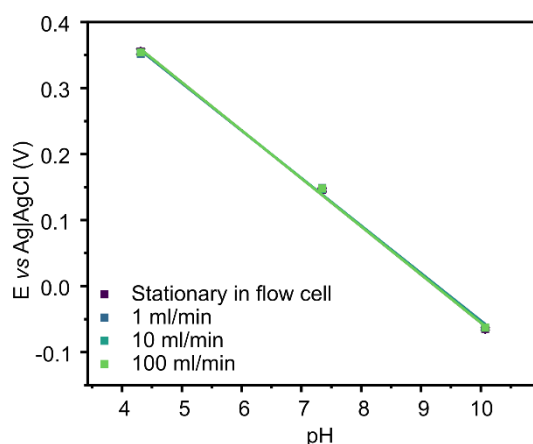
Figure 5.3. Flow rate dependence of the pH response of a BDD-IrOx pH sensor. Measurements are conducted in buffer solutions at flow rates 0, 1, 10, and 100 mL/min using OCP.

For the IrOx BDD pH sensor the linearity of the OCP versus pH slope remain effectively unchanged ($R^2 = 0.998$) as a function of V_f. Table 5.1 reports the calibration slope and intercept, which can also be seen to remain consistent up to flow rates of 100 mL/min. The stationary (0 mL/min) measurements were conducted in triplicate, however, only one measurement was conducted at each flow rate due to concerns over possible delamination of the IrOx film from the BDD electrode, with extended use.

Table 5.1. Summary of the gradient and intercept for the calibration curves for BDD-IrOx, stationary in the flow cell, and at different flow rates (1, 10, 100 mL/min). R^2 of all calibration curves for BDD-IrOx included is 0.998.

Flow rate (mL/min)	Gradient (mV)	Intercept (mV)
0	-72.8	673
1	-72.0	667
10	-72.3	670
100	-72.8	673

This data show that under these flow conditions explored, the IrOx film is sufficiently stable such that the potentiometric measurements remain consistent as a function of volume flow rate. In comparison, Figure 5.4 shows the

impact of flow rate on the pH measurements using the voltammetric BDD-Q pH sensor for (a) buffered (pH 2-10) and (b) unbuffered 0.1 M KNO_3 (pH 2-12, where pH is varied using H_2SO_4 or KOH) solutions. For the former (a) Carmody buffers were used at pH values of 2, 4, 7, and 10. For the latter, 6 pH measurements were made at pH 2, 4, 6, 8, 10, and 12.
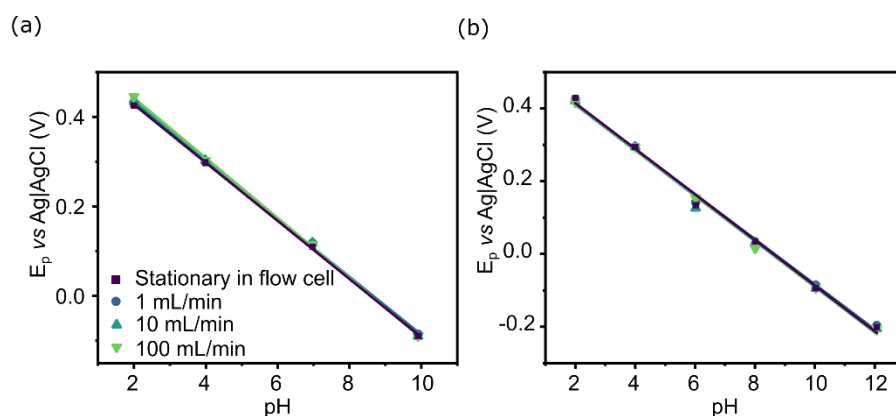
Figure 5.4. BDD-Q pH electrode calibration curves in (a) buffered and (b) unbuffered solutions at flow rates 0, 1, 10, and 100 mL/min.

Although twelve flow rates from 0.1, 1, 2, 4, 6, 8, 10, 20, 40, 60, 80, and 100 mL/min were tested, for clarity in Figure 5.4, only stationary in the flow cell, and flow rates of 1, 10, and 100 mL/min calibrations are shown. The mean of the SWV peak potential (E_p, e.g., as shown in Chapter 3) obtained from five SWV scans were analysed for each data point, with the standard deviation presented as error bars. Good linearity (lowest $R^2 = 0.993$ for stationary unbuffered) between the pH (measured using a potentiometric glass pH probe) and peak potential of the BDD-Q SWV response is observed.

Table 5.2 shows the mean calibration parameters for triplicate measurements using the BDD-Q pH electrode for stationary and at flow rates of 0.1, 1, 2, 4, 6, 8, 10, 20, 40, 60, 80, and 100 mL/min. The minimal variation in calibration gradients observed across the flow rates assessed in Figure 5.4a and b, demonstrates flow rate independence in both buffered and unbuffered solutions. This is particularly encouraging, providing certainty when moving towards biological applications with uncontrollable variables (such as biofouling), that any pH changes observed are due to the biological media explored and not a result of the flow system.

Table 5.2. Summary of the gradient and intercept for the calibration curves for BDD-Q. R^2 of all buffered and unbuffered calibration curves included is at least 0.999 and 0.995, respectively. Standard deviation error bars of n =3.

Flow rate (mL/min)	Buffered		Unbuffered	
	Gradient (mV)	Intercept (mV)	Gradient (mV)	Intercept (mV)
0	-65.8 ± 0.82	566 ± 8.8	-63.4 ± 0.67	537 ± 3.8
0.1	-66.2 ± 0.15	571 ± 2.3	-63.8 ± 1.22	545 ± 6.9
1	-65.8 ± 1.03	567 ± 6.9	-63.3 ± 1.19	539 ± 2.5
2	-65.3 ± 0.42	565 ± 4.7	-63.4 ± 0.96	538 ± 6.4
4	-66.4 ± 0.34	572 ± 2.3	-62.9 ± 0.46	535 ± 5.3
6	-66.3 ± 0.29	572 ± 3.0	-63.2 ± 1.04	537 ± 7.8
8	-65.6 ± 1.02	566 ± 4.9	-63.4 ± 0.87	539 ± 6.1
10	-65.9 ± 0.41	569 ± 5.4	-63.7 ± 1.00	542 ± 7.8
20	-66.0 ± 0.26	571 ± 2.1	-64.2 ± 0.67	549 ± 7.4
40	-65.9 ± 0.27	569 ± 4.7	-63.7 ± 0.56	544 ± 3.0
60	-66.0 ± 0.53	568 ± 6.3	-64.3 ± 1.05	549 ± 7.6
80	-66.2 ± 0.76	572 ± 6.0	-63.9 ± 1.69	546 ± 12.6
100	-66.2 ± 0.83	571 ± 7.1	-63.7 ± 0.97	545 ± 8.8

For the reduction of $Ru(NH_3)_6^{3+}$ on the unfunctionalised BDD electrode in Figure 5.2, increasing V_f results in an increase in the current and change in CV profile from peak shaped to limiting current. For the BDD-Q measurements, we are interested not in the magnitude of the peak current, but simply its position on the potential axis and under the flow conditions adopted this can be seen to remain constant. Interestingly the current magnitude of the SWVs also do not appear to change with flow rate, as shown in Figure 5.5 for (a) buffered pH (i) 2, (ii) 7, (iii) 10 and (b) unbuffered pH (i) 2, (ii) 8, (iii) 10, while stationary (black) and at flow rate of 100 mL/min (red).
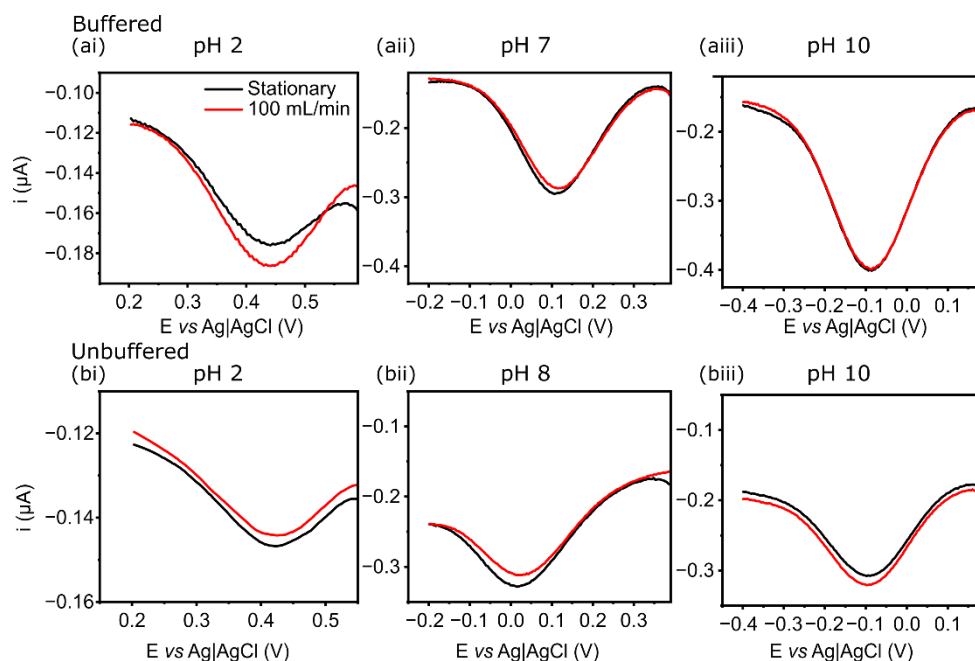
Figure 5.5. SWV scans for (a) buffered and (b) unbuffered pH measurements in solutions of pH (i) 2, (ii) 7 (buffered) or 8 (unbuffered), and (iii) 10

This could be due to very low surface coverage of quinone groups on the BDD-Q surface, effectively resembling an array of nanoelectrodes,[17] meaning that under stationary conditions diffusion of protons to the individual quinone groups is already high, as the diffusion coefficient of H+ is 9.3×10^{-9} m2/s.[63] Increasing the convective contribution of H+ flux to the quinone surface by increasing the flow rate is clearly not having a significant effect due to the already high diffusional flux. Similar behaviour was seen when observing the voltammetric response of a microarray electrode in a channel flow cell i.e. no enhancement in the i_{lim} was observed under flow conditions.[64] We also note that the resulting components of the SWV (forward and reverse wave, which when added together give the output SWV response) lie on top of each other suggesting reversibility.[65] This is shown in Figure 5.6 for (a) buffered pH (i) 2, (ii) 7, (iii) 10 and (b) unbuffered pH (i) 2, (ii) 8, (iii) 10, while stationary (black) and at flow rate of 100 mL/min (red). Even at the highest flow rate, this behaviour is still seen, suggesting that the proton coupled electron transfer process has not become rate limited.
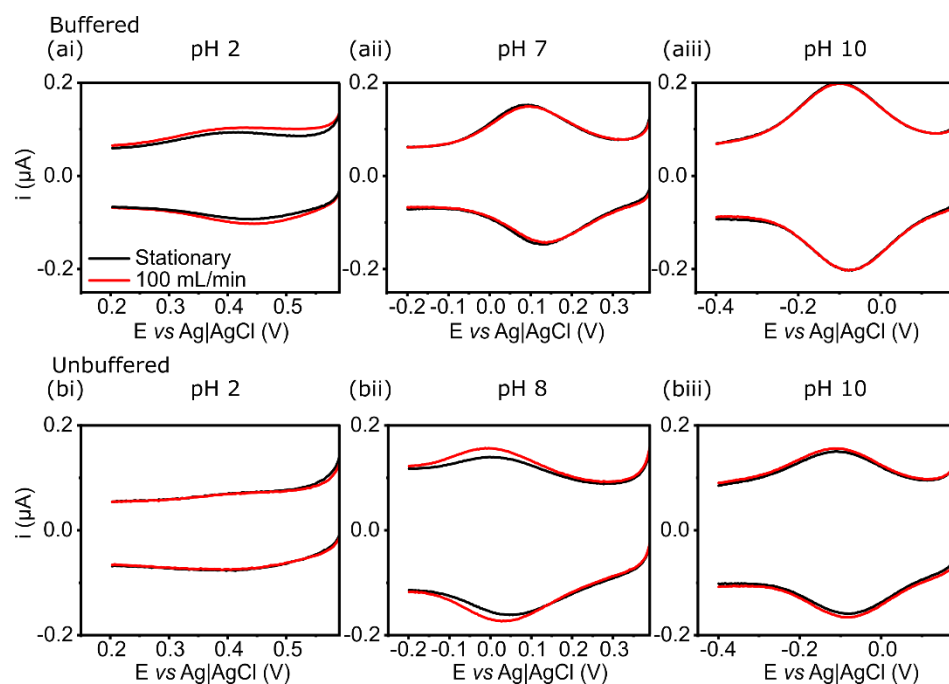
Figure 5.6. Forward and reverse scans for SWVs for (a) buffered and (b) unbuffered for pH (i) 2, (ii) 7 (buffered) or 8 (unbuffered), and (iii) 10

5.3.3. Biological Media Measurements

Electrochemical measurements in biological media are challenging due to the complexity of the matrix which contain different proteins, amino acids, phenols, neurotransmitters, and other biological molecules.[66,67] The effects of these molecules can be observed in stationary measurements described in Chapter 3 and 4 where it is shown how the presence of BSA/mucin (proteins) cause fouling of the electrode surface, resulting in inaccuracy and unreliability of the measurement and the sensor.[66] Therefore, it is important to develop a robust pH electrode which can be placed in different protein containing solutions with confidence that the electrode performance has not been compromised by the complex environment, and the measurements are reliable.

Figure 5.7 shows pH measurements conducted in bulk solutions under stationary conditions first of (a) 5% w/v BSA and (b) 0.5% w/v mucin in HEPES buffer solutions. Note, in regard to Chapter 3, here we do six consecutive scans instead of rinsing between scans as described in Chapter 3, to assess any electrode fouling. Each data point represents the peak potential derived from the mean of six SWV scans with standard deviation error bars. One full run involves

first (1) calibrating the electrode using Carmody buffers (4, 7, 10). (2) Then place in a pH 7 Carmody buffer record the pH using SWV (mean of six scans). (3) Then place in the respective protein solution, measure pH using SWV (mean of six scans). (4) Then place back in the pH 7 Carmody buffer, measure pH using SWV (mean of six scans). Note the last two steps are repeated a further two times so in total for each run there are three protein and four buffer measurements. Finally (5) the electrode is re-calibrated using Carmody buffers (4, 7, 10). The pre-protein calibration (1) was used to calculate the pH measured on the BDD-Q pH electrode. Three runs were recorded in total, noting that before starting a new run the electrode is cleaned using an alumina polish ready for pre-calibration.

Each SWV scan takes ~5 s, therefore, for each protein or buffer measurement the BDD-Q is exposed to this solution for ~50 s. Figure 5.7(i) shows the sixth SWV scan in BSA and mucin, for Run 1. Figure 5.7a(i) shows that when alternating the pH measurement between buffer and BSA, the sixth SWV scan in BSA shows a slight shift towards lower potentials, resulting in an alkaline shift, shifting from 91 to 87 to 83 mV (shift of 8 mV which corresponds to 0.13 pH units). In contrast, with mucin (Figure 5.7b(i)) the peak potential shift is more random, with the peak potential shifting from 166 to 154 to 162 mV (shift of 12 mV, corresponding to 0.19 pH units)over the three repeats.
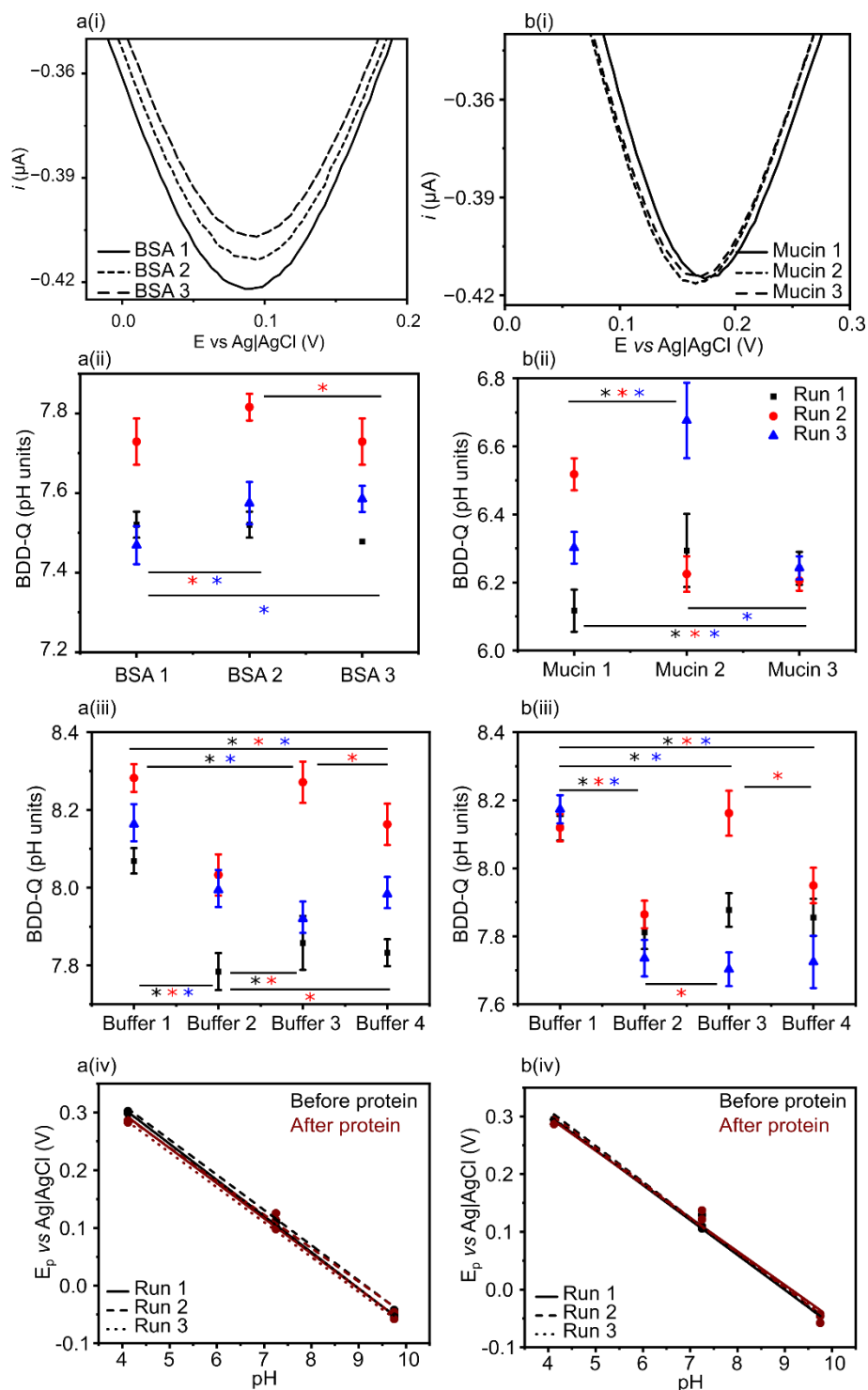
Figure 5.7. pH measurements conducted in bulk stationary solutions of (a) 5% w/v BSA and (b) 0.5% w/v mucin in HEPES buffer solutions. (i) The sixth SWV scans from each alternating measurement for Run 1. Average pH measured using the BDD-Q electrode while alternating between (aii) 5% w/v BSA, or (bii) 0.5% w/v mucin and (iii) Carmody buffer pH 7 in bulk stationary solutions,

with standard deviation error bars n = 6. (iv) The before and after protein calibrations for BDD-Q pH sensor. Data shown as mean ± standard deviation, *p* < 0.05.

The average peak potentials per repeat can be converted to a pH value using the pre-calibration gradient data. Figure 5.7a (ii) shows the three repeats for the BSA data as a function of run number, where the black data points represent Run 1, red represent Run 2 and blue represent Run 3. For each individual run in BSA, a one-way ANOVA at a 5% significance level test demonstrates statistical significance in the pH measured in Run 2 and 3 (except Run 1). Also shown is the data for pH recorded in the Carmody pH 7 buffer as a function of run number and repeats per run. Here the four buffer measurements within the run (Figure 5.7a (iii)), show no clear agreement and shift randomly, and statistically significant. For all three runs, the greatest difference in buffer pH is observed between the first buffer measurement (i.e., prior to first BSA measurement) and the second buffer measurement, with shifts of 0.29, 0.25, and 0.17 pH units, respectively for runs 1, 2 and 3. The inconsistency in the buffer pH measurements indicates that there is likely to be carry-over of protein on the surface of the pH electrode to the buffer solution to varying degrees.

In contrast to BSA, in the mucin solutions, Figure 5.7b (ii) shows that the three repeat pH measurements per run in mucin are not consistent and the differences are statistically significant. For example, taking Run 1 and 3 data, and looking at the first and second repeat data in mucin, they show a pH increase from pH 6.12 ± 0.06 (Run 1) and pH 6.30 ± 0.05 (Run 3) to pH 6.29 ± 0.11 and pH 6.67 ± 0.11, respectively. In contrast, in Run 2, the pH decreases from pH 6.52 ± 0.05 (first) to pH 6.22 ± 0.05 (second). The buffer measurements recorded prior to mucin (Buffer 1) and directly after mucin (Buffer 2) in Figure 5.7b (iii) are statistically significant at *p* < 0.05 (one-way ANOVA with Tukey correction for multiple comparison), and show a similar response to that observed for BSA (Figure 5.7a (iii)) with a decrease of 0.31, 0.26, and 0.44, for Runs 1, 2, and 3 respectively. The significant difference in pH between repeats in both, protein, and buffer measurements, suggests electrode fouling from protein adsorption on

the BDD-Q surface. However, the fouling is not reproducible and therefore measurements cannot be easily corrected to account for the fouling observed.

Table 5.3. Calibration equation in the format, y = mx + c, where y = E_p and x = pH, and the R^2, for pH measurements conducted in bulk solutions before and after exposure to 5% w/v BSA or 0.5% w/v mucin.

	BSA		Mucin	
	Before (mV)	After (mV)	Before (mV)	After (mV)
1	-62.7 pH + 559	-60.9 pH + 543	-60.5 pH + 544	-58.1 pH + 531
	0.999	0.998	1	0.998
2	-61.0 pH + 558	-58.0 pH + 529	-62.2 pH + 560	-60.6 pH + 549
	0.999	0.996	0.995	0.990
3	-62.5 pH + 558	-60.4 pH + 533	-60.4 pH + 545	-58.8 pH + 535
	0.999	0.999	0.999	0.998

Table 5.3 shows the calibration gradients and intercepts for the BDD-Q electrode recorded at the start and finish of each run. As can be seen there is only a small difference in the pre- and post-calibration gradients as shown in Figure 5.7a,b (iv) and listed in Table 5.3. This suggests that the adsorption of BSA and mucin is weak, and the proteins can start to be removed just via the action of placing the electrodes in and out of buffer solutions. In Chapter 3 it was shown simple rinsing was an effective method for removing mucin from the surface of the BDD-Q electrode. To explore a more effective and controllable method of removing / reducing protein-based fouling from the BDD-Q electrode surface, use of the flow system described above was explored. Convection was thought to be a useful method for minimising protein fouling as the adsorption of proteins to the BDD-Q is weak and reversible.[22] The physical action of flowing solution may prevent protein adsorption in the first place or remove any loosely bound protein from the surface.

Figure 5.8 shows the pH measurements conducted using the BDD-Q electrode with solutions flowing at 100 mL/min (the highest flow rate possible on the syringe pumps used), for (a) 5% w/v BSA and (b) 0.5% w/v mucin in

HEPES buffer solutions. As the BDD-Q pH electrode measurements have been shown to be flow rate independent (Figure 5.4), any pH changes observed can be associated with possible fouling from protein adsorption. The same measurements were conducted as for the stationary experiments described in Figure 5.5, but now under flow, Figure 5.8 As before, each data point represents the mean of six SWV scans with standard deviation error bars.
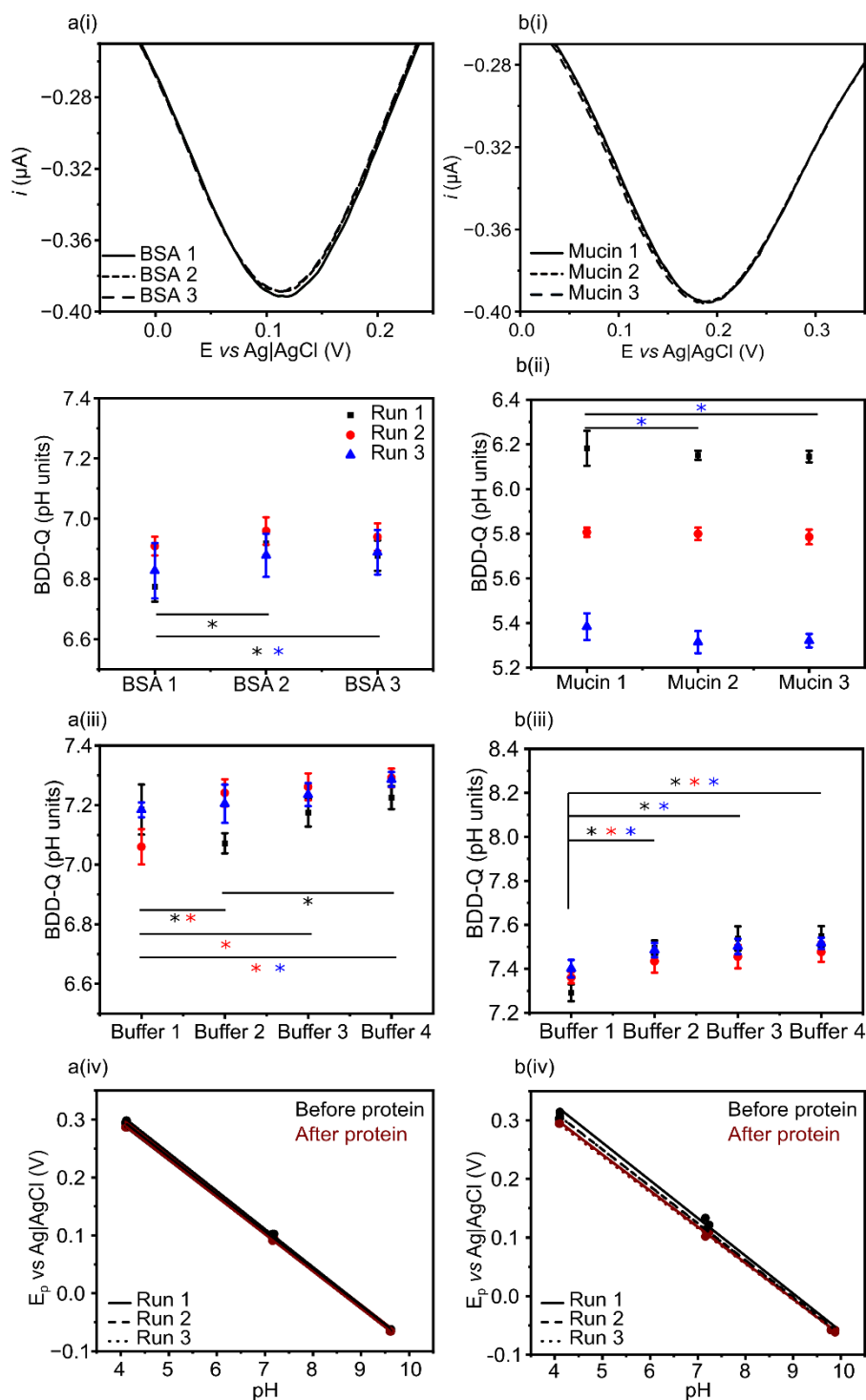
Figure 5.8.   pH measurements conducted under applied flow rate of 100 mL/min for solutions of (a) 5% w/v BSA and (b) 0.5% w/v mucin in HEPES buffer solutions. (i) The sixth SWV scans from each alternating measurement for Run 1. Average pH measured using the BDD-Q electrode while alternating between (aii) 5% w/v BSA, or (bii) 0.5% w/v mucin and (iii) Carmody buffer pH 7 in bulk stationary solutions, with standard deviation error bars n = 6. (iv) The before and after protein calibrations for BDD-Q pH sensor. Data shown as mean ± standard deviation, *$p < 0.05$.

Figure 5.8a, b(i) shows the sixth SWV scan recorded for pH in the repeat buffer and BSA/mucin solutions for Run 1. Both sets of data show good agreement with minimal peak shifting. For BSA a shift was observed from 118 (BSA 1) to 114 mV (BSA 2 and 3) and for mucin, a shift from 199 (mucin 1 and 2) to 203 mV (mucin 3), both corresponds to a pH shift of 0.06 pH units.

For BSA (Figure 5.8a(ii)), statistically significant difference in pH was observed in Run 1 (one-way ANOVA, $p < 0.05$), with BSA 1 pH measuring 0.14 and 0.10 pH units less than BSA 2 and 3, respectively. However, Run 2 and 3 show good statistical agreement, with the largest difference of 0.05 and 0.06 pH units, respectively, measured between BSA 1-3. For mucin, Figure 5.8b(ii), Run 1 and 2 show good agreement, with largest difference of 0.04 and 0.02, respectively. However, the pH measured in Run 3 for mucin 1 significantly differs from the pH recorded for mucin 2 and 3, with a difference of 0.07 pH unit.

The alternating buffer pH measurements with BSA, Figure 5.8a(iii), shows that in Run 1, buffer measurements 1, 3 and 4 are good agreement with buffer 2, possibly an outlier measuring 0.11, 0.10, and 0.15 pH units less than buffer 1, 3, and 4, respectively. Run 2 shows good agreement between buffer measurements 2, 3, and 4 (largest difference of 0.05 pH units). Finally, Run 3 shows good agreement between all four buffer measurements (0.05 pH unit difference). For the pH measurements in buffer alternating with mucin, in all three runs, there is a good agreement between buffer measurements 2, 3, and 4, however, these are statistically different to the buffer 1, with 0.26 and 0.12 pH unit difference observed in Run 1, and Run 2 and 3, respectively. Furthermore,

similar to stationary measurements, the sensor calibrates well pre- and post-protein exposure (Table 5.4).

Table 5.4.   Calibration equation in the format, y = mx + c, conducted in stationary bulk Carmody buffer solution for pH measurement of 5% w/v BSA or 0.5% w/v mucin and buffer solution under flow (at 100 mL/min).

	BSA		Mucin	
	Before (mV)	After (mV)	Before (mV)	After (mV)
1	-64.5 pH + 561 0.999	-63.8 pH + 549 0.999	-64.4 pH + 584 0.999	-61.7 pH + 550 0.999
2	-65.7 pH + 571 0.999	-64.2 pH + 553 0.999	-63.0 pH + 565 0.998	-61.7 pH + 550 0.999
3	-64.9 pH + 560 0.999	-64.2 pH + 551 0.999	-63.1 pH + 566 1	-61.1 pH + 544 0.999

In comparison to the pH measurements conducted under stationary bulk conditions, measuring the pH of BSA and mucin under flow (100 mL/min) using BDD-Q electrode results higher precision, with smaller error on each data point. Furthermore, two out of three runs in mucin and BSA, and pH measurements for buffers 2, 3, and 4 show good agreement. Therefore, this experiment shows that flow has the potential for reducing fouling of BDD-Q electrodes by individual protein solutions. However, biological samples tend to be more complex, containing a mixture of proteins. One such example is blood. Herein, we explore and compare the pH measurement recorded in whole sheep's blood in Alsever's solution using both the BDD-IrOx and BDD-Q pH sensors.

Initial assessments of performance in blood were conducted in bulk solutions under stationary conditions for both the BDD-IrOx and BDD-Q electrodes. OCP data from the BDD-IrOx electrode is presented in Figure 5.9. Here the electrode was calibrations prior to and after exposure to blood. Between calibrations alternating SWV measurements were conducted in pH 7 Carmody buffer (×3) and blood (×3), as above. The measured pH for each experiment was calculated using the initial pre-calibration and the results compared to the

calibration plots. For BDD-IrOx electrode calibrations, the OCP (which is converted to pH via the calibration line) was allowed to run until a stable potential was reached, or until it was observed that a stable potential will not be reached in a reasonable time (>>60 s). The potential reported is the potential measured at the end of this duration.
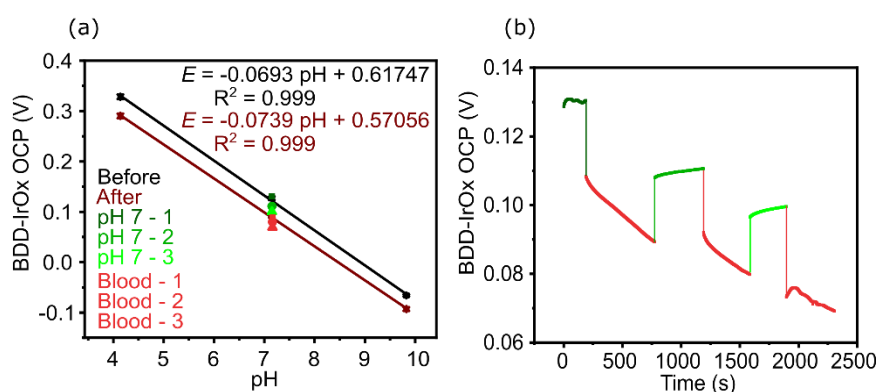
Figure 5.9. (a) pH calibration of BDD-IrOx electrode before and after exposure to blood. (b) OCP measurement for each calibration and alternating in blood (red) and buffer (green)solution.

Figure 5.9a. show that whilst the IrOx electrodes respond linearly to pH both before and after the buffer/blood pH measurements, with a similar calibration gradient in each case, 69.3 mV and 73.9 mV respectively, there is an offset of -0.047 V when comparing the intercepts. When looking at the OCP data in Figure 5.7b, it is clear that the IrOx electrodes struggle to recover from exposure to blood. The initial buffer OCP data shows a flat line (green line), when placed in the blood for the first time (red line) the OCP continually drifts down. When placed back in the buffer, the OCP does not completely stabilise in the time frame assessed here, and the second placement in blood again shows a clear drift downwards in OCP which is repeated for the third buffer/blood repeat.

The performance of the BDD-IrOx electrodes for blood pH measurements under flow conditions is also assessed. It is possible that flow conditions may prevent proteins in the blood from sticking onto or absorbing into the IrOx, thus improving the measurement reproducibility as observed with the BDD-Q electrodes in BSA and mucin. An initial flow rate of 100mL/min was

selected as a faster flow rate was thought to offer the highest chance of success in inhibiting fouling. As with the stationary measurements, calibrations in buffer solutions were conducted before and after alternating measurements in pH 7 buffer and blood. The resulting data collected on three different BDD-IrOx electrodes is presented in Figure 5.10.
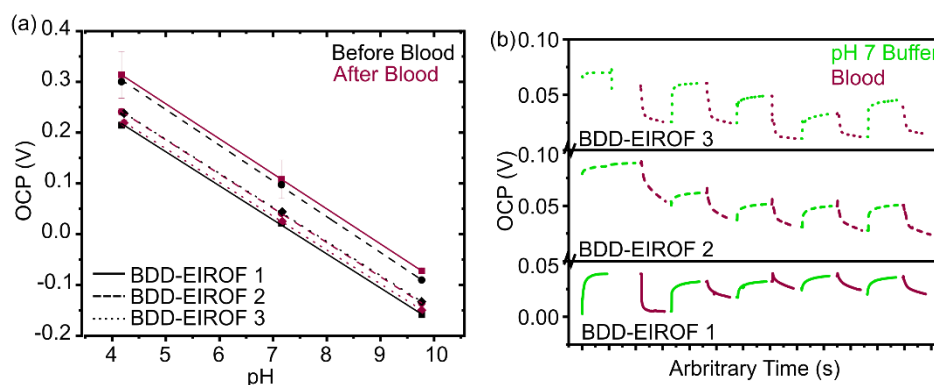
Figure 5.10. (a) pH Calibrations for BDD-IrOx electrodes before (black) and after (red) exposure to blood. Line type represents individual electrodes. (b) OCP measurements for BDD-IrOx electrodes alternating between pH 7 buffer (green) and blood (red) solutions at a flow rate of 100 mL/min. Data is plotted on an arbitrary time scale for ease of comparison.

It is evident from Figure 5.10(a) that, as under stationary conditions a shift in the calibration parameters (especially intercept) is observed on all three electrodes, (Table 5.5). The variation differs between electrodes most likely due to biological fouling being surface dependent (reflecting the difficulty in producing identical IrOx electrodes) and rarely reproducible. Furthermore, in buffer, the pH response approaches stability (although at varying potentials between runs) but a significant drift which does not stabilise on the timescale measured (≥ 60 s) is observed in the blood measurements (Figure 5.10b), as was observed under stationary conditions. The lack of stabilisation in the OCP value is also indicative of flow being unable to stabilise the IrOx response. It is unlikely therefore, that IrOx could be applied to biological pH measurements of blood, even when incorporated into a flow system.

Table 5.5.   Calibration equation in the format, y = mx + c, conducted in stationary bulk Carmody buffer solution using BDD-IrOx, for pH measurement of blood and buffer solution under flow (at 100 mL/min).

	Before (mV)	After (mV)
1	-66.7 pH + 495	-69.0 pH + 602
	0.999	1
2	-69.8 pH + 593	-67.3 pH + 522
	0.999	0.999
3	-66.9 pH + 521	-66.5 pH + 501
	0.999	0.999

Initial pH measurements in blood under stationary conditions for BDD-Q are presented in Figure 5.11(a) and recorded as detailed for BSA/mucin experiments, except in order to reduce the volume and exposure time of blood to the electrode surface, now six scans were recorded, with the sixth scan being shown. Fig 5.9 (b,c) shows the three alternate measurements conducted in sheep's blood (b) and (c) pH 7 Carmody buffer, and (d) the calibration of the BDD-Q pH sensors using Carmody buffers conducted pre- and post-exposure to sheep's blood. Each data point represents the mean of six SWV scans with standard deviation error bars.

In Figure 5.11a, the sixth scan for each alternate measurement in blood (for Run 1) shows a cathodic shift in the peak potential (102 to 98 to 95 mV) which equates to an alkaline pH shift of 0.12 pH units calculated using the calibration line, E_p = 64.6 pH + 556 (mV *vs* Ag|AgCl). With alternate pH measurements between blood and buffer, Runs 1, 2, and 3 show an overall alkaline shift of 0.13, 0.04 and 0.14 pH units in blood respectively (Figure 5.11b), where pH difference measured in pH for Run 1 and 3 are statistically significant between blood 1 and 3, calculated using one-way ANOVA, $p < 0.05$. Figure 5.11c shows an alkaline shift in buffer pH in all three runs as well, with an overall 0.11, 0.17, and 0.12 pH units for Runs 1, 2, and 3, respectively.
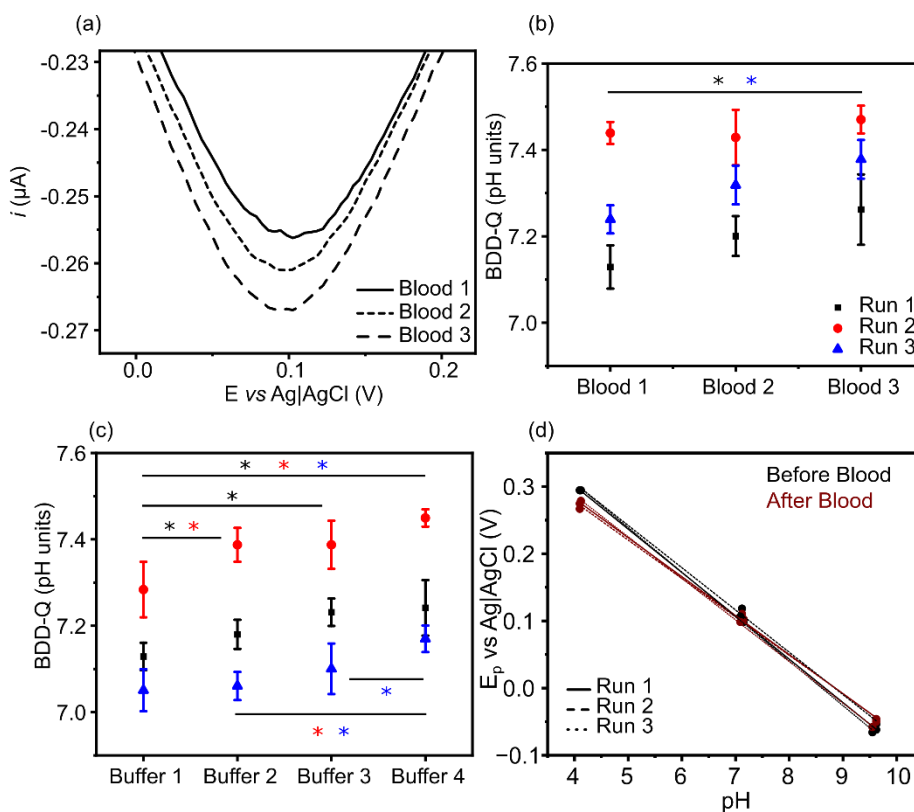
Figure 5.11. pH measurements conducted in bulk sheep's blood under stationary conditions, with (a) the sixth SWV scans from each alternating measurement for Run 1. Average pH measured using the BDD-Q electrode while alternating between (b) blood and (c) Carmody buffer pH 7, with standard deviation error bars n = 6. (d) The before and after blood calibrations for BDD-Q pH sensor. Data shown as mean ± standard deviation, *$p < 0.05$.

As with the BDD-IrOx, pH measurements conducted using BDD-Q electrodes in bulk stationary blood are showing evidence of fouling. This behaviour also correlates well with the results observed in stationary for BSA and mucin solutions. Furthermore, as with calibrations performed pre- and post-protein exposure, the calibrations prior to and post blood immersion show fairly good agreement (Figure 5.11, Table 5.6), with slight deviations at the lower pH (4) and higher pH (10).

Table 5.6.   Calibration equation in the format, y = mx + c, conducted in stationary bulk Carmody buffer solutions using BDD-Q, for pH measurement of blood and buffer solution in stationary solutions.

	Before (mV)	After (mV)
1	-64.6 pH + 559 0.999	-58.0 pH + 514 0.999
2	-63.0 pH + 557 0.998	-57.2 pH + 506 0.998
3	-66.3 pH + 570 0.999	-61.9 pH + 535 0.999

Moving towards a flow system, two flow rates were explored in Figure 5.12 (a) 100 mL/min and (b) 10 mL/min for both buffer and sheep's blood, (i) shows the sixth SWV scan in blood for Run 1. Alternating measurements were conducted in (ii) blood (×3), and (iii) a pH 7 Carmody buffer (first before protein, then alternating ×3), and (iv) shows the calibration of the BDD-Q pH sensors using Carmody buffers conducted pre- and post-exposure to blood. The pre-blood calibration was used to calculate the pH measured on the BDD-Q pH electrode. Table 5.7 lists the pre- and post-calibration equations. Each data point represents the mean of six SWV scans with standard deviation error bars.

As 100 mL/min effectively reduced BSA/mucin fouling on the BDD-Q electrode, this was used as the starting flow rate for blood. Figure 5.12a (i) shows that at 100 mL/min, the sixth scan for the three alternate measurements in blood for Run 1 shows a shift in peak potentials from 63 to 66 to 62 mV, an overall shift of 4 mV corresponding to 0.07 pH unit. Flowing blood and buffer at 100 mL/min show that alternate measurements in blood and buffer are consistent (Figure 5.12a (ii), (iii)). The average pH values showing little to no variation and small standard deviation error bars for each data point, with only the buffer pH measurements in Run 1 showing statistically significant difference (particularly Buffer 1 and 4 pH measurements, from Tukey comparison). Flowing blood at a higher flow rate, as the solution is constantly moving, this limits the contact duration for the fouling agents in sheep's blood, avoiding less time and

opportunity for surface adsorption, hence less overall fouling observed, compared to the stationary.
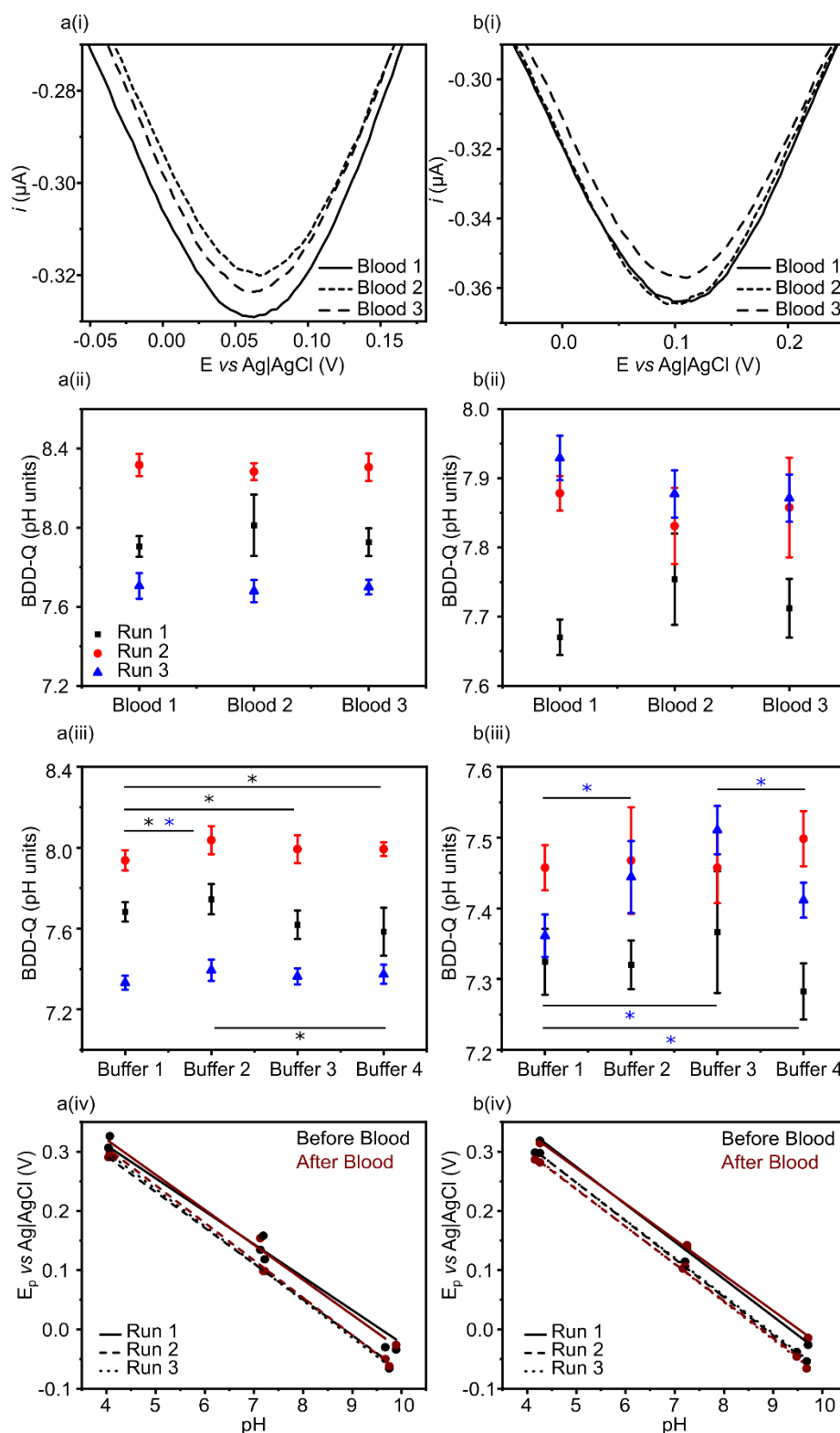
Figure 5.12. pH measurements conducted under flow rates of (a) 100 mL/min and (b) 10 mL/min. (i) The sixth SWV scans from each alternating measurement for Run 1. Average pH measured using the

BDD-Q electrode while alternating between (ii) blood and (iii) Carmody buffer pH 7, with standard deviation error bars n = 6. (iv) The before and after blood calibrations for BDD-Q pH sensor. Data shown as mean ± standard deviation, *$p < 0.05$.

At the reduced flow rate of 10 mL/min, in Figure 5.12b (ii), the average blood pH measurements between runs show agreement at $p_{0.05}$. Between Blood 1 and Blood 2, for Runs 2 and 3, the average pH decreases by 0.05 pH units, from 7.88 to 7.83 and 7.93 to 7.88 for Run 2 and Run 3, respectively. However, for Run 1, the pH increases from 7.72 to 7.75. For the alternate buffer measurements (Figure 5.12b (iii)), Run 1 and 2 show good overlay in pH measurements, however, Run 3 shows an increase from Buffer 1 (prior to blood) to Buffer 3 by 0.15 pH units, and then a decrease by 0.10 pH units (significant at $p < 0.05$). This suggests that flowing at 10 mL/min shows some improvement in accuracy over stationary, but there is still some fouling resulting in unpredictable shift in pH measurements, both in blood and buffer. Table 5.7 summaries the calibration equations conducted pre- and post-blood/buffer measurements at both 10 and 100 mL/min. This along with Figure 5.12a, b(iv) shows that the electrodes calibrate well after exposure to blood. Although there is a small shift in the intercept for the calibrations for 10 mL/min.

Table 5.7.   Calibration equation in the format, y = mx + c, conducted in stationary bulk Carmody buffer solutions for pH measurement of blood and buffer solution under flow rates of 10 and 100 mL/min.

	10 mL/min		100 mL/min	
	Before (mV)	After (mV)	Before (mV)	After (mV)
1	-63.1 pH + 590	-60.2 pH + 573	-59.2 pH + 557	-55.6 pH + 533
	0.999	0.999	0.991	0.996
2	-64.4 pH + 570	-62.7 pH + 550	-59.2 pH + 557	-60.5 pH + 535
	0.999	0.999	0.991	0.999
3	-63.7 pH + 567	-63.7 pH + 556	-63.3 pH + 560	-62.8 pH + 551
	0.999	0.999	0.997	0.999

To further explore the flow rate dependence on fouling, in Figure 5.13, the flow rate of (a) blood was reduced to 1 mL/min (as in an ideal setting you would need to use reduced volumes of blood) while (b) the buffer remains at 100 mL/min. Here the aim is to see if the higher buffer flow rate could act a cleaning method similar to the rinsing explored in Chapter 3. Figure 5.11 (c) represents the calibration of the BDD-Q electrode conducted pre- and post- each run. Each data point represents the mean of six SWV scans with standard deviation error bars.
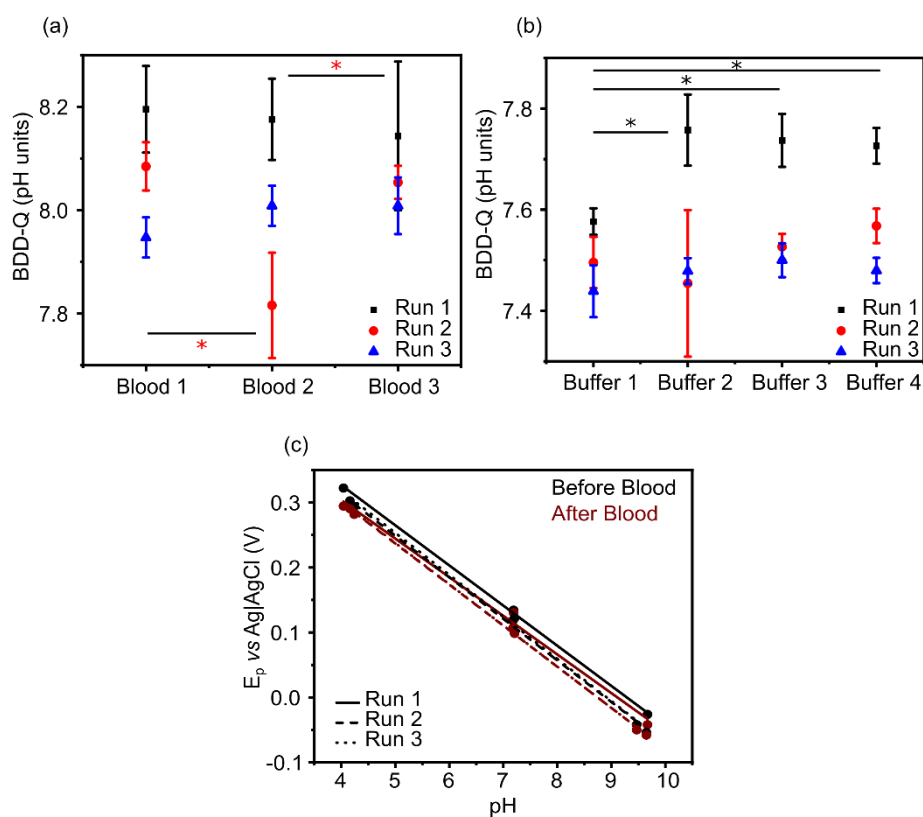
Figure 5.13. Average pH measured using the BDD-Q electrode while alternating between (a) blood at flow rate 1 mL/min and (b) Carmody buffer pH 7 at flow rate 100 mL/min, with standard deviation error bars n = 6. (c) The before and after blood calibrations for BDD-Q pH sensor. Data shown as mean ± standard deviation, *$p < 0.05$.

In Figure 5.13a, the blood measurements show an inconsistency with repeated measurements, for example, going from blood measurement 1 to 2 in

Run 2 there is decrease of 0.27 pH units from pH 8.08 to 7.82. Although Run 1 measurements overlap, the errors indicate a variation of at least 0.1 pH unit. A similar effect is observed with pH buffer measurements. In particular, an increase in pH is observed from buffer 1 measurement to buffer 2 measurement in Run 1 of 0.18 pH unit, which is a pH change of pH 7.58 to 7.76. Furthermore, in Run 2, there is a large variation in the pH measured, with the errors observed for Buffer 2 of 0.15 pH units. Even though the pH measurements are affected by fouling, similar to the response observed in mucin and BSA, the calibrations pre- and post-blood shown in Figure 5.13c and Table 5.8 show minimal changes.

Table 5.8.   Calibration equation in the format, y = mx + c, conducted in stationary bulk Carmody buffer solutions for pH measurement of blood and buffer solution under flow rate of 1 mL/min.

	Before (mV)	After (mV)
1	-61.8 pH + 574	59.4 pH + 542
	0.999	0.997
2	-64.0 pH + 569	-63.3 pH + 553
	0.999	0.999
3	-64.7 pH + 577	-63.5 pH + 555
	0.998	0.999

The flow rate applied for the fouling solution (blood) greatly influences the accuracy of the pH measurement in both fouling media and buffer. 100 mL/min has shown the most effective reduction of fouling on the BDD-Q electrode surface. Additionally, 10 mL/min shows some reduction in fouling compared to 1 mL/min and stationary, however, the response may not be as consistent as at 100 mL/min.

5.4. CONCLUSIONS

Herein, we have developed a 3D-printed flow cell with a laminar flow profile. The flow in the channel is characterised by the data for diffusion-limited reduction of $Ru(NH_3)_6^{3+}$ using a 1 mm macro BDD electrode, which demonstrates

a $V^{1/3}$ dependence on flow rate (0.1 to 100 mL/min). Furthermore, the pH response of BDD-IrOx in buffered, and BDD-Q in buffered and unbuffered solutions have been assessed for the flow rate dependence on the pH response. BDD-IrOx showed flow rate independent pH response in the buffered solutions assessed at flow rates 1, 10, and 100 mL/min. BDD-Q showed flow rate independent response in both buffered and unbuffered solutions, at flow rates of 0.1, 1, 2, 4, 6, 8, 10, 20, 40, 60, 80, and 100 mL/min.

Biological media contains large amounts of proteins, in the gastrointestinal tract, mucin is found in high concentrations, and in the blood, the most abundant protein present is serum albumin. These proteins are known fouling agents that can hinder electrochemical measurements by adsorbing onto the electrode surface. Using biological concentrations of both proteins (0.5% w/v mucin and 5% w/v BSA), BDD-Q electrode was used to measure the pH in stationary solutions, while alternating with buffer solutions. The data clearly showed significant amount of fouling on the pH measurements conducted in both the protein solutions, and the buffer solutions. Therefore, we hypothesised the use of flow as a method to mitigate the fouling observed in the pH measurements. Hence, the same experiments were repeated under flow, at 100 mL/min flow rate. It was clear that flow clearly improved the accuracy of the measurement, hence reducing the fouling that was observed in stationary conditions.

Similar experiments were conducted in blood, a more complex media containing multiple different proteins. Stationary and flow (100 mL/min) pH measurements using BDD-IrOx, showed that the sensor struggled to stabilise in the blood solution, and the subsequent buffer pH measurements were shifted from the pre-blood exposure measurement. Furthermore, stationary measurements using BDD-Q showed some fouling in the blood solution, however, the greatest effect was seen in the subsequent buffer measurements, where the alternating measurements did not show much agreement with the pre-blood buffer pH measurement. Flowing the blood and buffer solutions at 100 and 10 mL/min showed improvement in the blood pH measurements. For buffer pH measurements, both flow rate showed improvement, but 100 mL/min results showed a smaller standard deviation on the mean pH measurements. Clearly flow has reduced the fouling effect observed in stationary blood pH

measurements, however, the alternating buffer pH measurements may still experience some fouling. Suggestions for future work is detailed in Chapter 6.

5.5. REFERENCES

1   D. C. Christodouleas, B. Kaur and P. Chorti, *ACS Cent. Sci.*, 2018, **4**, 1600–1616.

2   M. T. Ghoneim, A. Nguyen, N. Dereje, J. Huang, G. C. Moore, P. J. Murzynowski and C. Dagdeviren, *Chem. Rev.*, 2019, **119**, 5248–5297.

3   M. Ganter and A. Zollinger, *Br. J. Anaesth.*, 2003, **91**, 397–407.

4   D. A. Skoog, F. J. Holler and S. R. Crouch, *Principles of Instrumental Analysis*, Cengage Learning, Boston, USA, 7th Editio., 2016.

5   H. B. Kristensen, A. Salomon, G. Kokholm, A. Salomon and G. Kokholm, *Anal. Chem.*, 1991, **63**, 885–891.

6   D. Daomin Zhou, *Microelectrodes for in-vivo determination of pH*, Elsevier Inc., 2008.

7   D. O'Hare, K. H. Parker and C. P. Winlove, *Med. Eng. Phys.*, 2006, **28**, 982–988.

8   K. Chaisiwamongkhol, C. Batchelor-Mcauley and R. G. Compton, *Analyst*, 2019, **144**, 1386.

9   S. Kakooei, C. Ismail and B. Ari-Wahjoedi, *Int. J. Mater. Sci. Innov.*, 2013, **1**, 62–72.

10   D. J. Graham, B. Jaselskis and C. E. Moore, *J. Chem. Educ.*, 2013, **90**, 345–351.

11   C. Cheng, Y. Wu, X. Li, Z. An, Y. Lu, F. Zhang, B. Su and Q. Liu, *Sensors Actuators B Chem.*, 2021, **349**, 130781.

12   S. A. Grant, K. Bettencourt, P. Krulevitch, J. Hamilton and R. Glass, *Sensors Actuators, B Chem.*, 2001, **72**, 174–179.

13   H. Cao, V. Landge, U. Tata, Y.-S. Seo, S. Rao, S.-J. Tang, H. F. Tibbals, S. Spechler and J.-C. Chiao, *IEEE Trans. Biomed. Eng.*, 2012, **59**, 3131–3139.

14   M. Lu and R. G. Compton, *Analyst*, 2014, **139**, 2397–2403.

15   M. Lu and R. G. Compton, *Analyst*, 2014, **139**, 4599–4605.

16   Z. J. Ayres, A. J. Borrill, J. C. Newland, M. E. Newton and J. V Macpherson, *Anal. Chem.*, 2016, **88**, 974–980.

17   S. J. Cobb, Z. J. Ayres, M. E. Newton and J. V. Macpherson, *J. Am. Chem. Soc.*, 2019, **141**, 1035–1044.

18   L. J. Simcox, R. P. A. Pereira, E. M. H. Wellington and J. V. Macpherson, *ACS Appl. Mater. Interfaces*, 2019, **11**, 25024–25033.

19   P. Joshi, P. Riley, K. Y. Goud, R. K. Mishra and R. Narayan, *Curr. Opin. Electrochem.*, 2022, **32**, 100920.

20   D. Shin, D. A. Tryk, A. Fujishima, A. Merkoçi and J. Wang, *Electroanalysis*, 2005, **17**, 305–311.

21   L. Jiang, I. Santiago and J. Foord, *Carbon N. Y.*, 2021, **174**, 390–395.

22   T. Rajan, T. Read, A. Abdalla, B. Patel and J. Macpherson, *ACS Sensors*, 2020, **5**, 2858–2865.

23   Y. Li, W. Chen and L. Lu, *ACS Appl. Bio Mater.*, 2020, 0–58.

24   M. H. Iqbal, A. Aydin, O. Brunckhorst, P. Dasgupta and K. Ahmed, *J. R. Soc. Med.*, 2016, 109, 372–380.

25   S. Lin, W. Yu, B. Wang, Y. Zhao, K. En, J. Zhu, X. Cheng, C. Zhou, H. Lin, Z. Wang, H. Hojaiji, C. Yeung, C. Milla and R. W. Davis, *Proc. Natl. Acad. Sci. U. S. A.*, 2020, **117**, 19017–19025.

26   S. Cheng, Z. Gu, L. Zhou, M. Hao, H. An, K. Song, X. Wu, K. Zhang, Z. Zhao, Y. Dong and Y. Wen, *Front. Bioeng. Biotechnol.*, 2021, **9**, 1–21.

27   E. Pinilla-Gil, *J. Appl. Bioanal.*, 2015, **1**, 68–71.

28   S. Nakata, T. Arie, S. Akita and K. Takei, *ACS Sensors*, 2017, **2**, 443–448.

29   W. Jia, A. J. Bandodkar, G. Valdés-Ramírez, J. R. Windmiller, Z. Yang, J. Ramírez, G. Chan and J. Wang, *Anal. Chem.*, 2013, **85**, 6553–6560.

30   T. Guinovart, A. J. Bandodkar, J. R. Windmiller, F. J. Andrade and J. Wang, *Analyst*, 2013, **138**, 7031–7038.

31   H. Lee, C. Song, Y. S. Hong, M. S. Kim, H. R. Cho, T. Kang, K. Shin, S. H. Choi, T. Hyeon and D. H. Kim, *Sci. Adv.*, 2017, **3**, 1–9.

32   J. Xu and H. Lee, *Chemosensors*, 2020, **8**, 1–29.

33   L. Rivas, S. Dulay, S. Miserere, L. Pla, S. B. Marin, J. Parra, E. Eixarch, E. Gratacós, M. Illa, M. Mir and J. Samitier, *Biosens. Bioelectron.*, 2020, **153**, 112028.

34   I. Bogachan Tahirbegi, O. Mir and J. Samitier, *Biosens. Bioelectron.*, 2013, **40**, 323–328.

35   C. Ming Li, H. Dong, X. Cao, J. T. Luong and X. Zhang, *Curr. Med. Chem.*, 2007, **14**, 937–951.

36   T. D. Yoshida Kozai, N. B. Langhals, P. R. Patel, X. Deng, H. Zhang, K. L. Smith, J. Lahann, N. A. Kotov and D. R. Kipke, *Nat. Mater.*, 2012, **11**, 1065–1073.

37   H. N. Schwerdt, E. Zhang, M. J. Kim, T. Yoshida, L. Stanwicks, S. Amemori, H. E. Dagdeviren, R. Langer, M. J. Cima and A. M. Graybiel, *Commun. Biol.*, 2018, **1**, 1–11.

38   M. Shichiri, R. Kawamori, Y. Goriya, Y. Yamasaki, M. Nomura, N. Hakui and H. Abe, *Diabetologia*, 1983, **24**, 179–184.

39   L. C. Clark, J. R. And and C. A. Duggan, *Diabetes Care*, 1982, **5**, 174–180.

40   I. H. Jaffer, J. C. Fredenburgh, J. Hirsh and J. I. Weitz, *J. Thromb. Haemost.*, 2015, **13**, S72–S81.

41   C. Jiang, G. Wang, R. Hein, N. Liu, X. Luo and J. J. Davis, *Chem. Rev.*, 2020, **120**, 3852–3889.

42   I. C. Samper, S. A. N. Gowers, M. L. Rogers, D.-S. S. R. K. Murray, S. L. Jewell, C. Pahl, A. J. Strong and M. G. Boutelle, *Lab Chip*, 2019, **19**, 2038–2048.

43   M. L. Rogers, C. L. Leong, S. A. Gowers, I. C. Samper, S. L. Jewell, A. Khan, L.

McCarthy, C. Pahl, C. M. Tolias, D. C. Walsh, A. J. Strong and M. G. Boutelle, *J. Cereb. Blood Flow Metab.*, 2017, **37**, 1883–1895.

44   S. A. N. Gowers, M. L. Rogers, M. A. Booth, C. L. Leong, I. C. Samper, T. Phairatana, S. L. Jewell, C. Pahl, A. J. Strong and M. G. Boutelle, *Lab Chip*, 2019, **19**, 2537–2548.

45   Y. Zhang, N. Jiang and A. K. Yetisen, *Biosens. Bioelectron.*, 2021, **189**, 113351.

46   S. A. N. Gowers, I. C. Samper, D.-S. S. R. K. Murray, G. K. Smith, S. Jeyaprakash, M. L. Rogers, M. Karlsson, M. H. Olsen, K. Møller and M. G. Boutelle, *Analyst*, 2020, **145**, 1894–1902.

47   M. E. Snowden, P. H. King, J. A. Covington, J. V. MacPherson and P. R. Unwin, *Anal. Chem.*, 2010, **82**, 3124–3131.

48   R. B. Channon, M. B. Joseph and J. V Macpherson, *Electrochem. Soc. Interface*, 2016, **25**, 63–68.

49   S. A. N. Gowers, V. F. Curto, C. A. Seneci, C. Wang, S. Anastasova, P. Vadgama, G. Z. Yang and M. G. Boutelle, *Anal. Chem.*, 2015, **87**, 7763–7770.

50   G. D. O'Neil, S. Ahmed, K. Halloran, J. N. Janusz, A. Rodríguez and I. M. Terrero Rodríguez, *Electrochem. commun.*, 2019, **99**, 56–60.

51   R. M. Cardoso, C. Kalinke, R. G. Rocha, P. L. dos Santos, D. P. Rocha, P. R. Oliveira, B. C. Janegitz, J. A. Bonacin, E. M. Richter and R. A. A. Munoz, *Anal. Chim. Acta*, 2020, **1118**, 73–91.

52   C. W. Foster, H. M. Elbardisy, M. P. Down, E. M. Keefe, G. C. Smith and C. E. Banks, *Chem. Eng. J.*, 2020, **381**, 122343.

53   W. R. Carmody, *J. Chem. Educ.*, 1961, **38**, 559–560.

54   L. Hutton, M. E. Newton, P. R. Unwin and J. V Macpherson, *Anal. Chem*, 2009, **81**, 1023–1032.

55   A. W. Colburn, K. J. Levey, D. O'Hare and J. V Macpherson, *Phys. Chem. Chem. Phys.*, 2021, **23**, 8100–8117.

56   J. Booth, R. G. Compton, J. A. Cooper, R. A. W. Dryfe, A. C. Fisher, L. Davies, M. K. Walters, C. L. Davies and M. K. Walters, *J. Phys. Chem.*, 1995, **99**, 10942–10947.

57   A. J. Bard and L. R. Faulkner, *Electrochemical Methods Fundamentals and Applications*, John Wiley & Sons, 2001.

58   R. G. Compton and P. R. Unwin, *J. Electroanal. Chem. Interfacial Electrochem.*, 1986, **205**, 1–20.

59   A. Lardner, *J. Leukoc. Biol.*, 2001, **69**, 522–530.

60   H. J. Chung, M. S. Sulkin, J. S. Kim, C. Goudeseune, H. Y. Chao, J. W. Song, S. Y. Yang, Y. Y. Hsu, R. Ghaffari, I. R. Efimov and J. A. Rogers, *Adv. Healthc. Mater.*, 2014, **3**, 59–68.

61   M. Damaghi, J. W. Wojtkowiak and R. J. Gillies, *Front. Physiol.*, 2013, **4**, 1–10.

62   S. Głab, A. Hulanicki, E. Gunnar and F. Ingman, *Crit. Rev. Anal. Chem.*, 1989, **21**, 29–47.

63   N. Agmon, *Chem. Phys. Lett.*, 1995, **244**, 456–462.

64   W. L. Caudill, J. O. Howell and R. M. Wightman, *Anal. Chem.*, 1982, **54**, 2532–2535.

65   J. G. Osteryoung and R. A. Osteryoung, *Anal. Chem.*, 1985, **57**, 101–110.

66   B. L. Hanssen, S. Siraj and D. K. Y. Wong, *Rev. Anal. Chem.*, 2016, **35**, 1–28.

67   S. Campuzano, M. Pedrero, P. Yáñez-Sedeño and J. M. Pingarrón, *Int. J. Mol. Sci.*, 2019, **20**, 1–19.

Chapter 6.   CONCLUSIONS AND FUTURE WORK

In Chapter 3, the pH profile of the upper gastrointestinal (GI) tract of a mouse, from the oesophagus to duodenum was investigated in the absence and presence of pharmacological agents targeted altering the acid/bicarbonate production. Three pH electrodes were assessed for the suitability for application in the GI environment, which is known to contain high concentrations of mucin. Therefore, a buffer solution containing 0.5% mucin was used as a mimic for the GI environment. The electrodes assessed include, the traditional glass pH probe, iridium oxide (IrOx) film electrodeposited on boron doped diamond (BDD-IrOx) (both operated potentiometrically), and a quinone (Q) surface-integrated BDD (BDD-Q) electrode (voltammetric). The latter is produced by selectively introducing sp^2 micro-spots using a laser-ablation technique, the surface quinone groups undergo a proton coupled electron transfer process to provide the pH response. In mucin, both glass and BDD-IrOx takes ~100's of s to provide a stable measurement, most likely due to fouling from mucin adsorption, in contrast the BDD-Q electrode takes 6 s per scan. Besides response time, both glass and IrOx pH were also compromised on robustness due to fragility of the glass, and delamination of the IrOx film, as contact with the GI tissue was an experimental requirement. BDD-Q was deemed the most suitable.

Ten pH measurements were made along the GI tract oesophagus (1), stomach (5), and duodenum (4). Under buffered conditions, BDD-Q electrode tracked the pH from neutral in oesophagus, to acidic in the stomach, to alkaline in the duodenum. Under omeprazole (the proton pump inhibitor) treatment, the middle regions (body) of the stomach displayed elevated pH values. In the presence of melatonin (an acid inhibitor and bicarbonate agonist), the body of the stomach and the duodenum showed increased pH values. To reduce any possible fouling from tissue contact, the BDD-Q probe was gently rinsed in between measurements.

Future work in this area could see the BDD-Q pH sensor technology moving from *ex vivo* to *in vivo* applications. This involves the need to miniaturise the sensor to be able to integrate into an ingestible sensor or endoscopic probes,

and also building the necessary electronics to support the ingestible capsule. Another potential area to explore is the possibility of analysing multiple analytes using the same electrode. As biological systems containing a multitude of signalling molecules, most of them electroactive, the BDD-Q sensor could be used for simultaneous detection of pH and signalling molecules such, as serotonin, dopamine etc, provided the response does not overlap with the pH signal.

Chapter 4 investigates the time dependent effect of protein adsorption on three carbon-based electrodes, these include BDD, sp^2 BDD, and glassy carbon (GC). BDD is known to be weakly adsorbing, therefore has the potential to exhibit a reduced fouling response. The sp^2-BDD electrode is fabricated by a similar laser ablation method used for BDD-Q, but instead of micro-spots, the whole surface is graphitised. Finally, GC is typical sp^2 electrode, that provides a good comparison to sp^2-BDD electrode with its hybrid sp^3 (bulk) -sp^2 (surface) structure.

The Pt microelectrode response of two transition metal redox couples, $Ru(NH_3)_6^{3+}$ and $IrCl_6^{2-}$ were assessed in the absence and presence of proteins, mucin (0.5% w/v) and bovine serum albumin (BSA, 5% w/v). BSA is one of the most abundant proteins (and fouling agent) present in blood. The presence of proteins such as, mucin and BSA in solution, was found to increase the viscosity of the solution, which in turn decreased the diffusion coefficient for $Ru(NH_3)_6^{3+}$. Interestingly, $IrCl_6^{2-}$ was found to undergo a chemical reduction to $IrCl_6^{3-}$, most likely due to the cysteine residues found in mucin and BSA prior to applying any potential, this was observed by the shift in the zero current position.

The time dependent cyclic voltammetric (CV) response of $Ru(NH_3)_6^{3+}$ was assessed for 912 s in the absence and presence of proteins. Firstly, the cathodic peak current of the first scan was found to decrease in the presence of mucin by 22%, 15%, and 12% for BDD, sp^2-BDD, and GC, respectively. The peak-to-peak separation (ΔE_p) for BDD and sp^2-BDD increased, but for GC there was minimal change. In the presence of BSA, the peak current for BDD reduced by 52% in the first scan, but BSA had the greatest effect on sp^2-BDD, with the peak current decreasing till 112 s, but then increasing. The peak current correlates with ΔE_p for sp^2-BDD, starting at 131 mV, increasing to 134 mV, then decreasing to 74 mV by 912 s. Peak current for GC in the presence of BSA reduces by 24% in the first scan and minimal change in ΔE_p. On BDD both mucin and BSA exhibits a

combination of adsorption and viscosity effect, and the electron transfer kinetics is more affected for BDD and sp^2-BDD than GC. The time dependent oxidation of $IrCl_6^{3-}$ was also assessed, the peak current was found to decrease over time (910 s) for all three electrodes. BSA was found to have a greater fouling effect on GC as the peak current stabilise for BDD and sp^2-BDD but not for GC. Furthermore, CV shape was observed to change from peak shaped to steady state on all three electrodes.

The double layer capacitance of the three electrodes was assessed using CV in the absence and presence of proteins for 900 s. The capacitance was found to decrease over time on BDD and sp^2-BDD, an indication of protein adsorption, as the protein layer on the surface, the capacitance drops. However, this method used for quantifying capacitance, was found to be challenging with the GC electrode, as even under degassed conditions, faradaic processes were difficult to eliminate.

Finally, electrodeposition of silver was assessed using CV and scanning electron microscopy (SEM) on the surface of BDD and sp^2-BDD, as method to understand the protein film formation at different potentials (+0.4 V and -0.4 V). The characteristic Ag reduction peak was observed to shift more negative after +0.4 V treatment in mucin for BDD. However, after +0.4 V treatment in BSA, the electrodeposition was hindered, with the first scan does not show a peak for deposition. On sp^2-BDD, the +0.4 V treatment had a greater effect in both mucin and BSA, as there is an absence of Ag deposition peak in the first scan. In contrast, the -0.4 V treatment barely shifts the characteristic Ag peak potential, except on sp^2-BDD in the presence of BSA. SEM imaging showed, after -0.4 V treatment, there was a presence of large Ag particles (micron sized) at a low density, and after +0.4 V treatment, there was high density of smaller Ag particles (nanometre sized). This study shows the surface polarisation is extremely important when studying protein adsorption. Also, BSA has a greater fouling affect than mucin, especially on sp^2-BDD and GC electrodes.

A 3D printed flow cell, with laminar flow profile was developed in Chapter 5. The flow profile was characterised using the diffusion-limited reduction of $Ru(NH_3)_6^{3+}$ at a BDD macroelectrode (diameter 1 mm) with reference electrode (Ag|AgCl) placed directly opposite and the counter Pt wire

placed downstream. A $V^{1/3}$ dependence on flow rate was observed at flow rates of 0.1 to 100 mL/min. For pH sensing, the BDD macro electrode was replaced with either BDD-IrOx or BDD-Q pH sensor (diameter 1 mm). The pH response for BDD-IrOx in buffered, and BDD-Q in buffered and unbuffered solutions were assessed for flow rate dependence. BDD-IrOx showed flow rate independent pH response at flow rates 1, 10, and 100 mL/min. BDD-Q exhibited flow rate independent pH response at flow rates from 0.1 to 100 mL/min.

As discussed in Chapter 3 and 4, biological matrix contains high concentrations of proteins that can cause electrode fouling, and result in erroneous measurements. Therefore, BDD-Q pH electrode was used to study the fouling in solutions containing biological concentrations of mucin (0.5% w/v) or BSA (5% w/v) in both stationary and flow (100 mL/min) conditions. The pH measurements were alternated with Carmody buffer solutions, to understand the degree of fouling on the sensor. Stationary measurements in both protein solutions showed significant difference in the pH measured within each run. Flowing the solutions at 100 mL/min showed improvement in the pH measurements conducted in the protein solutions, although some of the buffer measurements showed slight difference in pH values. The experiments conducted in protein solutions suggest that flow could be used as a method to mitigate electrode fouling from protein adsorption.

A similar experiment was conducted in the more complex solution of sheep's blood. Stationary and flow (100 mL/min) pH measurement were conducted using BDD-IrOx, the sensors struggled to stabilise in blood, and the pH was found to shift over time under stationary measurements. Under flow, the pH response slightly improved for the buffer measurements, with a faster response time, however, the pH value shifted with repeat measurements. Blood pH measurement under flow with BDD-IrOx, also struggled to stabilise and the pH value was found to shift with repeat measurements. For BDD-Q sensors, the stationary blood-buffer alternate pH measurements showed significant difference in the pH values recorded. Flowing at 10 and 100 mL/min, showed significant improvement in both blood and buffer measurement using BDD-Q, with 100 mL/min demonstrating smaller errors in the pH measurement.

This study has demonstrated by proof-of-concept, that flow can be used as a method to reduce fouling on the electrode surface. However, the method needs improvement. Laminar flow has the highest velocity at the middle of the flow channel, and reaching zero at the walls, which means the electrode surface experiences minimal force. Turbulent flow, however, introduces force in a random manner and could be used to target the electrode surface and reduce build-up of fouling agents on the electrode surface and/or on the walls of the flow cell. Therefore, introducing structures within the flow cell channel creates a turbulent flow rather than having a laminar flow that just flows past the electrode surface without actually cleaning the surface.

A potential future work in this area would be to change the flow cell designs. Figure 6.1 shows potential flow cell designs to minimise this fouling effect. Figure 6.1a. suggests a method to introduce turbulence to the flow system whereby introduce microstructures on the walls of the channel to create turbulence, this could be easily achieved using 3D printing. Figure 6.1b. proposes a wall-jet design, where solution flow impinges directly on the electrode surface, ideally maximising removal of adsorbed protein from the electrode surface.
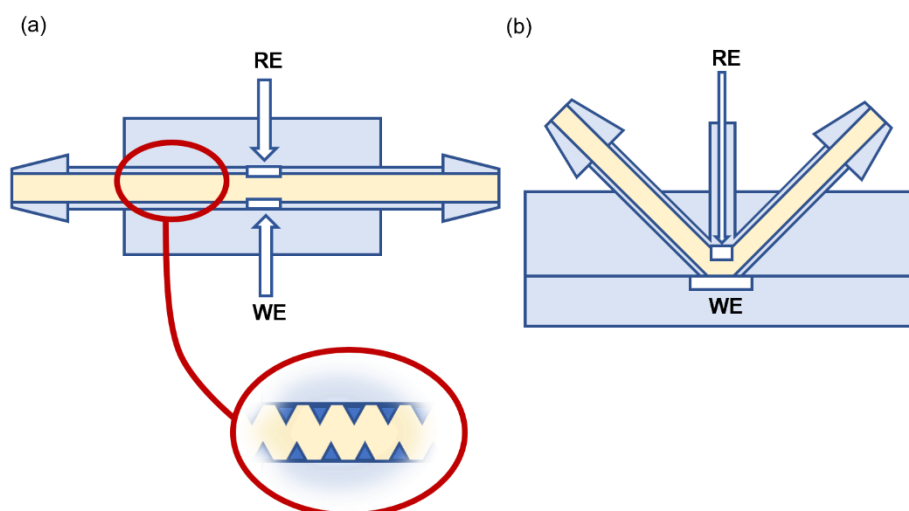

Figure 6.1. Schematic illustrating potential flow cell designs to minimise fouling effect by (a) generating a turbulent flow or (b) a wall-jet like flow cell that can directly clean the electrode surface with the solution flow.

Moving towards point-of-care, this study shows potential for integrating flow devices into the intravenous lines commonly used in hospitals to infuse fluids, electrolytes, and medications and to obtain venous blood samples from patients. Other applications include the use in monitoring the pH in patients undergoing dialysis, for brain injury and kidney functions.

Combining the results from Chapter 4 and 5, future work can also explore the development of a self-diagnosing pH sensor that can detect when the surface has fouled beyond a point where the recorded measurements are no longer reliable. The information from the sensor can then trigger a cleaning procedure, which could involve the automatic flushing of the electrode surface, or a more thorough mechanical cleaning (e.g., polishing).